

**SPATIO-TEMPORAL VARIABILITY OF MINERAL DUST OVER THE  
ARABIAN SEA AND ITS IMPACT ON PRIMARY PRODUCTION**

A thesis submitted to Goa University for the award of the Degree of

**DOCTOR OF PHILOSOPHY**

IN

**MARINE SCIENCE**

By

**Priyanka Banerjee**

Research Guide

**Dr. S. Prasanna Kumar**

Chief Scientist

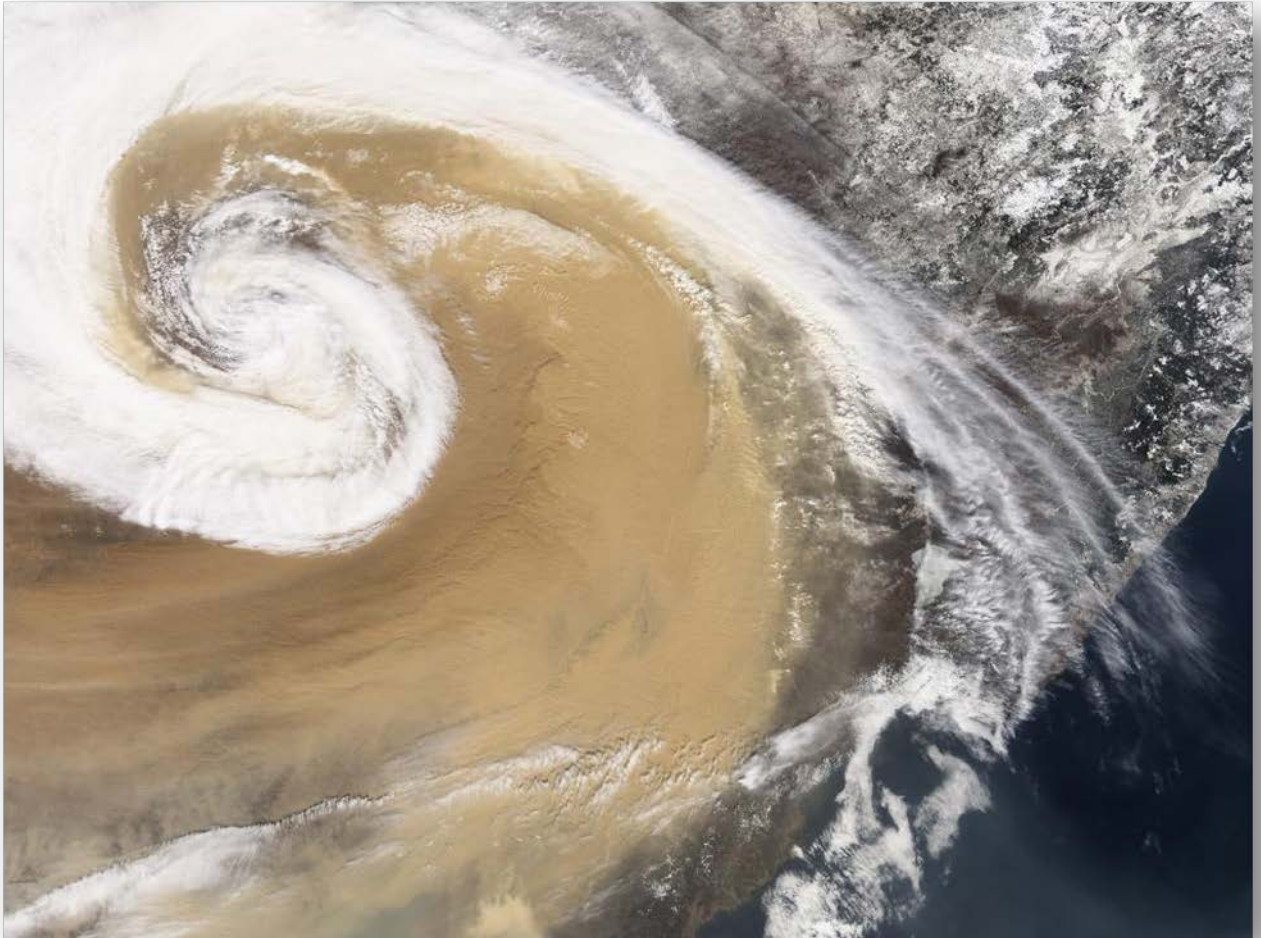
CSIR-National Institute of Oceanography  
(Council of Scientific and Industrial Research)

Dona Paula, Goa – 403004, India.

**GOA UNIVERSITY**

Taleigao Goa

**April 2015**



*Some infinities are bigger than our infinities.....*

*Dedicated to my aunt.....*

## Statement

As required under the university ordinance 0.19.8 (vi), I hereby state that the present thesis entitled “**Spatio-temporal variability of mineral dust over the Arabian Sea and its impact on primary production**” is my original contribution and the same has not been submitted on any previous occasion. To the best of my knowledge, the present study is the first comprehensive work of its kind from the area mentioned.

The literature related to the problem investigated has been cited. Due acknowledgements have been made wherever facilities and suggestions have been availed off.

**Priyanka Banerjee**

CSIR-National Institute of Oceanography

Dona Paula, Goa

Place: Dona Paula

Date: 29 April 2015

## **Certificate**

This is to certify that the thesis entitled “**Spatio-temporal variability of mineral dust over the Arabian Sea and its impact on primary production**” submitted by **Ms. Priyanka Banerjee** for the award of the degree of Doctor of Philosophy in Marine Science is based on original studies carried out by her under my supervision. The thesis or any part of thereof has not been previously submitted for any other degree or diploma in any university or institution.

**(Dr. S. Prasanna Kumar)**

Research Supervisor

CSIR-National Institute of Oceanography

Dona Paula, Goa

Place: Dona Paula

Date: 29 April 2015

## **Abstract**

The atmosphere over the Arabian Sea perennially contains high levels of mineral dust aerosols transported from the surrounding arid and semi-arid regions of Asia and North Africa. Observations and models have demonstrated that mineral dust over the Arabian Sea can influence the climate of the region by modulating the hydrological cycle, the radiative budgets and especially the large-scale monsoon system. In spite of the importance of mineral dust in this region, a holistic view of the dust cycle and its variability has not emerged. There is no understanding, till date, of how the different climate modes can exert an influence on the interannual variability of dust over the Arabian Sea. Over the last three decades studies have postulated an interesting possibility that there might be some association between dust depositions and the phytoplankton biomass. The Arabian Sea is a highly productive region due to upwelling during the southwest monsoon and winter convection during the northeast monsoon. However, till date no study has tried to explore if the oceanic supply of nutrients are sufficient to support the observed levels of phytoplankton biomass and how much nutrients can be supplied by dust depositions.

The aim of this thesis is to study the temporal variability of dust cycle at seasonal scale, the influence that different climate modes may exert on the levels of dust activity at interannual time scale and to identify mechanistic relations between dust depositions and phytoplankton biomass in the Arabian Sea. In order to achieve this, a regional climate model has been set up and the dust cycle has been simulated for 10 years from 2001 to 2010. The model results have been used to study the seasonal cycle of dust emission, transport and depositions along with the factors that control this seasonal cycle. The interannual variability of dust load over the Arabian Sea and its

surroundings has been studied using time-series of 26 years of Aerosol Index data derived from satellite. This has been used to explore how the climate modes such as El Nino-Southern Oscillation and the Indian Ocean Dipole can remotely control the climatic conditions over the dust source regions. Lastly, the possibility of dust depositions leading to phytoplankton biomass enhancements in the Arabian Sea has been studied with particular stress on the northeast monsoon period. Using satellite-derived chlorophyll concentrations as a proxy to phytoplankton biomass, any episodic increase in chlorophyll levels following dust storms have been marked and the demand for macro and micro nutrients have been calculated. Comparing this demand with the possible supply of water column and the atmospheric depositions of different nutrients has revealed how far dust depositions are important in driving phytoplankton blooms in the Arabian Sea.

The results from the thesis show that at seasonal scale 47% of dust emissions and 79% of dust depositions into the Arabian Sea take place during the southwest monsoon season. To the east and the south of the intertropical convergence zone, the mobilization and transport of is controlled by the strength of the southwest monsoon wind system. To the north and the west of the convergence zone, the same is controlled by the northerly and northwesterly wind system related to the surrounding high pressure regions. At the top of the Troposphere, dust transport is accomplished by the easterly return flow of the monsoon system, thereby, transporting dust to long distances. At interannual scale, La Nina conditions are conducive to increased dust production and dust transport, while El Nino conditions lead to suppression of dust activity in the Arabian Sea and the surroundings. This is affected by El Nino remotely modulating the amount of winter precipitation over the dust source regions and is related to the intensity of convection over the Indo-Pacific warm pool region. El Nino-Southern Oscillation explains about 36% of the

interannual variability of dust activity over the Arabian Sea and its surroundings. The effect of the Indian Ocean Dipole on dust activity in this region is to counteract the effect of El Nino. Finally, the thesis also suggests that dust depositions can lead to episodic enhancements of the phytoplankton biomass in the central Arabian Sea during the northeast monsoon by supplying micronutrient iron. It is likely that any deepening of the mixed layer within the central Arabian Sea can supply enough macro-nutrients, but not enough micro-nutrient dissolved iron. This possibly leads to iron limitation. Following episodic dust depositions, if enough dissolved iron is supplied by dust, phytoplankton blooms can take place. The high dust years account for 47% of the total chlorophyll concentrations in the Arabian Sea during the northeast monsoon. Any such definitive conclusions cannot be arrived at for other seasons.

## Acknowledgements

When I took the decision in 2010 to come to Goa and work with Dr. S. Prasanna Kumar, my mind was cluttered with uncertainties and questions. Writing this volume in 2015, I am glad that that this decision has resulted in an enriching journey for me. Working with my supervisor, Dr. Prasanna Kumar has been a rewarding experience. He has been challenging and has motivated me to delve beneath the surface of the things around me. No doubt about the fact that hours of discussions with him have formed the basis of my understanding of the workings of the ocean-atmosphere system. I am grateful to him for being particularly inspiring, for his patience, for believing in me and for his cutting perspicacity towards science. I strongly believe that without his able guidance my thesis would not have been realized in the present form and I would have been much further away from fulfilling my objectives.

I am grateful to my Vice Chancellor's nominee Dr. P. Vethamony for always being prompt, encouraging and positive. My sincere thanks to Dr. V. Ramaswamy for discussions regarding the compositions of aerosols collected over Goa, the understanding of which have helped me to calculate the atmospheric flux of nutrients into the Arabian Sea. I am thankful to the Council of Scientific and Industrial Research (CSIR) for granting me fellowship to undertake this research work. I would also like to thank Dr. S.W.A Naqvi, Director, CSIR-National Institute of Oceanography for providing all the required research facilities. My gratitude goes out to Dr. G. N. Nayak and Dr. H.B. Menon of the Department of Marine Science, Goa University for their kind support during the various phases of the Ph.D program. I would hereby also like to acknowledge the several useful comments from Dr. Kenneth Coale, Dr. Amato Evan and other

anonymous reviewers on the submitted papers that have provided me new insights into the workings of the dust and the climate system.

I am indebted to my office mates and my seniors for their continuous positive support. I take this opportunity to express my heartfelt thanks to Jayu, Divya, Joshua, Renjith, Vijith, Navaneeth, Ravinder and Aswini. Many thanks to Byju for helping me hone my programming skills in Linux and Ferret. A big thank you to Praveen Kumar for patiently sitting for hours and helping me out whenever I managed to crash my laptop (Yes, I have mastered the art of crashing my laptop). Your help is most appreciated! I would like to express my gratitude to Vidya and Mani Murali for cheering me up whenever I was feeling down and for all the “useful” and “useless” talks. My special thanks to two wonderful friends that I have made during my years in Goa: Arnab and Simontini. They have been beside me during the most challenging times, have tolerated me at my worst and have made my stay here a lot easier. I fondly remember the wonderful and crazy trips together and the weekends spent with you people. Most important of all I would like to thank my family who have gone through lot of difficulties and have made tremendous sacrifices to enable me to complete my thesis. This journey would not have been possible without their support.

# Table of Contents

<b>Statement</b> .....	<b>i</b>
<b>Certificate</b> .....	<b>ii</b>
<b>Abstract</b> .....	<b>iii</b>
<b>Acknowledgements</b> .....	<b>vi</b>
<b>Table of Contents</b> .....	<b>viii</b>
<b>List of Figures</b> .....	<b>xi</b>
<b>List of Tables</b> .....	<b>xx</b>
<b>List of Abbreviations</b> .....	<b>xxi</b>
<b>List of Publications from the thesis</b> .....	<b>xxiii</b>
<b>1 Introduction</b> .....	<b>1</b>
1.1 MINERAL DUST IN THE CLIMATE SYSTEM.....	1
1.2 DUST OVER THE ARABIAN SEA .....	4
1.3 DUST AND PHYTOPLANKTON IN THE ARABIAN SEA .....	9
1.4 AIMS OF THE PRESENT STUDY .....	10
1.5 THESIS OUTLINE .....	11
<b>2 Study Region</b> .....	<b>14</b>
2.1 CLIMATE OF THE ARABIAN SEA .....	14
2.1.1 The southwest monsoon.....	15
2.1.2 The northeast monsoon.....	17
2.2 BIO-PHYSICAL COUPLING IN THE ARABIAN SEA .....	18
2.2.1 The southwest monsoon.....	18
2.2.2 The northeast monsoon.....	20
2.3 DUST SOURCE REGIONS.....	21
<b>3 Data and Methods</b> .....	<b>25</b>
3.1 REGIONAL CLIMATE MODEL .....	25
3.2 1-D MIXED LAYER DEPTH MODEL .....	31
3.3 REMOTE SENSING OF DUST .....	32
3.3.1 Derivation of dust optical depth from satellite.....	32
3.3.2 Aerosol Index.....	34
3.3.3 MODIS deep blue aerosol optical depth.....	36
3.3.4 AERONET Data.....	36

	3.4 OTHER DATA.....	37
<b>4</b>	<b>Validation of Regional Climate Model over the Arabian Sea .....</b>	<b>40</b>
	4.1 APPROACH .....	40
	4.2 COMPARISON WITH SATELLITE OBSERVATIONS .....	42
	4.3 COMPARISON WITH AERONET OBSERVATIONS .....	45
	4.4 COMPARISON OF MODEL FORCINGS WITH OUTPUT .....	47
	4.5 SUMMARY.....	54
<b>5</b>	<b>Dust cycle over the Arabian Sea .....</b>	<b>55</b>
	5.1 DUST EMISSION.....	55
	5.1.1 Seasonal cycle of dust emission.....	55
	5.1.2 Region-wise meteorological conditions favouring dust emissions.....	58
	5.2 DUST TRANSPORT.....	69
	5.3 DUST DEPOSITION.....	78
	5.4 SUMMARY.....	80
<b>6</b>	<b>Influence of Climate Modes on dust over the Arabian Sea .....</b>	<b>82</b>
	6.1 INFLUENCE OF ENSO .....	82
	6.1.1 Relation between dust, precipitation and soil moisture.....	83
	6.1.2 Relation between AI-1.5 and ENSO.....	86
	6.1.3 How ENSO modulates interannual variability of AI-1.5?.....	90
	6.2 INFLUENCE OF IOD .....	97
	6.3 SUMMARY.....	100
<b>7</b>	<b>Influence of dust on the primary productivity over the Arabian Sea .....</b>	<b>102</b>
	7.1 INFLUENCE OF DUST DURING WINTER MONSOON .....	102
	7.1.1 Correlations between dust and chlorophyll.....	102
	7.1.2 Simulated episodic dust depositions.....	106
	7.1.3 Enhancements of chlorophyll a following episodic dust storms in the central Arabian Sea.....	109
	7.1.4. Possible mechanisms leading to phytoplankton blooms in the central Arabian Sea.....	112

7.1.5. Requirements versus supply of nutrients.....	113
7.1.6. Significance of dust deposition related to community structure of the Arabian Sea.....	122
7.1.7. Contribution of dust to interannual variability in the chlorophyll.....	123
7.2 INFLUENCE OF DUST DURING REST OF THE YEAR .....	125
7.2.1 Influence of dust during spring intermonsoon.....	125
7.2.2 Influence of dust during southwest monsoon.....	126
7.2.3 Influence of dust during fall intermonsoon.....	127
7.3 SUMMARY.....	129
<b>8 Summary and Outlook .....</b>	<b>130</b>
<b>Bibliography .....</b>	<b>134</b>
<b>Publications from the thesis</b>	

# List of Figures

**Figure 1.1** Global distribution pattern of main types of aerosols present in the atmosphere. Red indicates dust aerosols, blue: sea salt, white: sulphate aerosols and green: biomass burning aerosols. (Image courtesy NASA Goddard Space Flight Center).....2

**Figure 1.2** Schematic representations of some of the different ways in which dust can influence the climate.....4

**Figure 2.1** Climatology (1997-2013) of the seasonal cycle of monsoon wind system over the northern Indian Ocean for (a) southwest monsoon and (b) northeast monsoon. The shading shows precipitation and the arrows represent the wind vectors. The black contours are the sea level pressure shown only for 1014 and 1004 mb pressure levels. The thick green line represents the mean position of the intertropical convergence zone taken to be the location where the meridional component of the wind becomes zero. The climatology of precipitation has been constructed from the Tropical Rainfall Measuring Missions data, while those for wind and pressure are from National Centers for Environmental Prediction/ National Center for Atmospheric Research (NCEP/NCAR) reanalysis.....16

**Figure 2.2** Climatological (2003-2013) distribution of chlorophyll *a* concentration (shading), surface currents (vector) and sea surface temperature (red contours) over the Arabian Sea during (a) southwest monsoon and (b) northeast monsoon. Chlorophyll *a* concentration data is from Moderate Resolution Imaging Spectroradiometer (MODIS) onboard Aqua satellite, current vector is from Ocean Surface Current Analyses-Real time (OSCAR) and sea surface temperature is from Extended Reconstructed Sea Surface Temperature (ERSST).....19

**Figure 2.3** Map showing climatological (2001-2010) distribution of dust optical depth over the Arabian Sea along with the locations of the surrounding dust source regions. The shading (and the overlaid black contours) shows the dust optical depth generated using a regional climate model as described in Section 3.1. The red contours overlaid on Google Earth image indicate the regions where the modeled annual dust emission exceeds  $500 \text{ mg m}^{-2} \text{ day}^{-1}$  .....22

**Figure 2.4** An example of dust storm over the Persian Gulf due to the *Shamal* weather. This image has been captured by Moderate Resolution Imaging Spectroradiometer onboard Terra satellite on 01<sup>st</sup> July, 2011.....24

**Figure 3.1** Figure illustrating the difference in resolution between the driving reanalysis fields and the regional climate model. The finer resolution grid of RegCM4 is superimposed on the coarse resolution NCEP/NCAR reanalysis used to force the model.....**25**

**Figure 3.2** Horizontal (a) and vertical (b) grids used in RegCM4. (a) A representation of Arakawa B grid used in RegCM4 Model. The scalar quantities are calculated at the centre of the grid and the vector variables are calculated at the corners (b) Sigma pressure system used in RegCM4 Model (source: <http://aaron.boone.free.fr/aspdoc/node7.html>). The pressure levels follow the outline of the local terrain at lower levels, but tend to flatten out at higher levels....**26**

**Figure 3.3** Distribution of different categories of landcover within the model domain. The landcover categories are obtained from Global Land Cover Characteristics (GLCC) - Biosphere Atmosphere Transfer Scheme (BATS). The black stippling mark the landcover classified as “Desert” and “Semi-desert” from where dust emission takes place.....**28**

**Figure 3.4** Schematic representation of the working of the dust module in RegCM4 model.....**30**

**Figure 3.5** Time-series of dust and aerosol optical depth over the Arabian Sea (50-78°E and 10-25°N) for (left) MODIS/Aqua and (right) MODIS/Terra.....**34**

**Figure 4.1** Temporal coverage of different data that have been used to evaluate dust optical depth derived from RegCM4 model.....**41**

**Figure 4.2** Shading shows the spatial pattern of climatological (2001-2010) distribution of dust optical depth derived from (a) RegCM4 model, (b) MODIS/Terra and (c) MODIS/Aqua (for 2003-2010). The shading in (d) shows the climatological (2005-2010) distribution of Aerosol Index from OMI while that in (e) shows the total deep blue aerosol optical depth from MODIS/Aqua for the period of 2003-2010. The coloured boxes in (a) represents the four regions used to compare time-series of dust in Figure 4.4. The black squares in (e) indicate the locations of the AERONET stations that have been used for Figure 4.3.....**43**

**Figure 4.3** Time-series of daily aerosol optical depth for selected AERONET stations (in black) and dust optical depth generated by the RegCM4 model (in red). The locations of the stations are marked in Figure 4.2e. The time-series have been broken up into two parts for Sede Boker and Solar Village as the data in these stations are available for 10 years.....**47**

**Figure 4.4** Temporal evolution of dust optical depth over different regions of the Arabian Sea. The regions represented by each colour in the time series are indicated by the boxes in Figure 4.2a. The lines show the monthly climatology of dust optical depth obtained from MODIS/Terra observation for the period 2001-2010, while the small circles represent the same but for RegCM4.....**48**

**Figure 4.5** Spatial pattern of climatological (2001-2010) distribution of dust optical depth derived from (a) RegCM4 model, (b) MODIS/Terra and (c) MODIS/Aqua (for 2003-2010) during southwest monsoon (SWM, June-September). The shading in (d) shows the climatological (2005-2010) distribution of OMI Aerosol Index for SWM while that in (e) shows the deep blue aerosol optical depth from MODIS/Aqua for the SWM of 2003-2010.....**50**

**Figure 4.6** Comparison between the meteorological fields from NCEP/NCAR reanalysis used to force RegCM4 model (left) and simulated meteorological fields (right) during the southwest monsoon. Shown are wind speed (in shading, unit:  $m s^{-1}$ ) overlaid with the vectors (top panel), temperature (middle panel) (unit in  $^{\circ}C$ ) and relative humidity (bottom panel) (expressed as %) at 1000 mb pressure level for NCEP/NCAR reanalysis and 1008mb pressure level for RegCM4 simulation.....**51**

**Figure 4.7** Comparison of precipitation ( $mm day^{-1}$ ) between TRMM (left) and that generated using RegCM4 model (right) over the Arabian Sea and the surrounding regions for the southwest monsoon period.....**53**

**Figure 5.1** Seasonal cycle of dust emission in the regions surrounding the Arabian Sea for (a) northeast monsoon (b) spring intermonsoon (c) southwest monsoon and (d) fall intermonsoon.....**56**

**Figure 5.2** Map showing variation in elevation over the landmass surrounding the Arabian Sea.....**58**

**Figure 5.3** Time of the year when the maximum dust emission takes place in regions surrounding the Arabian Sea. The boxes mark the regions that have been taken up to study the meteorological conditions responsible for dust emission. The thick red line marks the position of the intertropical convergence zone during the southwest monsoon period demarcated as the zone where the meridional component of the wind becomes zero. The arrows mark the prevailing wind directions during the time of maximum dust emission over a region. The column graph shows average emission (unit  $\text{mg m}^{-2} \text{ day}^{-1}$ ) for each of the 11 regions denoted by the boxes....**59**

**Figure 5.4** Annual cycle of meteorological conditions that are associated with dust emission in the different regions surrounding the Arabian Sea. Shown are the fields for Region 1 to 4 as demarcated in Figure 5.3. The top panel for each region shows dust emission; the shadings in the middle panel shows the time versus height evolution of temperature and the blue curve shows the distribution of precipitation; the bottom panel shows the time versus height evolution of wind direction (shading) and wind speed (contours). All fields shown are daily climatologies that have been smoothed by ten days' running mean.....**62-63**

**Figure 5.5** Same as for Figure 5.4 but for Regions 5 to 8.....**66-67**

**Figure 5.6** Same as for Figure 5.4 but for Regions 9 to 11.....**69**

**Figure 5.7** Dust concentrations (shadings) and the dust mass flux vectors ( $\mu\text{g kg}^{-1} \text{ m s}^{-1}$ ) over the Arabian Sea during the southwest monsoon season for the different pressure levels at which maximum dust transport takes place. The red dashed lines in (a) indicate the sections along which dust concentration is depicted in Figure 5.8.....**72**

**Figure 5.8** The longitude-height variation of dust concentrations over the Arabian Sea during the northeast monsoon (top panel) and the southwest monsoon (bottom panel) period for  $10^\circ\text{N}$  (left),  $16^\circ\text{N}$  (centre) and  $24^\circ\text{N}$  (right) latitudes as marked by the red dashed lines in Figure 5.7a. The shading shows dust concentration, the contours are the fraction of dust that have diameter lesser than  $2.5 \mu\text{m}$  and the red dots mark the height at which maximum dust is concentrated.....**74**

**Figure 5.9** Magnitude of dust mass flux over the Arabian Sea during the southwest monsoon period. (a) Shading shows the latitude-height variation in the magnitude of dust mass flux along  $64^\circ\text{E}$  longitude and the contours show the contribution of the fraction of dust that have diameter less than  $2.5 \mu\text{m}$ . (b) Shading shows the concentration of dust at 267 mb pressure level and the

vectors are the wind direction. (c) Time versus height evolution of dust mass flux and (d) the corresponding wind directions within the box marked out in (b).....76

**Figure 5.10** Schematic representation of the different routes through which dust is transported over the Arabian Sea. The base map indicates the topography of the region generated from ETOPO-01. The red stippling indicates the regions where average dust emission exceeds  $1000 \text{ mg m}^{-2} \text{ day}^{-1}$ . The warm colour indicates dust transport routes during the southwest monsoon period and the cold colour indicates dust transport routes during the northeast monsoon period.....77

**Figure 5.11** Seasonal cycle of dust depositions (blue-red shading) over the Arabian Sea and surroundings for (a) northeast monsoon (b) spring intermonsoon (c) southwest monsoon and (d) fall intermonsoon. The contours mark the contribution of dry deposition to total deposition....79

**Figure 5.12** Distribution of precipitation over the Arabian Sea and surroundings during the northeast monsoon (left) and southwest monsoon (right).....79

**Figure 6.1** Climatological (1979-2013) distribution of AI-1.5, precipitation and soil moisture over the Arabian Sea and the surrounding landmass. Shadings in (a), (b) and (c) show AI-1.5, precipitation and soil moisture respectively and the black contours are their standard deviations. The white dashed line in (a) shows the mean position of the ITCZ determined as the location where the northward component of the wind becomes zero during boreal summers. The red box in (a) represents the region SAME which has been taken up for further study. The temporal evolution of AI, precipitation and soil moisture over SAME is depicted in (d). Thick red curve shows the daily climatology of AI with the standard deviations of AI represented by the shaded region. The tiny blue squares indicate monthly climatology of precipitation plotted along with their error bars. The hollow black rectangles are the monthly mean climatology of the soil moisture. The numbers below the rectangles indicate the standard deviations of soil moisture...83

**Figure 6.2** Time-series of anomalies of AI-1.5, soil moisture and precipitation (rectangles) and NINO3.4 and IOD index (dashed lines). The NINO3.4 and IOD index of previous years are collocated with the current years' anomalies. The 4 El Nino (EN) and 7 La Nina (LN) years when AI data are available are indicated on top and the bottom of the anomaly respectively.....86

**Figure 6.3** Map showing spatial pattern of the correlation between (a) ENSO and AI-1.5 and (b) ENSO and precipitation and soil moisture. (a) Shading shows the distribution of correlations

between ENSO and AI-1.5. The black and red dashed contours enclose the regions where the correlation exceeds 95% and 99% significance levels respectively. (b) Shaded map shows the correlation between NINO3.4 and precipitation from October-May. Only the regions that have correlation coefficient exceeding 95% significance level are shaded, while the stippling encloses the regions that have correlation coefficient exceeding 99% significance level. The red contours marked 0.33 and 0.43 indicate the regions that have correlation between NINO3.4 and soil moisture (October-May) exceeding 95% and 99% significance levels respectively.....**89**

**Figure 6.4** Comparison of anomalies of vertically integrated specific humidity, moisture flux (a and c), OLR and wind vectors (b and d) during December to March of El Nino (a and b) years and La Nina (c and d) years. Anomalous conditions during El Nino (La Nina) years are obtained by differencing the meteorological fields during the years when NINO3.4 index exceeded value of 1.0 (less than -1.0) from the years when NINO3.4 index was between -1 and +1. The blue (red) shades in (a) and (c) indicate positive (negative) vertically integrated specific humidity anomaly (expressed as  $\text{g kg}^{-1}$ ) and the vectors are the vertically integrated moisture flux anomaly (expressed as  $\text{kg kg}^{-1} \cdot \text{m s}^{-1}$ ). The shading in (b) and (d) show the anomaly in OLR. The vectors are the wind anomaly (horizontal and vertical) at 300 mb pressure level. The vertical component of wind anomaly has been multiplied by 10. For specific humidity and OLR, anomalies at 95% significance levels are shown. The black contours enclose the regions where the magnitude of vertically integrated moisture flux anomaly exceeds 95% significance level.....**93**

**Figure 6.5** Relation between ENSO, AI-1.5 and geopotential height during the summer following an ENSO. (a) Shading shows correlation between NINO3.4 index and geopotential height at 300 mb for April to August of the following year. The regions exceeding 95% and 99% significance levels are shown by red contours marked as 0.33 and 0.43 respectively. The white contours enclose the regions where correlation between NINO3.4 and precipitation for April to August exceeds 95% significance level. Continuous contours are for positive and dashed contours are for negative correlations. The stippling indicates the regions where correlation between NINO3.4 and precipitation exceeds 99% significance level. (b) Difference in geopotential height at 300 mb pressure level between years having positive AI-1.5 anomaly and negative AI-1.5 anomaly. Red (blue) shades show the regions of positive (negative) anomaly. The contours enclose the regions having anomaly greater than 95% significance level.....**95**

**Figure 6.6** Anomaly of AI-1.5 during the years following La Nina. The contours enclose the regions that have anomaly significant at 95%.....**97**

**Figure 6.7** Anomaly diagrams for vertically integrated specific humidity, moisture flux, OLR and wind vectors. (a) Shadings show anomalies in vertically integrated specific humidity (expressed as  $\text{g kg}^{-1}$ ) and the vectors indicate vertically integrated moisture flux (expressed as  $\text{kg kg}^{-1}$ )

kg<sup>-1</sup>\*m s<sup>-1</sup>) during a positive IOD year. The blue (red) shades show the regions where the positive (negative) anomaly of vertically integrated specific humidity exceeds 95% significance level. The black contours enclose the regions where the magnitude of vertically integrated moisture flux anomaly exceeds 95% significance level. (b) Representation of the conditions prevailing after subtracting the conditions prevailing during positive IOD years from the El Nino years. The shading on the horizontal plane represents the OLR anomaly at 95% significance level. The vectors are the wind anomaly (horizontal and vertical) at 300 mb pressure level. The vertical component of wind anomaly has been multiplied by 10.....**99**

**Figure 7.1** (a) Spatial distribution of correlation coefficient between  $\tau_{du}$  and (b) climatological mean chlorophyll *a* (Chl *a*) concentration (mg m<sup>-3</sup>) for the NEM of 2002-2003 to 2010-2011 over the AS. In (a) the thick white contours indicate the region having coefficient of correlation between  $\tau_{du}$  and Chl *a* greater than 0.5. The black contours show the distribution of the correlation coefficient between  $\tau_{du}$  and Fluorescence Line Height (FLH). The green box outlines the region central Arabian Sea (CAS), which is considered for studying the effect of episodic dust storms on phytoplankton biomass. The dashed black box demarcates north AS (NAS) (see the text). In (b) the contours indicate the climatological distribution of  $\tau_{du}$  and the vectors represent the current (in m s<sup>-1</sup>) during the same period.....**103**

**Figure 7.2** Climatological (2002-3003 to 2010-2011) mixed layer depth (MLD) during the NEM time for NAS (upper panel) and CAS (lower panel). The blue squares are the MLD calculated from Argo data to which a third order polynomial curve was fitted for NAS and a second order polynomial curve was fitted for CAS as indicated by the blue curves. Daily climatology of modeled MLD is shown by the black lines.....**105**

**Figure 7.3** (a) Climatological mean distribution of surface nitrate during the northeast monsoon (shading) overlaid with contours of SST from World Ocean Atlas 2009 (WOA09) and (b) north-south gradient in nitrate values obtained from JGOFS measurements during January overlaid with SST contours from WOA09.....**106**

**Figure 7.4** Simulated dust depositions (mg m<sup>-2</sup>) for the episodic dust storms using RegCM4 model. The black contours indicate the difference between  $\tau_{du}$  sensed from MODIS/Aqua and model simulation. The value of the thick contour is 0. All contour intervals are 0.1. Continuous contours indicate positive difference and dashed contours indicate negative difference. The white square indicates the study region CAS.....**108**

**Figure 7.5** Time-series of 3-day averaged chlorophyll *a* (Chl *a*) concentration ( $\text{mg m}^{-3}$ ) and mixed layer depth (MLD) in central Arabian Sea (CAS) region for the winter monsoon of 2002-2003 to 2010-2011. The green dashed line shows the 3-day Chl *a* climatology and the vertical lines represent their 2 standard deviations; the red squares are the Chl *a* concentrations for each corresponding year; the blue line is the MLD; the black squares indicate the windows when dust storms were observed by satellite around CAS and the hollow black rectangles indicate the cases of Chl *a* enhancement when Chl *a* exceeded 2 SD level. The numbers on the top of the rectangles indicate the episode numbers which are referred in the text as E1, E2 and so on.....**110**

**Figure 7.6** Schematic representation of the time evolution of mixed layer in the Arabian Sea during the northeast monsoon and its association with the episodic chlorophyll enhancements. E1 to E8 indicates the numbers of the episodes of chlorophyll enhancements.....**111**

**Figure 7.7** Matrix showing the possible scenarios when observed phytoplankton bloom can be ascribed to be driven by dust depositions and oceanic supply of DFe under varying Fe dissolution threshold and Fe/C ratio. The episodes listed in black are entirely supported by oceanic DFe. The episodes listed in red need an atmospheric source of DFe. The episodes that have not been listed are the ones which cannot be supported even with the atmospheric and oceanic sources of DFe taken together.....**120**

**Figure 7.8** Schematic diagram showing the mechanism leading to chlorophyll *a* enhancement in the central Arabian Sea following dust storms during the northeast monsoons (see text for explanation).....**121**

**Figure 7.9** Mean northeast monsoon time chlorophyll *a* concentration ( $\text{mg m}^{-3}$ ) for (a) heavy dust years (2003-2004, 2006-2007 and 2007-2008) and (b) less dust years (2002-2003, 2004-2005, 2005-2006, 2008-2009, 2009-2010 and 2010-2011) within central Arabian Sea.....**124**

**Figure 7.10** Distribution of correlation coefficient between dust optical depth and chlorophyll *a* concentration over the AS (shading) for the spring intermonsoons of 2003-2011. The black contours enclose the regions where the correlation between dust optical depth and FLH exceeds a magnitude of 0.4: continuous contours for positive correlation and dashed contours for negative correlation.....**126**

**Figure 7.11** Spatial distribution of correlation coefficient between dust optical depth and chlorophyll *a* concentration over the AS (shading) for the southwest monsoons of 2003-2011. The black contours enclose the regions where the correlation between dust optical depth and

FLH exceeds a magnitude of 0.4: continuous contours for positive correlation and dashed contours for negative correlation.....127

**Figure 7.12** Spatial distribution of correlation coefficient between dust optical depth and chlorophyll *a* concentration over the AS (shading) for the fall intermonsoons of 2003-2011. The black contours enclose the regions where the correlation between dust optical depth and FLH exceeds a magnitude of 0.4: continuous contours for positive correlation and dashed contours for negative correlation.....128

# List of Tables

<b>Table 3.1</b> Configurations used for simulating dust cycle using RegCM4 Model.....	<b>30</b>
<b>Table 5.1</b> Dust emissions in the regions around the Arabian Sea (0-36°N latitude, 32-75°E longitude) during different seasons.....	<b>57</b>
<b>Table 5.2</b> Dust depositions into the Arabian Sea (5-25°N latitude, 50-78°E longitude) during different seasons.....	<b>80</b>
<b>Table 6.1</b> Correlation coefficients between climate modes and AI-1.5, precipitation and soil moisture.....	<b>88</b>
<b>Table 7.1</b> Estimated dust deposition in the CAS following dust storms and the possible amount of nutrients that can be derived from dust.....	<b>109</b>
<b>Table 7.2</b> Nutrient requirements for the observed surface Chl <i>a</i> enhancements in CAS.....	<b>111</b>

## List of Abbreviations

AERONET	Aerosol Robotic NETwork
AI	Aerosol Index
AMSR-E	Advanced Microwave Scanning Radiometer - Earth Observing System
AMSU-B	Advanced microwave sounding unit
AS	Arabian Sea
ASCAT	Advanced Scatterometer
ASHSW	Arabian Sea High Salinity Water
BATS	Biosphere-Atmosphere Transfer Scheme
CAS	Central Arabian Sea
Chl <i>a</i>	Chlorophyll <i>a</i>
DMI	Dipole Mode Index
EP	Earth Probe
E-P	Evaporation minus precipitation
ENSO	El Nino-Southern Oscillation
ERSST	Extended Reconstructed Sea Surface Temperature
FIM	Fall intermonsoon
FLH	Fluorescence Line Height
GCM	General Circulation Model
GLCC	Global Land Cover Characteristics
HNLC	High-nutrient-low-chlorophyll
INDOEX	Indian Ocean Experiment
IO	Indian Ocean
IOD	Indian Ocean Dipole
IPWP	Indo-Pacific warm pool
ITCZ	Intertropical convergence zone
JGOFS	Joint Global Ocean Flux Studies
MHS	Microwave Humidity Sounder

MLD	Mixed layer depth
MODIS	Moderate Resolution Imaging Spectroradiometer
NAS	Northern Arabian Sea
NCAR	National Center for Atmospheric Research
NCEP	National Centers for Environmental Prediction
NEM	Northeast monsoon
OAFflux	Objectively Analyzed air-sea Fluxes
OC3M	Ocean Chlorophyll three-band Algorithm for MODIS
OLR	Outgoing longwave radiation
OMI	Ozone Monitoring Instrument
OND	October November December
OSCAR	Ocean Surface Current Analyses-Real time
PGW	Persian Gulf Water
PWP	Price-Weller-Pinkel
QuickSCAT	Quick Scatterometer
RegCM4	Regional Climate Model Version 4
RSW	Red Sea Water
SAME	Southwest Asia and the Middle East
SD	Standard deviation
SIM	Spring intermonsoon
SON	September October November
SSMI	Special Sensor Microwave Imager
SSMIS	Special Sensor Microwave Imager Sounder
SST	Sea surface temperature
SUBEX	Subgrid Explicit Moisture Scheme
SWM	Southwest monsoon
TOMS	Total Ozone Mapping Spectrometer
TRMM	Tropical Rainfall Measuring Missions
USDA	United States Department of Agriculture
WICC	West India coastal current
WOA09	World Ocean Atlas 2009

## List of Publications from the thesis

**Banerjee, P.** and Prasanna Kumar, S. (2014). Dust depositions leading to phytoplankton blooms in the Arabian Sea, SOLAS Newsletter, 16, 13-14.

**Banerjee, P.** and Prasanna Kumar, S. (2014). Dust-induced episodic phytoplankton blooms in the Arabian Sea during winter monsoon, Journal of Geophysical Research (Oceans), 119, 7123-7138, doi:10.1002/2014JC010304.

**Banerjee, P.** and Prasanna Kumar, S. ENSO modulation of interannual variability of dust aerosols over the northwest Indian Ocean, (under review in Journal of Climate).

# CHAPTER 1

## INTRODUCTION

### 1.1. Mineral dust in the climate system

Atmospheric aerosols are tiny particles of solid or liquid suspended in the atmosphere and can range in size between few nanometres to up to a millimetre. They can be either from natural sources (example soil dust, sea salt, volcanic eruption, biological matters) or from anthropogenic sources (example industrial emissions, soot, biomass burning and organics from volatile organic carbon) [Poschl, 2005]. Mineral dust is an important component of the atmospheric aerosol affecting the climate system manifold. According to the Fifth Assessment Report of the Intergovernmental Panel on Climate Change, the global emission of mineral dust varies between 1000 and 4000 Tg year<sup>-1</sup> [Stocker et al., 2014], that is, from 34% to 31% of the total natural aerosols. Figure 1.1 gives a view of the different types of aerosols that are present in the atmosphere.

The main sources of the mineral dust are the arid and semi-arid regions of the globe [Prospero et al., 2002]. Dust can also be emitted from those regions where anthropogenic activities have significantly modified the natural vegetated land cover and have resulted in desertification [example Ginoux et al., 2010; 2012]. Anthropogenic contributions to the dust load can vary from less than 10% [Tegen et al., 2004] to more than 50% [Mahowald and Luo, 2003]. The main dust sources of the globe lie in the northern hemisphere with the Sahara Desert in North Africa as the largest source of dust to the atmosphere [see Mahowald et al., 2005 and the references therein].

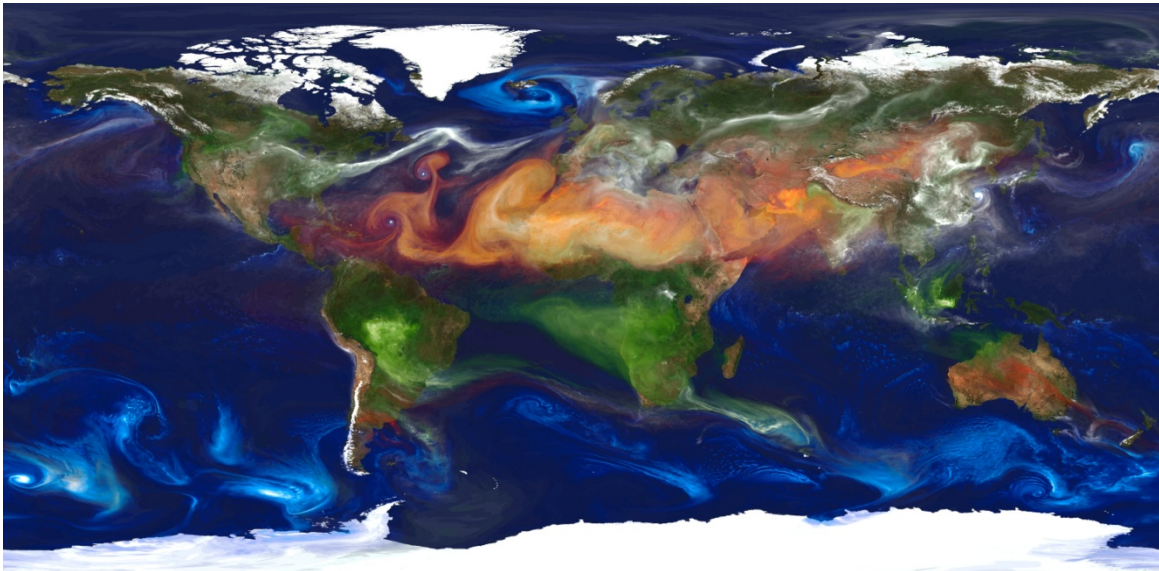


**Figure 1.1** Global distribution pattern of main types of aerosols present in the atmosphere. Red indicates dust aerosols, blue: sea salt, white: sulphate aerosols and green: biomass burning aerosols. (Image courtesy NASA Goddard Space Flight Center).

Dust emissions in North Africa ranges between 204 and 2888 Tg year<sup>-1</sup> [Huneus *et al.*, 2011]. This is followed by dust emissions from the deserts of central Asia, deserts of west Asia and the Middle East. Emission ranges are 26 to 531 Tg year<sup>-1</sup> for Middle East and 27 to 837 Tg year<sup>-1</sup> for central Asia [Huneus *et al.*, 2011]. The southern hemisphere is a minor source of dust to the globe with the main contributions coming from the Patagonian Desert in South America [Li *et al.*, 2010; Johnson *et al.*, 2011] and the Australian Desert [Raupach *et al.*, 1994]. Estimations of dust emissions over South America ranges between 0.2 and 186 Tg year<sup>-1</sup>, while those over Australia ranges between 9 and 129 Tg year<sup>-1</sup> [Huneus *et al.*, 2011]. Because dust can be carried to remote places (often from one continent to another) by the prevailing wind system [example Perry *et al.*, 1997; Uno *et al.*, 2009; Badarinath *et al.*, 2010], it can affect the climate of places far removed from the dust sources. The lifetime of dust in the free Troposphere can vary from few hours to about a week [Zender *et al.*, 2004]. Mineral dust aerosols can impact the hydrological cycle by acting as cloud condensation nuclei [example Rosenfeld *et al.*, 2001;

*Creamean et al.*, 2013] and can affect the radiative balance of a region both directly [*Miller et al.*, 2004] by heating the dust layer and indirectly by effecting the level of cloudiness [*Lohmann and Feichter*, 2005]. *Mahowald et al.* [2010] have calculated a change in the mineral dust radiative forcing between 1750 and 2000 as  $-0.14 \pm 0.11 \text{ W m}^{-2}$ . Mineral dust have been given attention due to its potential role in fertilizing the ocean by supplying micronutrient iron and, thereby, influencing carbon export [example *Bishop et al.*, 2002; *Jickells et al.*, 2005; *Maher et al.*, 2010; *Martinez-Garcia et al.*, 2011]. Soil dusts are also of serious concern because the impact they have on the human respiratory system [*Griffin and Kellogg*, 2004]. In recent years, studies have also shown that dust can significantly impact tropical cyclone activity (negatively) by stabilizing the atmosphere [*Dunion and Velden*, 2004; *Evan et al.*, 2006]. More interestingly, it has been shown that dust and other aerosols together account for 69% of the upward trend of the North Atlantic Ocean mixed layer temperature [*Evan et al.*, 2009] and that aerosols are the largest driver of the North Atlantic Ocean climate variability [*Booth et al.*, 2012].

It has been estimated by several studies that the dust load during the glacial period was 2-20 times higher than the present [*Kohfeld and Harrison*, 2001]. It is conceived that, in all its probability, dust must have played a very important role in changing the climate of the past by supplying iron that led to high production and drawdown of atmospheric carbon dioxide during the last glacial maximum [*Martin*, 1990]. The main routes through which dust can impact the climate system is illustrated with the help of a schematic diagram in Figure 1.2. Thus, the understanding of the variability of mineral dust and how it can impact the climate is a key step in assessing how the climate of a region will respond to global warming.

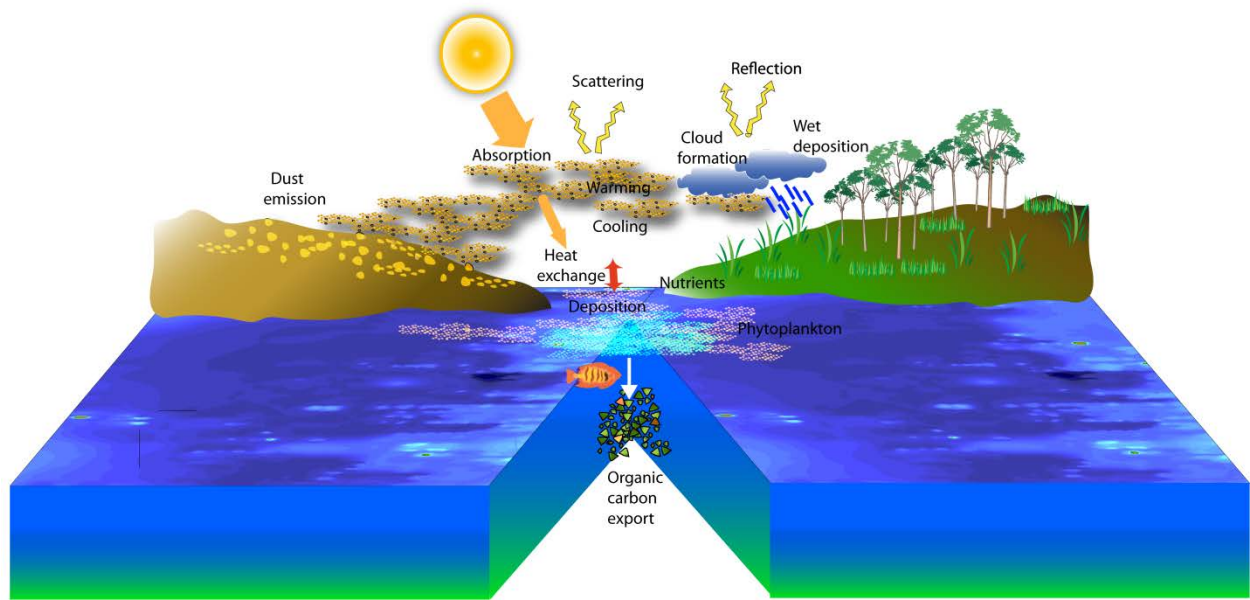


**Figure 1.2** Schematic representations of some of the different ways in which dust can influence the climate.

## 1.2. Dust over the Arabian Sea

Dust storms have affected the lives of inhabitants around the northwest Indian Ocean (IO) for centuries. The action of the forceful wind in tossing up soil particles has fascinated the curious minds and many explanations have been sought to understand this idiosyncrasy of nature. In the Vedas, mentions have been made of dust whirled up in the air due to the passage of the deity of wind *Vayu*, also known as *Vata* or *Pavan*:

*Sublime and shining is the car of Vata;  
It sweeps resounding, thundering and crashing;  
Athwart the sky it wakens ruddy flashes,  
Or o'er the earth it sets the dust-clouds whirling  
.....Rigveda, x, 168*

Most of the reports in the early literature related to dust storms have been anecdotal and scientific investigations have been very limited. They have been largely based on the accounts of

travellers, merchants and explorers who had traversed the lengths of the deserts. One of the earliest studies of dust storms in this region had been done by P.F.H. Baddeley in his book “Whirlwinds and Duststorms of India” published in 1860. In this book he had provided a vivid description of his encounter with a dust storm in northwest India:

*We take our stand, and observe in the distance several lofty pillars of dust moving towards us with a somewhat tortuous course, and we plant ourselves so as to meet one of them. The air about us is perfectly still up to the time of the whirlwind’s approach; but the instant it strikes us, we are encompassed with conflicting winds and a cloud of dust. The whirl has passed; and we next notice a train of dust broken into minute tortuous eddies following in its wake for several yards; and experience for a short time, during which the whirlwind may have progressed 100 or 200 yards, light fluttering winds, or a calm; and then, all at once, a strong breeze blows steadily in the direction of the whirlwind for some minutes, with, now and then, a diminution or an increase in the strength of the blast. Afterwards the wind veers and becomes unsteady, and finally subsides into a calm. The same process is repeated over and over again, as long as the whirlwinds last.*

Subsequently, the investigations into dust entrainment in the atmosphere had a slow but steady evolution. The efforts towards this have been punctuated by the inaccessibility and the volatile history of the region. However, data from different weather stations scattered across the Middle East, southwest Asia and south Asia provided valuable basis for studying the meteorological conditions responsible for spawning dust storms. Perhaps one of the first scientific descriptions of dust storm around the Arabian Sea (AS) was provided by *Perrone* [1979] who described the synoptic conditions associated with a winter time *Shamal* weather system in the Persian Gulf. These *Shamals* or northwesterly winds have been regarded as the main dust-raising winds in the Gulf region. *Membery* [1983] reported the presence of low-level jet over the Persian Gulf during the summer *Shamals* in the leeward side of the Zagros Mountains which were much stronger during the daytime compared to night.

One of the most important works that describes the nature of dust storms is by *Middleton* [1986] based on meteorological stations data. Maximum dust activity has been associated with the dry months of spring and summer, while the maximum frequency of dust storms was reported from Zabol in Iran. However, *Middleton* [1986] did not take Iraq or the Arabian Peninsula into his analysis. Ship-based measurements along the western AS led to the conclusion that mineral dust comprises a significant fraction of sediments off the Horn of Africa and the Arabian Peninsula with mineral aerosol concentration of  $7.6 \mu\text{g m}^{-3}$  during dust outbreaks [*Savoie et al.*, 1987]. Similar notion emerged from the work by *Chester et al.* [1991] who measured Al (aluminium, an indicator for dust) concentration exceeding  $1000 \text{ ng m}^{-3}$  of air in the AS. This yielded mineral dust concentrations of about  $15 \mu\text{g m}^{-3}$ . *Ackerman and Cox* [1989] analysed the surface weather conditions associated with dust storms during the southwest monsoons and have concluded that for most of the stations dust uplift and transport is accomplished by the mean wind. An analysis of the climatic factors led *Littman* [1991] to conclude that although spring and summer are the preferred time for dust storms, there is hardly any correlation between climatic factors and the frequency of dust storms. However, there are some indications that rainfall and its frequency probably has influence on dust storms of the Middle East; wind speed is important for southwest Asia and the mean maximum temperature is a controlling factor for dust storm generation is India.

During the Joint Global Ocean Flux Studies (JGOFS) carried out between 1994 and 1996, ship-based investigations of dust fluxes were carried out to study the seasonal cycle of dust more intensively and to be able to quantify the dust flux. Taking Al as an indicator of mineral dust, maximum dust deposition of  $2\text{-}7 \text{ g m}^{-2}$  was calculated for July-August period [*Measures and Vink*, 1999]. However, maximum dust deposition was calculated in the central and southern AS

in contrast to northern and western AS. On the contrary, *Tindale and Pease* [1999] reported maximum concentration of mineral dust during the winter time as opposed to earlier studies citing that the low level Findlater Jet during the southwest monsoon time might block the transit of dust into the open AS. They also proposed that dust transport at higher levels in the atmosphere might be more important during the summer time. It was also supported by *Siefert et al.* [1999] who showed that the air parcel trajectory during the southwest monsoon was predominantly maritime with little crustal materials. They reported that during the spring intermonsoon time air parcel came from Africa and Arabian Peninsula carrying more crustal materials. Based on sediment trap records annual dust depositions were seen to vary between  $\sim 12 \text{ g m}^{-2} \text{ year}^{-1}$  in the western AS to  $1.5 \text{ g m}^{-2} \text{ year}^{-1}$  in the southern AS [*Clemens*, 1998].

Satellite remote sensing, numerical modeling in conjunction with concerted field campaigns led to significant progress in quantifying the distribution of dust and its effect on the climate of the IO. The significance of atmospheric aerosols in modulating the radiative balance over the AS was brought to light during the Indian Ocean Experiment (INDOEX) conducted during January to March 1999. A net decrease in solar radiative forcing of  $10\text{-}20 \text{ W m}^{-2}$  at the surface was estimated due to presence of aerosols [*Krishnamurti et al.*, 1998]. In their seminal work *Prospero et al.* [2002] described the characteristics of the dust source regions. The principal dust source regions were attributed to as topographic lowlands associated with fluvial activities which are important in generating fine sediments for wind to pick up. Compiling results from several model studies *Mahowald et al.* [2005] estimated that the IO receives 8 to 32% of the global ocean dust depositions ranging from 29 to 154 billion  $\text{kg year}^{-1}$ . Based on multiple satellite and model studies by *Zhu et al.* [2007] important information about the radiative forcing by dust during southwest monsoon emerged: (i) a shortwave heating of  $0.5 \text{ K}^{-1} \text{ day}$  took place within the

dust layer over AS (ii) a net top of the atmosphere radiative forcing (shortwave+longwave) of  $-7.0 \text{ W m}^{-2}$  (iii) a surface radiative forcing of  $-17.8 \text{ W m}^{-2}$  and (iv) a net radiative gain of  $10.8 \text{ W m}^{-2}$  within the dust layer. An important implication of the dust induced atmospheric heating is with respect to its capability to alter the monsoon system. It has been proposed that the presence of absorbing aerosols like dust in the atmosphere can act as an “elevated heat pump” which leads to more vigorous monsoon circulation and increased rainfall during the beginning of the monsoon season [Lau and Kim, 2006]. An increase in the pre-monsoon high cloud cover along with a decrease in low cloud cover have been attributed to an increase in absorbing aerosols over the Indo-Gangetic plain [Lal et al., 2013]. The heating as well as the microphysical effect of dust leading to an increase in short-term rainfall over central India has been experimentally shown [Vinoj et al., 2014]. Thus, the interest in understanding the transport and temporal variability of dust peaked with these findings that demonstrated the effects of dust on the climate of the IO.

An investigation into how dust transport is accomplished and what factors are relevant in driving the interannual variability of dust over the AS and its surroundings have been, however, far less and isolated. Rahul et al. [2008] have shown that, in general, there is higher aerosol loading over the AS during the years when the Indian summer monsoon is normal compared to those years when there is drought over India. El Nino conditions have been associated with increased dust transport from the Middle East to the Indian subcontinent by the strengthened westerlies [Abish and Mohanakumar, 2013]. Over the Sistan region of Iran, no significant relation between summertime El Nino-Southern Oscillation (ENSO) and dust storms have been discerned [Kaskaoutis et al., 2014].

### 1.3. Dust and phytoplankton in the Arabian Sea

Apart from influencing the radiative budget and the hydrological cycle of the earth, mineral dust has an important implication in the biogeochemistry of the oceans. This is the impact of dust on the primary productivity of the open ocean regions by supplying nutrients, especially micronutrient iron (Fe), leading to drawdown of atmospheric carbon dioxide [*Martin and Fitzwater, 1988; Bishop et al., 2002; Jickells et al., 2005; Gabric et al., 2010*]. AS is one of the most productive regions of the world oceans due to wind driven coastal upwelling in the western AS during southwest monsoon and convective mixing during the northeast monsoon in the northern AS. The mean annual primary productivity in the AS is estimated to be about  $111 \pm 11 \text{ mmol C m}^{-2} \text{ day}^{-1}$  [*Barber et al., 2001*].

The findings of the JGOFS based on *Measures and Vink [1999]* led *Smith [2001]* to conclude that the AS probably is Fe replete due to high dust depositions. However, a possibility of Fe limitation during the late southwest monsoon period emerged through the studies of *Wiggert and Murtugudde, [2007]* and *Naqvi et al. [2010]*. Using primarily satellite data few studies have tried to show the effect of dust deposition on phytoplankton from daily [*Singh et al., 2008*] to seasonal [*Patra et al., 2007*] time scales. *Singh et al. [2008]* reported phytoplankton blooms in the northern AS following the passage of individual dust storms for the period December 2003 to December 2006. However, an ambiguity remains regarding the provenance of the nutrients that fuelled these blooms as they also found a decrease in sea surface temperature (SST) due to increased wind mixing during these dust storms. *Patra et al. [2007]* postulated that the region of high chlorophyll *a* (Chl *a*) during southwest monsoon coincides with the region having high dust supply rather than the region of strong upwelling. They also concluded that although the eastern

AS receives higher oceanic nutrients during northeast monsoon compared to southwest monsoon, high Chl *a* is observed during southwest monsoon compared to northeast monsoon period because of higher dust supply during southwest monsoon.

An annual increase in Chl *a* in the AS for the time period of 1997-2007 is speculated to be boosted by an increasing mineral dust supply [*Prasanna Kumar et al.*, 2010]. Studies also show that only 0.02-0.4% of the Fe in the aerosols over the AS is soluble [*Srinivas et al.*, 2011] implying very little bioavailability of Fe in dust. *Seifert et al.* [1999] reported less than 4% of Fe in aerosols was soluble and indicated the possibility of atmospheric processing of the Fe. These studies points to the wide range of solubility of Fe present in dust. In the northwest AS for example, where the dust deposition can be around  $12 \text{ g m}^{-2} \text{ year}^{-1}$  [*Clemens et al.*,1998], such wide range of Fe solubility results in a wide range of dissolved Fe flux roughly varying between 300 and  $15 \mu\text{mol m}^{-2} \text{ year}^{-1}$ . At a greater distance from the dust sources near the southern AS, about  $1 \text{ g m}^{-2} \text{ year}^{-1}$  of dust deposition can result in dissolved Fe flux of about 25 to  $1 \mu\text{mol m}^{-2} \text{ year}^{-1}$ . A similar notion could be arrived at from extensive studies in other regions of the globe where Fe solubility has been seen to range from 0.01 % to 90% [see Table S3 of *Mahowald et al.*, 2005]. Overall, the amounts of Fe supplied by dust and its bioavailability are subject to high uncertainty.

#### **1.4. Aims of the present study**

It appears from the previous sections that dust aerosols play a crucial role in perturbing the climate over the entire north IO and the AS in particular. However, we are yet to get a holistic view of the dust cycle. There is currently no consensus on how the large scale climate modes might control the interannual variability of dust aerosols over the AS and its surroundings. Also,

while there has been compelling evidences from several parts of the globe that dust may influence the phytoplankton growth by supplying nutrients, such an understanding has not emerged from the AS, a region characterized by high levels of primary productivity and dust depositions. In this context, the following objectives have been set for the present thesis:

1. To decipher the temporal variability of mineral dust over the Arabian Sea and the factors responsible for the observed variability.
2. To examine the link between the variability of mineral dust and different climate modes.
3. To understand how the chlorophyll biomass responds to dust deposition in the Arabian Sea.

Objective 1 has been attempted at by studying the seasonal cycle of dust emission, transport and deposition using a regional climate model. Objective 2 has been studied at interannual scale by using satellite data and by trying to link how El Nino-Southern Oscillation and the Indian Ocean Dipole might affect the levels of dust activity in the AS and the surroundings. Objective 3 has been studied by giving maximum stress on the northeast monsoon period. This objective tries to understand if any chlorophyll response can be attributed to episodic dust depositions.

## **1.5. Thesis Outline**

The thesis investigates the spatial and temporal variability of mineral dust aerosols over the Arabian Sea (AS) and how it influences phytoplankton biomass in this region using a combination of satellite data and a regional climate model. The organization of the work is detailed as under.

Chapter 2 describes in detail the specific characteristics of the AS. More specifically, Section 2.1 describes the climate of the AS and the surrounding landmass with respect to the monsoon wind circulations. Section 2.2 explains how the monsoon system effects the seasonal cycle of the upper ocean circulation and the primary productivity in the AS. Section 2.3 describes the geography of the principal dust source regions surrounding the AS.

Chapter 3 introduces the data that have formed the foundations of the thesis. The description of the regional climate model RegCM4, that has been used to simulate the dust cycle, is provided in Section 3.1. A one-dimensional mixed layer depth model used to study the state of the water column is described in Section 3.2. The various remote sensing data that have been used to understand the dust levels in the atmosphere are explained in Section 3.3, while Section 3.4 briefly explains other supporting data used for the purpose of this thesis.

Chapter 4 is devoted to an extensive validation of the model and pointing out the model shortcomings using a suite of satellite and ground-based aerosol data.

Chapter 5 describes the seasonal cycle of dust over the AS as simulated by the regional climate model. Section 5.1 describes dust emission and the meteorological factors that are responsible. Section 5.2 focuses on dust transport routes over the AS giving maximum emphasis on the southwest monsoon season. Section 5.3 tries to quantify season-wise dust depositions, both wet and dry.

Chapter 6 focuses on the influence of different climate modes in modulating the interannual variability in dust activity surrounding the AS. The influence of El Nino-Southern Oscillation in remotely controlling the dust activity is discussed in Section 6.1, while that of the Indian Ocean Dipole is discussed in Section 6.2.

Chapter 7 details the impact of dust depositions on the phytoplankton biomass of the AS. Section 7.1 looks into the dust-phytoplankton relation during the northeast monsoon time by considering the nutrients that can be supplied by dust. Section 7.2 briefly describes the possible influence of dust on the phytoplankton biomass during other seasons.

Finally, the main findings of the thesis are summarized in Chapter 8. The chapter outlines the significance of the findings in understanding the climate system and the future works that can be vested in this field.

## **CHAPTER 2**

# **STUDY REGION**

### **2.1. Climate of the Arabian Sea**

The AS, the northwest part of the northern IO, has inherited much uniqueness in its climatic and oceanographic features by the virtue of its location. The presence of the Eurasian landmass has blocked the corridor to the polar oceans in the north. The high annual range of temperature and pressure that develop between the boreal winters and summers are of the order of 20°C and 16 mb respectively. This extreme range of temperature and pressure induces the intertropical convergence zone (ITCZ) to annually undergo north-south migration of about 35 degrees. Such a large range of latitudinal migration by the ITCZ has resulted in the most important climatic feature of the AS, the monsoonal pattern of seasonally reversing wind system. The prevailing winds are southwesterlies between May and September and northeasterlies between November and March. The intervening months are transitional periods between the two monsoons experiencing weak and variable winds. Since the response of the upper ocean to the prevailing wind system is often delayed, the classification of the seasons has to be done with caution. Throughout this thesis, except otherwise mentioned, southwest monsoon (SWM) refers to the period from June to September; spring intermonsoon (SIM or just spring) refers to April and May; northeast monsoon (NEM) refers to December to March and fall intermonsoon (FIM or just fall) refers to October and November. Boreal summer is defined as the period from April to September and boreal winter is defined as the period from October to March.

### 2.1.1. The southwest monsoon

During the months of April and May, due to high heating over the Eurasian landmass, an intense low pressure centre with pressure less than 1000 mb develops that stretches between 40-100°E longitude and 15-38°N latitude. The pressure difference between this Indo-Iranian low and the Mascarene high pressure region (located in the subtropical southern IO) results in the flow of the moisture-laden SWM wind over the northern IO (see Figure 2.1a). The SWM season is characterized by strong southwesterly winds exceeding a speed of  $12 \text{ m s}^{-1}$ . The highest wind stress exceeding  $0.4 \text{ N m}^{-2}$  is seen during this season with maximum value off the coast of Somalia. Near the southwest coast of India the wind direction is from west-northwest [Shetye *et al.*, 1990]. The core of the strongest wind during the SWM is called the Findlater Jet [Findlater, 1969] that follows Somali-Gujarat axis. Positive wind stress curl of magnitude exceeding  $1.0 \times 10^{-7} \text{ Pa m}^{-1}$  prevails to the north of the Findlater Jet and a negative wind stress curl of magnitude less than  $-2.0 \times 10^{-5} \text{ Pa m}^{-1}$  prevails to its south. SWM is responsible for bringing heavy rains to the Indian subcontinent. Maximum rainfall is recorded along the west coast of India due to the orographic effect of the Western Ghats that rise to a height of more than 500m within a distance of few kilometres from the coast and results in a mechanical lifting of the moisture-laden airmass. The average rainfall during SWM along the west coast of India can exceed  $30 \text{ mm day}^{-1}$ . The amount of rainfall decreases drastically towards the west to a value of less than  $1 \text{ mm day}^{-1}$ . To the west and north of the ITCZ, however, dryness prevails as any source of moisture is absent. Some of the most arid regions in the world are located here where the temperature soars more than  $40^\circ\text{C}$ . The surface wind direction here is northerly over Iran, Pakistan and Afghanistan turning to northwesterly over the Arabian Peninsula and eastern part of North Africa.

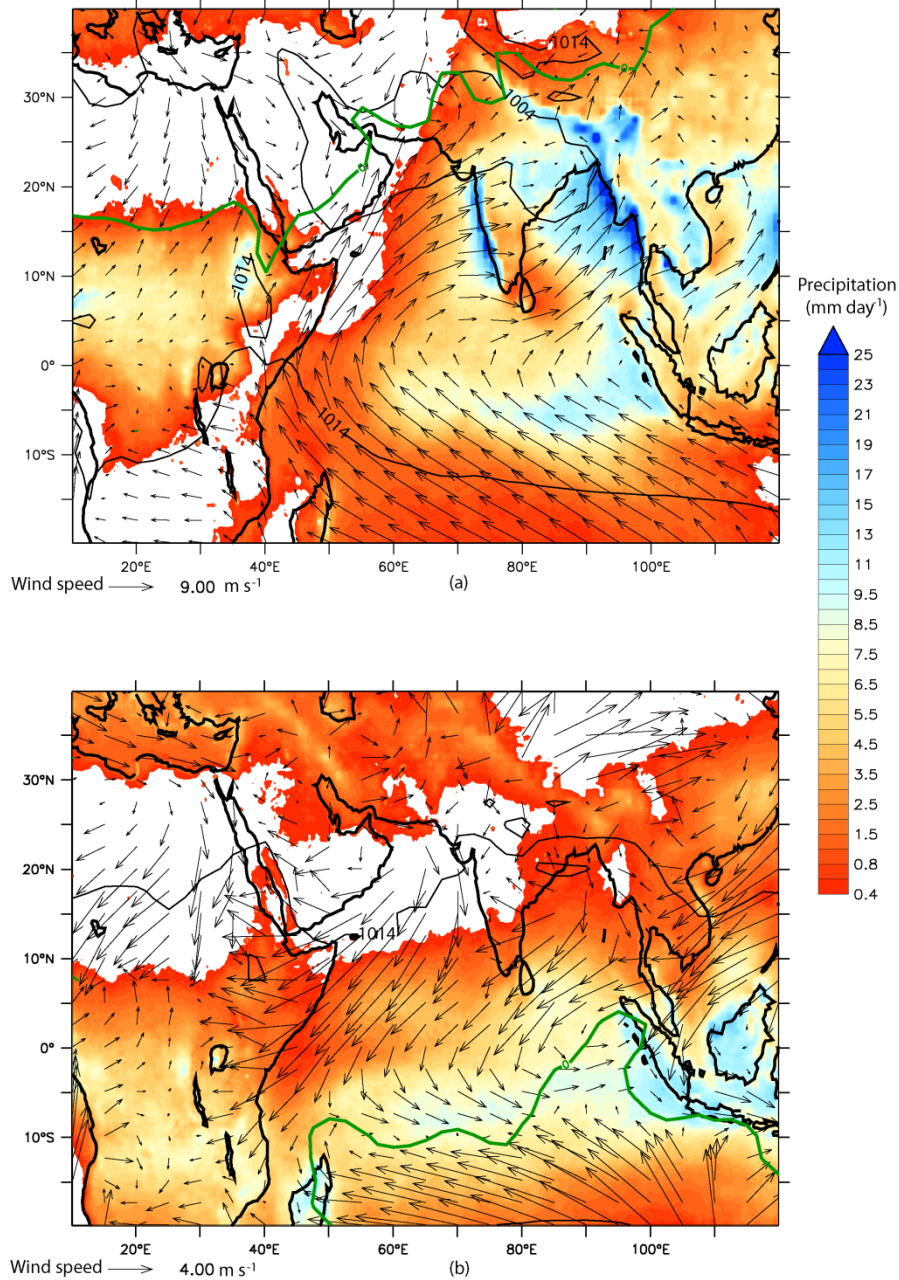


**Figure 2.1** Climatology (1997-2013) of the seasonal cycle of monsoon wind system over the northern Indian Ocean for (a) southwest monsoon and (b) northeast monsoon. The shading shows precipitation and the arrows represent the wind vectors. The black contours are the sea level pressure shown only for 1014 and 1004 mb pressure levels. The thick green line represents the mean position of the intertropical convergence zone taken to be the location where the meridional component of the wind becomes zero. The climatology of precipitation has been constructed from the Tropical Rainfall Measuring Missions data, while those for wind and pressure are from National Centers for Environmental Prediction/ National Center for Atmospheric Research (NCEP/NCAR) reanalysis.

The winds converge with the moist southwesterly winds at the ITCZ and override the monsoon system forming an inclined plane from west (near the surface) to east (higher up from the surface). In the vertical, the SWM system extends to about 700 mb pressure level. Above the monsoon system, the dry and warm airmass originating from the Middle East and southwest Asia blankets the sky.

### **2.1.2. The northeast monsoon**

The NEM season is much tranquil in comparison to the SWM. The low pressure centre over the land is replaced by the high pressure (exceeding 1020 mb) due to the cooling of the landmass (see Figure 2.1b). The ITCZ has shifted its position to about 10°S. Cold and dry northerly wind blows out from the Indian Subcontinent with an average speed of about 4 m s<sup>-1</sup>. The magnitude of wind stress is less than 0.1 N m<sup>-2</sup> over most of the AS with negative wind stress curl prevailing over the central AS. This time of the year is characterized by stable conditions due to subsidence of airmass. The main high pressure centre is over the Indo-Iranian region. Often western disturbances originating from the Mediterranean region travels eastward as low pressure systems. These are cold fronts that bring precipitation to the Middle East and central Asia and snowfall in northern India. In contrast to the Indian Subcontinent, most of the Middle East and southwest Asia receives winter rainfall, although the amount is very less (~ 5mm day<sup>-1</sup>). More than 60% of the rainfall is concentrated during the winter months of December to March peaking during January (total winter rainfall ~30mm).

## 2.2. Bio-physical coupling in the Arabian Sea

The influence of the monsoon wind is reflected in the seasonally reversing surface current systems in the AS. During the SWM time the direction of the monsoonal gyre is clockwise and during NEM, the circulation is anticlockwise [Schott and McCreary, 2001].

### 2.2.1. The southwest monsoon

During the SWM, the Somali Current flows northward along the coast off Somalia. This is one of the strongest western boundary currents having a maximum speed of  $3.5 \text{ m s}^{-1}$  during June [Tomczak and Godfrey, 1994]. Around  $4^{\circ}\text{N}$  latitude, the alongshore component of wind stress gives rise to the Somali upwelling. This moves surface water offshore and brings up nutrient rich cold subsurface water [Ryther *et al.*, 1966] from a depth of about 200m. This is marked by a reduction in the SST to less than  $25^{\circ}\text{C}$  during the peak of the upwelling season (see Figure 2.2a). Ekman pumping vertical velocity as high as  $1\text{-}2 \text{ m day}^{-1}$  is seen in the upwelling region [Vecchi *et al.*, 2004]. To the northeast of this intense upwelling region gyres and eddies are formed due to the breakdown of the mean flow. Two most important are the Great Whirl and the Socotra Eddy [McCreary and Kundu, 1988; Fischer *et al.*, 1996]. A second region of intense upwelling is off the coast of Oman also characterised by low SST and high primary productivity. The Ras al Hadd Jet having a maximum speed of about  $1 \text{ m s}^{-1}$  flows towards the northeast. To the north of the Findlater Jet, the positive wind stress curl gives rise to open ocean upwelling, while to the south the negative wind stress curl is responsible for mixed layer deepening [Prasanna Kumar *et al.*, 2001]. The region lying to the west of the Findlater Jet is characterized by the presence of numerous eddies and filaments. This region is one of the most productive regions of the world oceans during this time of the year having primary productivity of about  $135 \text{ mmol C m}^{-2} \text{ day}^{-1}$

[Barber *et al.*, 2001]. This is associated with organic carbon flux of  $45\text{-}55 \text{ mg m}^{-2} \text{ day}^{-1}$  dominated by opal suggesting the importance of diatoms [Honjo *et al.*, 1999].

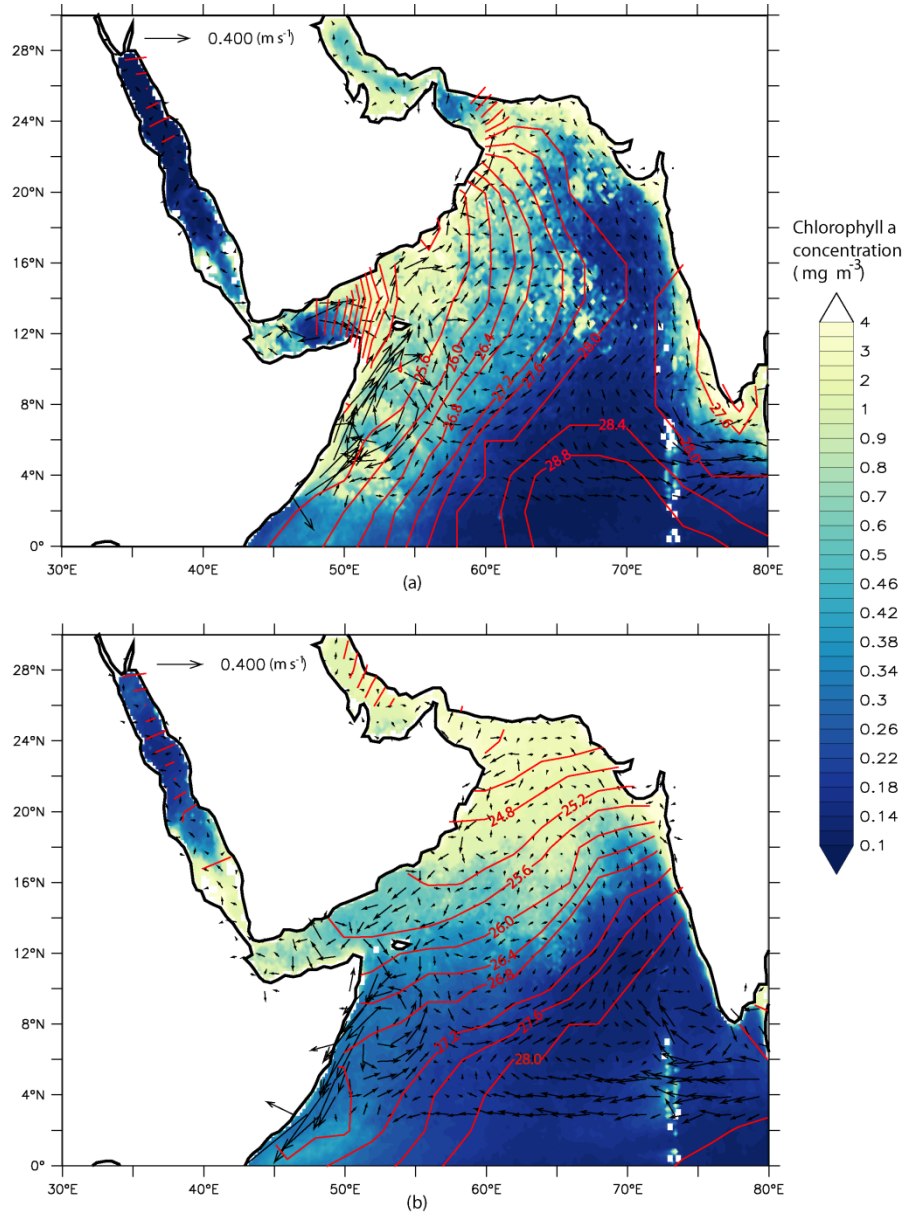


**Figure 2.2** Climatological (2003-2013) distribution of chlorophyll *a* concentration (shading), surface currents (vector) and sea surface temperature (red contours) over the Arabian Sea during (a) southwest monsoon and (b) northeast monsoon. Chlorophyll *a* concentration data is from Moderate Resolution Imaging Spectroradiometer (MODIS) onboard Aqua satellite, current vector is from Ocean Surface Current Analyses-Real time (OSCAR) and sea surface temperature is from Extended Reconstructed Sea Surface Temperature (ERSST).

There is a third upwelling developed along the southwest coast off India due to the change in sign of the wind stress curl [*Banse, 1959; Darbyshire, 1967*]. However, this upwelling is not as vigorous as the upwelling along the western AS.

### **2.2.2. The northeast monsoon**

During the NEM period, the West India Coastal current (WICC) flows northward along the west coast of India [*Shetye et al., 1991; Shetye et al., 2008*]. The current along the Somali coast also changes its direction and flow southward to join the East African Coastal Current. This time of the year the cold dry wind blowing out from landmass coupled with low insolation leads to high evaporation, which can exceed  $15 \text{ cm month}^{-1}$ . This leads to cooling of the surface water, increase in salinity, sinking of surface water, deepening of the mixed layer and formation of water masses. The Arabian Sea High Salinity Water (ASHSW) mass is formed during winter and spreads along the sigma-theta surface of 24 [*Prasanna Kumar and Prasad., 1999*] between 0-150m depths. Persian Gulf Water (PGW) is present between 250-300m, with core sigma-theta of 26.6. It forms in the Persian Gulf and spills through the Strait of Hormuz into the AS at a depth of 25-70m [*Prasad et al., 2001*]. Red Sea Water (RSW) lies between 600-700m depth ranges, with core sigma-theta of 27.2. After crossing the Strait of Bab el Mandeb, the water enters the Gulf of Aden. The northernmost limit of RSW is  $18^{\circ}\text{N}$  latitude [*Shetye et al., 1994*]. The mixed layer deepening associated with the NEM, entrains nutrients from the subsurface layer and leads to an increase in phytoplankton biomass [*Madhupratap et al., 1996; Prasanna Kumar et al., 2001*] (see Figure 2.2b). However, this time, the phytoplankton biomass is not as high as during the SWM. One reason for this is that a deep mixed layer leads to light limitation. The primary productivity during NEM is about  $88 \text{ mmol C m}^{-2} \text{ day}^{-1}$  [*Barber et al., 2001*].

The high productivity and the presence of land to the north have resulted in poor ventilation in the AS. This has given rise to the most intense oxygen minimum zone with oxygen concentration of less than 20  $\mu\text{M}$  in the depth range of 100-1000 m [Naqvi *et al.*, 2006]. This is a zone of intense denitrification and is an important source of the greenhouse gas nitrous oxide to the atmosphere [Naqvi *et al.*, 2000]. Thus, a change in productivity of this region has serious implications for the climate.

### **2.3. Dust source regions**

The main dust sources around the AS are the arid and the semi-arid regions of northeast Africa, the eastern Horn of Africa (Somalia), the Arabian Peninsula, the Tigris-Euphrates Basin, coastal Iran, the border between Iran-Pakistan-Afghanistan and the Thar Desert lying in Indo-Pakistan border [Prospero *et al.*, 2002; Leon and Legrand, 2003] (see Figure 2.3). In general, these dust sources are closely associated with water bodies (example lakes, rivers) that can produce and transport fine sediments for the wind to pick up when the water bodies get dried up [Prospero *et al.*, 2002]. These dust sources are active year-round, but the peak in dust activity is attained during the boreal summer. This is due to the high heat leading to atmospheric instability and convective activity. Average annual rainfall in the dust activity regions is limited to less than 200 mm. The regions that lie to the east and south of the ITCZ, receive rainfall during summer under the influence of SWM winds. Somalia experiences double peaks in rainfall: during spring and fall. The regions that lie to the west and north of the ITCZ experience winter rainfall due to the transit of low pressure systems from the Mediterranean region.

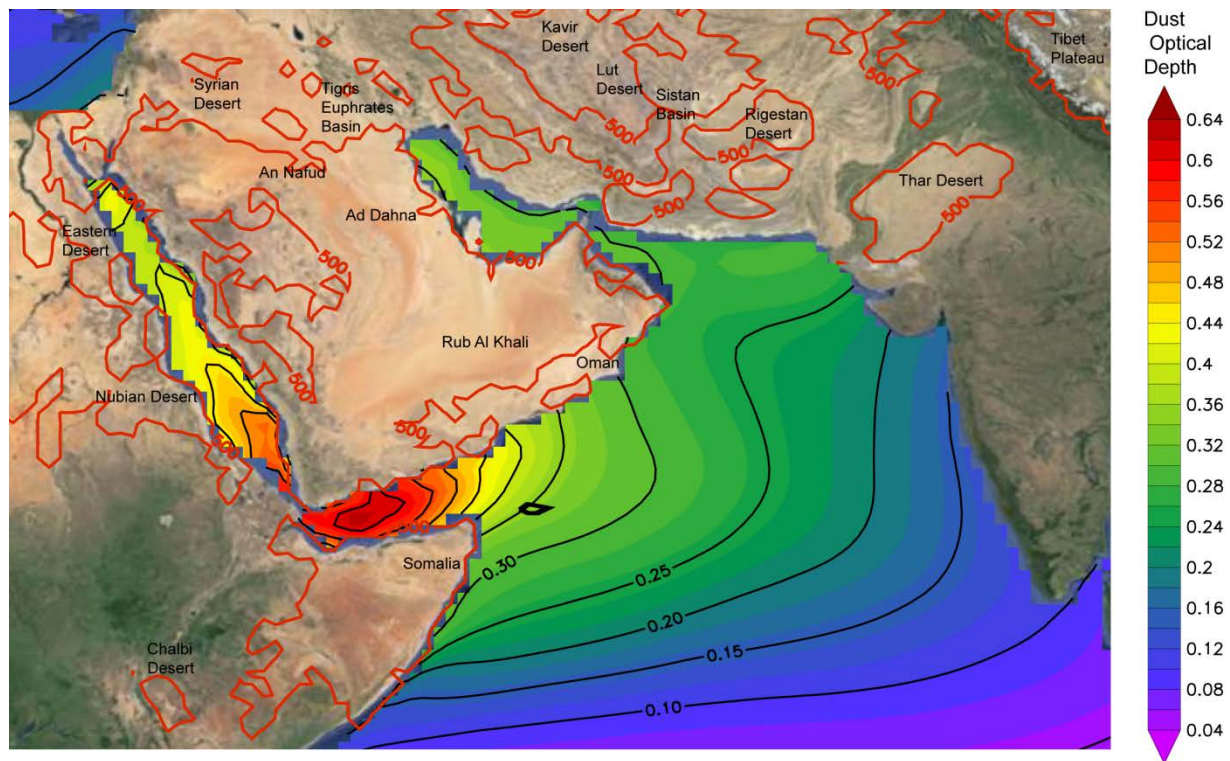


**Figure 2.3** Map showing climatological (2001-2010) distribution of dust optical depth over the Arabian Sea along with the locations of the surrounding dust source regions. The shading (and the overlaid black contours) shows the dust optical depth generated using a regional climate model as described in Section 3.1. The red contours overlaid on Google Earth image indicate the regions where the modeled annual dust emission exceeds  $500 \text{ mg m}^{-2} \text{ day}^{-1}$ .

The region lying in the Indo-Pakistan border is built up of fine alluvial sediments brought down by the mighty Ganges and the Indus river system. The loess deposits in the Thar Desert itself are associated with glacio-fluvial deposits during the Pleistocene [Tripathi and Rajamani, 1999]. As a whole, dust activity over the Indian subcontinent begins during March-April, peaks during the month of May and continues till July when the SWM rain establishes [example Middleton, 1986; Littman, 1991; Deepshikha et al., 2006]. The local name for dust generating wind is *Loo* (formed due to pressure gradient) and *Andhi* (formed due to convective downdrafts) [Middleton, 1986]. The Sistan Basin is the main region of dust activity lying in the border between Iran-Pakistan-

Afghanistan. The region is characterised by presence of ephemeral lakes due to the discharge of Helmand River. Dust is picked up between June and September under the influence of topographically steered northerly *Levar* wind (wind of 120-days) [Kaskaoutis et al., 2014].

Dust over Oman region is associated with the SWM circulation peaking during July [Ackerman and Cox, 1989]. The main dust activity regions are the alluvial deposits at the foot of the Hajar Mountains in northeast Oman, the Wahiba Sand Sea and the coastal lowlands. This region is one of the most important sources of dust to the AS [Pease et al., 1998]. Over the Arabian Peninsula, Tigris-Euphrates Basin and the coastal Iran region, dust activity begins during April-May and peaks in July [Prospero et al., 2002]. The dust activities in these regions are mainly associated with the northwesterly winds locally known as *Shamals* [Perrone, 1979; Rao et al., 2003; Vishkaee et al., 2012]. *Shamal* winds blow along the axis of the Persian Gulf (see Figure 2.4). They are associated with the deepening of the Indo-Iranian trough during summer and the eastward migration of the Mediterranean cold fronts during winter. The most active area is along the southern coast of the Persian Gulf associated with the presence of coastal calcareous sediments. Often, walls of dust, known as *Haboobs*, are seen to occur from the leading edge of convective downdrafts [Miller et al., 2008]. These *Haboobs* can be generated as mesoscale events, however, may often expand over time to synoptic scales [Miller et al., 2008]. To the southeast, the region of dust activity opens into the Rub Al Khali Desert. The region is bounded to the west by Ad Dahna and to the northwest by An Nafud Desert. The main source of sediment in the Tigris-Euphrates basin is the river alluvium that has accumulated since the Babylonian times. There are significant signatures of human induced desertification in the Tigris-Euphrates and the coastal Iran region [Ginoux et al., 2012]. Often the *Sharav* cyclones from the

Mediterranean region can give rise to dusty weather in the northern part of the Arabian Peninsula during winter-spring [Kubilay *et al.*, 2000].

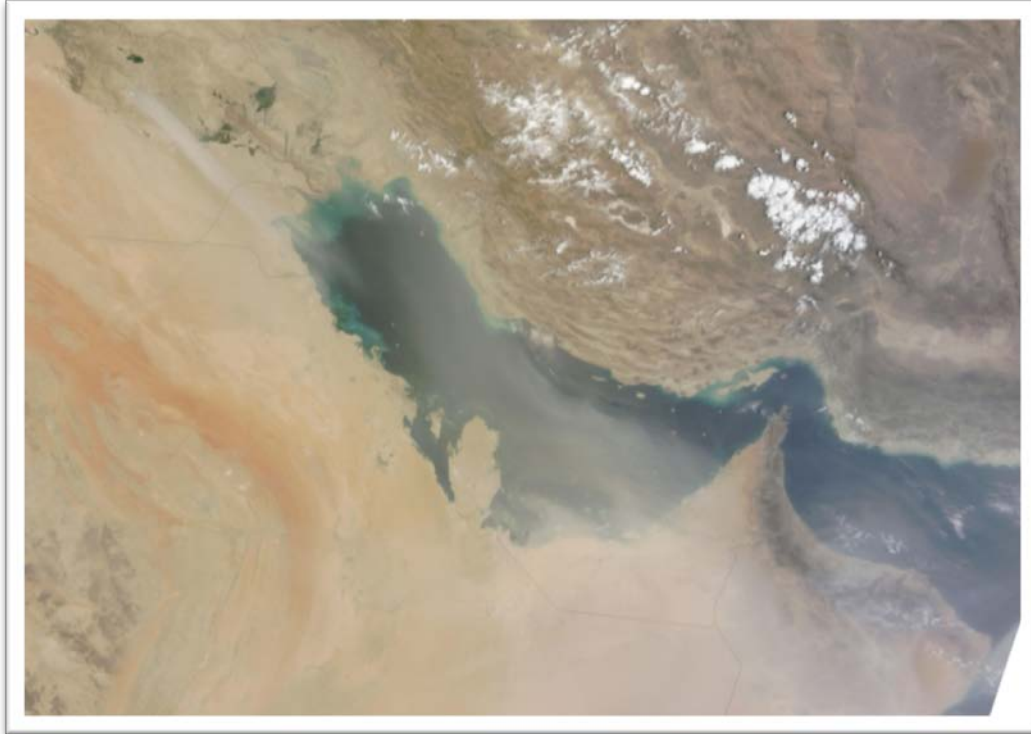


**Figure 2.4** An example of dust storm over the Persian Gulf due to the *Shamal* weather. This image has been captured by Moderate Resolution Imaging Spectroradiometer onboard Terra satellite on 01<sup>st</sup> July, 2011.

The Nubian Desert in Sudan is an active dust source, especially during spring. Dust from this region is often seen to move northward crossing the Red Sea. Dust activity in Somalia reaches maximum during July-August which correspond to the time of minimum rainfall. The main dust sources correspond to the numerous dry river channels that can produce abundant fine sediments during rainy periods [Leon and Legrand, 2003].

# CHAPTER 3

## DATA AND METHODS

### 3.1. Regional Climate Model

The dust cycle over the AS has been simulated using a regional climate model RegCM4. RegCM model was originally developed at National Centre for Atmospheric Research (NCAR) and later being constantly improved by Abdus Salam International Centre for Theoretical Physics. This type of regional climate model derives its forcing fields from a reanalysis product or a parent general circulation model (GCM) and dynamically downscales the fields into the model domain. Thus, the model can simulate climate processes for a selected study region at a resolution much finer than that can be attained in a GCM. This improves the forecasting skills and the representation of processes at a regional scale (see Figure 3.1 for example).

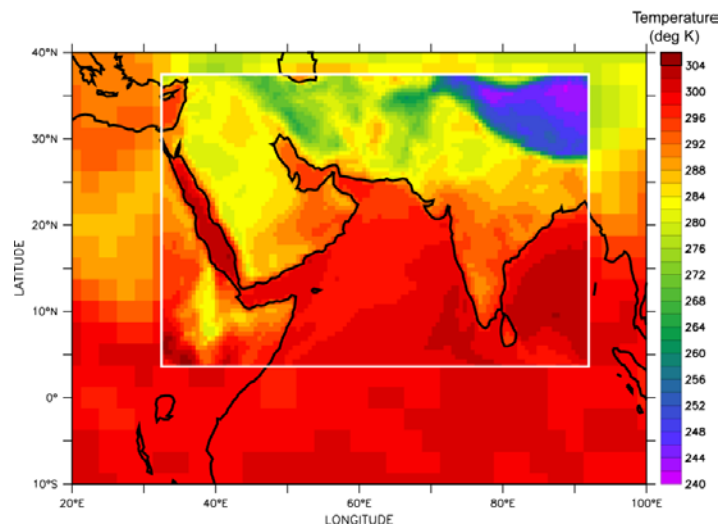


**Figure 3.1** Figure illustrating the difference in resolution between the driving reanalysis fields and the regional climate model. The finer resolution grid of RegCM4 is superimposed on the coarse resolution NCEP/NCAR reanalysis used to force the model.

RegCM4 is a hydrostatic, sigma vertical terrain-following model with Arakawa B-grid horizontal grid system (see Figure 3.2).

Sigma coordinate is defined as:  $\sigma = (p-p_t) / (p_s-p_t)$ ..... (i)

Where,  $p$ = pressure at a particular level,  $p_s$ = surface pressure and  $p_t$ = pressure at model top.

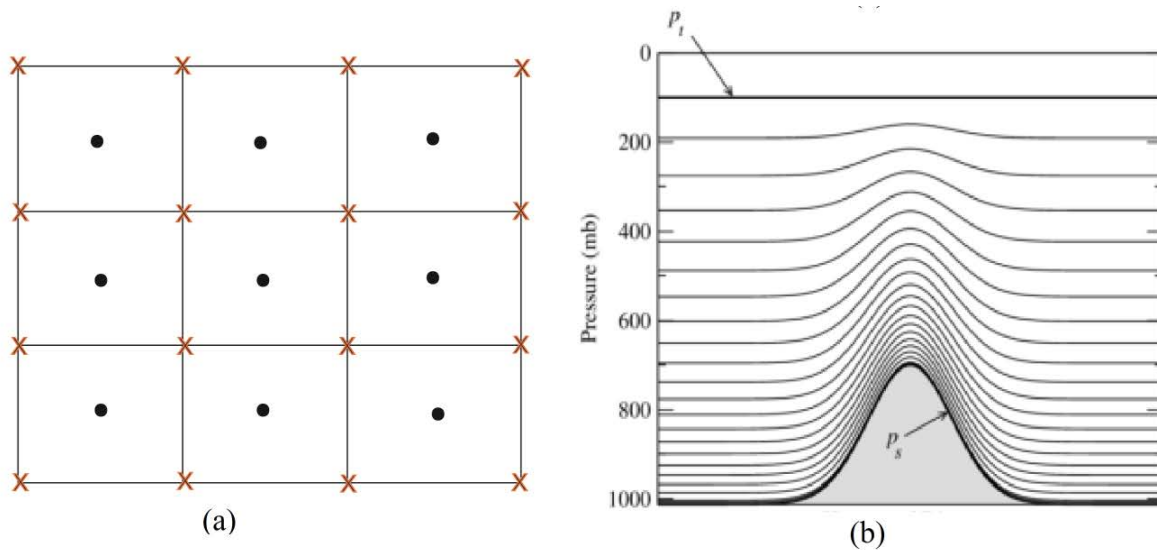


**Figure 3.2** Horizontal (a) and vertical (b) grids used in RegCM4. (a) A representation of Arakawa B grid used in RegCM4 Model. The scalar quantities are calculated at the centre of the grid and the vector variables are calculated at the corners (b) Sigma pressure system used in RegCM4 Model (source: <http://aaron.boone.free.fr/aspdoc/node7.html>). The pressure levels follow the outline of the local terrain at lower levels, but tend to flatten out at higher levels.

In case of Arakawa B-grid, the scalar variables are located at the centre of the grid box, while the velocity variables are located at the corners. The model dynamics has been described by *Grell et al.* [1994] and involves solving the momentum, continuity, thermodynamic and hydrostatic equations. Terrain, landcover and SST are given as lateral and boundary conditions; while time-varying temperature, geopotential height, relative humidity, U and V components of the wind are given as forcing. For running RegCM4 with dust, the distribution of soil texture has to be provided as well.

Land surface processes are modeled using Biosphere-Atmosphere Transfer Scheme (BATS) [Dickinson *et al.*, 1993]. BATS is used to calculate surface-atmosphere exchanges of momentum, energy and water vapour using a vegetation layer, a snow layer and soil layers (surface layer, root zone and a deeper layer). It uses 20 landcover types, 12 soil texture types and 8 soil colour types. First, the landcover and soil types are assigned for each model grid. Next, the drag coefficient for a particular surface is calculated. In case of vegetated surface transpiration, evaporation, dew formation and leaf temperature are determined. For a particular soil, temperature, soil moisture, soil water evaporation, runoff and snow covers are estimated. This information is used to calculate sensible and latent heat fluxes to the atmosphere for a particular landcover type.

The dust module included within RegCM4 has been described by Zakey *et al.* [2006]. It includes emission, transport and depositions of dust particles and calculation of dust optical properties. The BATS interface is used to calculate dust emissions. The main steps involved in the implementation of the dust module are given as follows:

- (1) Calculation of dust emission by wind erosion. This involves specification of soil size distribution for each grid based on United States Department of Agriculture (USDA) soil textural classifications and determination of soil mass-mean diameter for these textural types. Next, the (size-dependent) threshold friction velocity is calculated for each soil type. Horizontal mass flux of soil aggregates by saltation take place if the friction velocity exceeds the threshold. Finally, vertical mass flux of dust is dependent on the diameter, density and the kinetic energy (dependent on horizontal mass flux) of the soil

aggregates. Based on the BATS land type information, dust can only be emitted from a desert and semi-desert region which is shown in. Figure 3.3.

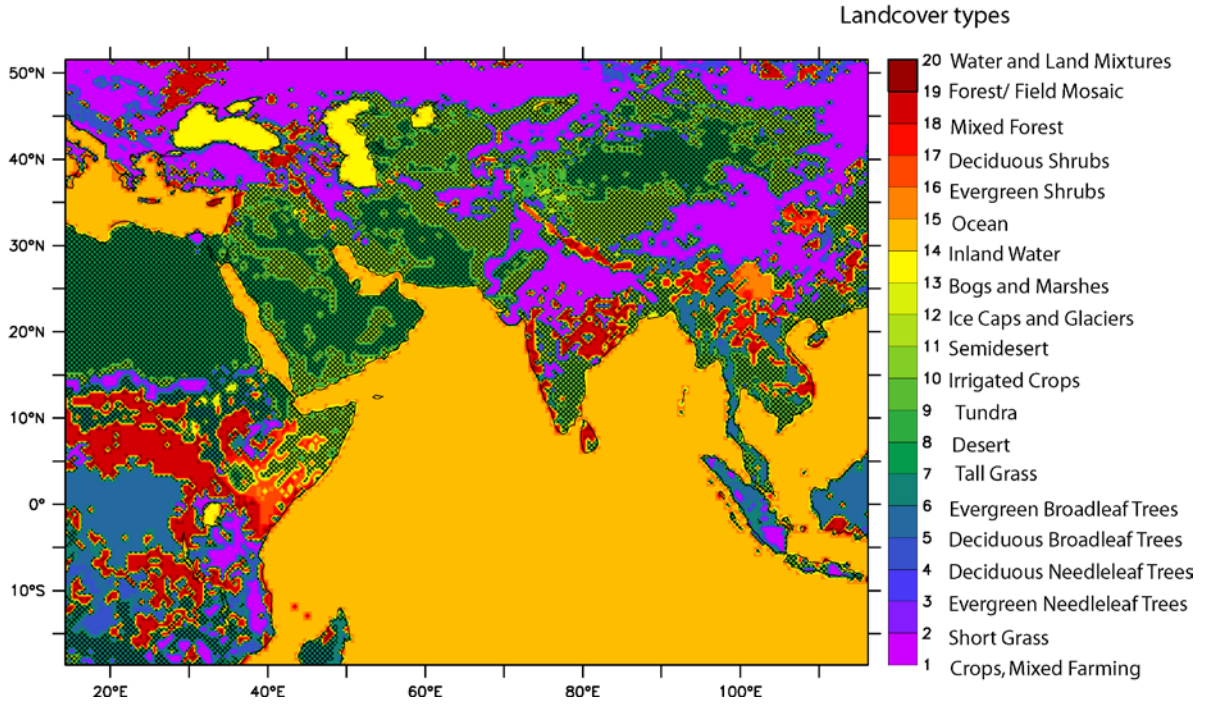


**Figure 3.3** Distribution of different categories of landcover within the model domain. The landcover categories are obtained from Global Land Cover Characteristics (GLCC) - Biosphere Atmosphere Transfer Scheme (BATS). The black stippling mark the landcover classified as “Desert” and “Semi-desert” from where dust emission takes place.

(2) Dust transport takes place in 4 size bins: 0.01-1  $\mu\text{m}$ , 1-2.5  $\mu\text{m}$ , 2.5-5  $\mu\text{m}$ , 5-20  $\mu\text{m}$ . Dust transport is based on the tracer transport equation of *Solomon et al.* [2006] which for each tracer  $i$  is given as follows:

$$\frac{\partial \chi}{\partial t} = -\mathbf{V} \cdot \nabla \chi^i + F_D^i + T_C^i + S^i - R_{WIS}^i - R_{WC}^i - D_d^i + \sum (Q_p^i - Q_i^i) \dots \dots \text{(ii)}$$

where,  $S^i$  is the emission term,  $-\mathbf{V} \cdot \nabla \chi^i$  is the advection term,  $F_D^i$  is the diffusion term (horizontal + vertical),  $T_C^i$  is the convective transport term,  $R_{WIS}^i$  and  $R_{WC}^i$  are terms

describing wet removal by large-scale and convective rain respectively,  $D_{\text{a}}^{\text{i}}$  refers to dry deposition,  $Q_{\text{p}}^{\text{i}}$  and  $Q_{\text{t}}^{\text{i}}$  are the production and loss of a tracer due to the chemical transformations.

(3) Dry deposition of dust is based on particle size and density and takes into account the contributions of turbulent transfer, Brownian diffusion, impaction, interception, gravitational settling and particle rebound [Zhang *et al.*, 2001]. So far as wet deposition is concerned, fraction of dust contained in the cloud water that can be precipitated has been specified with smaller size dust particles more likely to form cloud condensation nuclei than the larger size dust particles.

(4) Aerosol Optical Depth ( $\tau$ ) is calculated for each size bin based on Kiehl *et al.* [1996] using Mie theory. Model output of  $\tau$  is at 500 nm wavelength.

Figure 3.4 schematically represents the main features involved in the dust module incorporated within RegCM4 model.

For the present study, dust cycle has been simulated using RegCM4 for the period of 2001-2010. In the present configuration, dust has been allowed to dynamically and thermodynamically interact with the model forcing fields. For each year, simulation has begun from 01-November of the previous year to 31-December of the year being simulated. For example, for the year 2001, dust cycle has been simulated for 01-November, 2000 to 31-December, 2001, allowing the first month as a spin-up time. The outputs of the model have been compared extensively with satellite-derived dust optical depth (described in Section 3.3 and Chapter 4) and with *in situ* AERONET aerosol optical depth (see Chapter 4). The main model configuration is provided in Table 3.1.

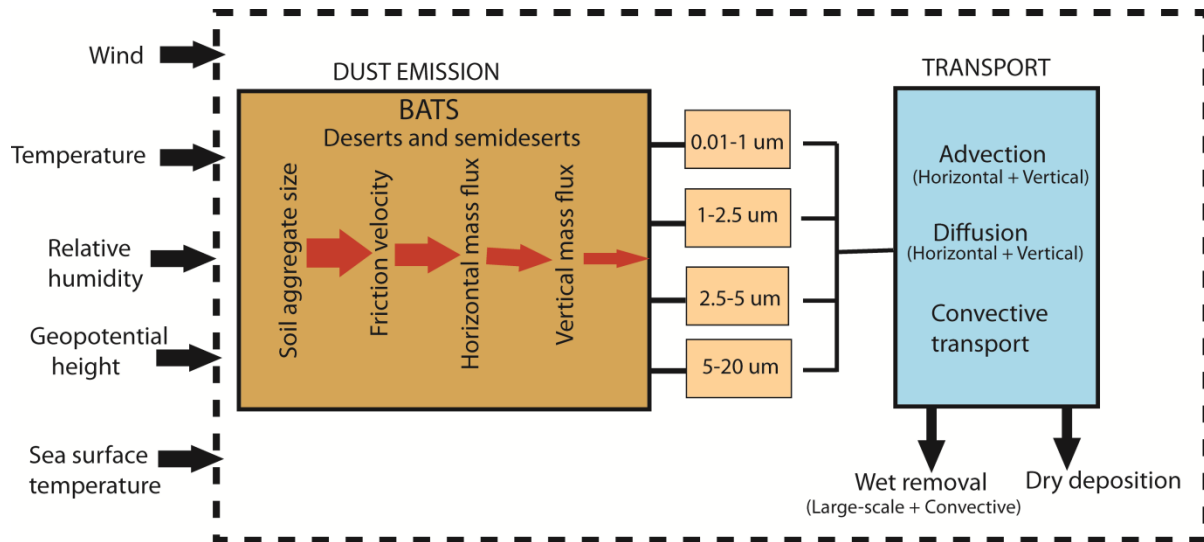


**Figure 3.4** Schematic representation of the working of the dust module in RegCM4 model.

**Table 3.1** Configurations used for simulating dust cycle using RegCM4 Model

<b>Domain</b>	14 -116°E longitude and 19°S – 52°N latitude
<b>Period of Simulation</b>	01 November 2000 to 31 December 2010
<b>Spatial Resolution</b>	60 kilometres
<b>Map Projection</b>	Normal Mercator
<b>Vertical levels</b>	23 vertical levels from 1008 to 50 mb
<b>Atmospheric forcing</b>	6-hourly data from NCEP/NCAR reanalysis
<b>Sea surface temperature</b>	weekly Optimally Interpolated SST
<b>Surface Terrain</b>	GTOPO30
<b>Soil texture</b>	Zobler's assessment of FAO Soil Unit [Zobler, 1986]
<b>Landcover categories</b>	Global Land Cover Characteristics- Biosphere Atmosphere Transfer Scheme (GLCC-BATS)
<b>Large-scale Precipitation Scheme</b>	Subgrid Explicit Moisture Scheme (SUBEX) [Pal et al., 2000]
<b>Convection Scheme</b>	Grell Scheme [Grell, 1993]

### 3.2. 1-D mixed layer depth model

The state of the water column in the study region has been assessed with the help of the mixed layer depth (MLD) data obtained by employing the Price-Weller-Pinkel (PWP) mixed layer

model [Price *et al.*, 1986]. PWP is a simple one-dimensional model in which scale analysis suggests that MLD is directly proportional to surface wind stress and inversely proportional to the square-root of surface heat fluxes. PWP is a bulk mixed layer model which assumes all properties are well mixed within the mixed layer. The calculation of the MLD is initialized from a temperature, salinity profile. First, momentum, freshwater and heat fluxes are applied at the surface which controls the degree of mixing. MLD is determined using a density criterion of  $0.0001 \text{ kg m}^{-3}$ . Mixed layer is deepened till all instabilities are removed. It uses a bulk Richardson number (critical value of 0.65) to check the mixed layer stability and uses gradient Richardson number (critical value of 0.25) below the mixed layer to check for shear flow instability. Since this is a one-dimensional model, any effect of advective processes is discounted here. Therefore, PWP model will fail to reproduce the MLD during those periods (example SWM) when strong currents prevail. This model has been primarily applied to simulate MLD for the central AS during NEM period. In this location during this time of the year advection is insignificant and momentum and heat fluxes are the prime drivers of MLD.

The model has been initialized with the climatological temperature and salinity profiles from World Ocean Atlas 2009 (WOA09) [Locarnini *et al.*, 2010; Antonov *et al.*, 2010] and forced by net longwave and shortwave radiation data from National Centers for Environmental Prediction/ National Center for Atmospheric Research (NCEP/NCAR) reanalysis [Kalnay *et al.*, 1996]. Turbulent heat fluxes are obtained from Objectively Analyzed air-sea Fluxes (OAFlux) [Yu and Weller, 2007]. Momentum fluxes are calculated from Quick Scatterometer (QuickSCAT) and Advanced Scatterometer (ASCAT) wind data. For freshwater fluxes (E-P), Evaporation (E) data are obtained from OAFlux and Precipitation (P) from Tropical Rainfall Measuring Mission (TRMM) (<http://disc.sci.gsfc.nasa.gov/precipitation/tovas/>). The daily climatology of the

simulated MLD has been compared with the MLD derived from *in situ* Argo data ([http://www.usgodae.org/cgi-bin/argo\\_select.pl](http://www.usgodae.org/cgi-bin/argo_select.pl)) using 0.5°C temperature difference criteria.

### **3.3. Remote sensing of dust**

#### **3.3.1. Derivation of dust optical depth from satellite**

Aerosol optical depth or  $\tau$  refers to the vertically integrated extinction (absorption + scattering) of light due to the presence of different types of aerosols in the atmosphere. More the amounts of aerosols present more is the value of  $\tau$ . The polar-orbiting Moderate Resolution Imaging Spectroradiometer (MODIS) onboard Aqua (since 4 May 2002) and Terra (since 18 December 1999) is a key instrument to derive value of  $\tau$  from space [Tanre *et al.*, 1997; Levy *et al.*, 2009]. Terra orbits the earth from north to south crossing the equator in the morning and the Aqua orbits the earth from south to north crossing the equator during the local noon time. Retrieval is done at 3 different spatial resolutions: 250 m, 500 m and 1 km. MODIS instrument uses 36 spectral bands ranging from 400 nm to 14.4  $\mu\text{m}$  wavelengths. Of these, 7 channels (weighted central wavelengths are: 466 nm, 553 nm, 646 nm, 855 nm, 1243 nm, 1632 nm and 2119 nm) are used to retrieve aerosols over the ocean. The retrieval of  $\tau$  by MODIS is based on look-up table which have pre-computed radiation values for a set of aerosol load and surface type [Levy *et al.*, 2009]. These values are compared with the observed radiances. There are separate algorithms for retrieving  $\tau$  over land [Kaufman *et al.*, 1997] and over oceans [Tanre *et al.*, 1997]. For the present study monthly mean Level 3 gridded ( $1^\circ \times 1^\circ$  spatial resolution)  $\tau$  over ocean from MODIS Collection 5.1 has been used at 550 nm wavelength.

The contribution of dust aerosols to the light extinction is referred to as dust optical depth. Dust optical depth ( $\tau_{\text{du}}$ ) has been calculated for the AS from MODIS onboard Aqua (period 2003-

2011) and Terra (period 2000-2011) using the method given by *Kaufman et al.* [2005]. Briefly, this is given as:

$$\tau_{du} = [\tau (f_{an} - f) - \tau_{ma} (f_{an} - f_{ma})] / (f_{an} - f_{du}) \dots\dots\dots (iii)$$

For this, monthly mean aerosol optical depth ( $\tau$ ) at 550 nm wavelength and fraction of  $\tau$  contributed by the fine aerosols ( $f$ ) have been obtained from MODIS Aqua and Terra.  $f_{an}$ ,  $f_{ma}$  and  $f_{du}$  are the fine mode fraction of anthropogenic, maritime and dust aerosols respectively.  $f_{an}$  has been taken as 0.90 based on MODIS measurements in the northern Bay of Bengal (88°-92°E, 19°-21°N) during NEM when anthropogenic fraction dominates the total aerosol load [*Nair et al.*, 2005]. The value of  $f_{ma}$  is taken as 0.47 based on average value for the period of 2003 to 2011 over the western part of the Equatorial IO (55°-65°E, 5°-10°S) where pristine maritime condition prevails. The standard deviations (SD) for values of  $f_{an}$  and  $f_{ma}$  were 0.15 and 0.08 respectively. A value of 0.25 has been assigned to  $f_{du}$  based on satellite values during dust outbreaks in the Middle East. The maritime aerosol optical depth ( $\tau_{ma}$ ) is obtained from the wind speed based equation given by *Smirnov et al.* [2003]:

$$\tau_{ma} = 0.007W (m s^{-1}) + 0.05 \dots\dots\dots (iv)$$

where,  $W$  is the wind speed ( $m s^{-1}$ ). Wind data at 10m above the sea surface from QuickSCAT has been used during the period 2000 to 2008 followed by ASCAT data (<http://cersat.ifremer.fr/data/products/catalogue/>) for the remaining years. *Kaufman et al.* [2005] have estimated an error of 10-15% in  $\tau_{du}$  for  $\tau_{du} > 0.1$ , while the error in  $\tau$  is  $\pm 0.01 \pm 0.05\tau$  [*Remer et al.*, 2002]. Assuming that the error in  $\tau_{du}$  arises due to the values assigned for  $f_{an}$ ,  $f_{du}$  and  $f_{ma}$ , 1000 simulations of  $\tau_{du}$  have been performed using Monte Carlo method [*Geyer*, 2011]. Using

this method the error has been estimated as 1.35%. Figure 3.5 shows the time-series of  $\tau_{du}$  over the AS along with  $\tau$ .

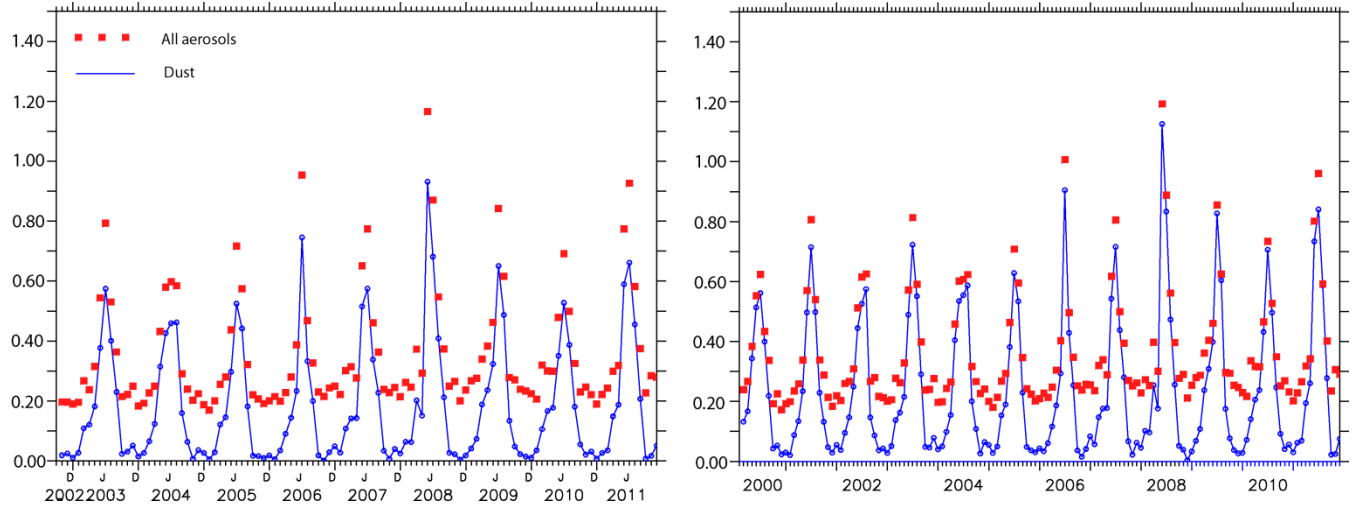


**Figure 3.5** Time-series of dust and aerosol optical depth over the Arabian Sea (50-78°E and 10-25°N) for (left) MODIS/Aqua and (right) MODIS/Terra.

### 3.3.2. Aerosol Index

The time-series of dust aerosols in the atmosphere over a region for climate studies is perhaps best represented by ultraviolet-absorbing Aerosol Index (AI) which, although discontinuous at times, has been giving a semi-quantitative indication of dust load over both land and ocean since the late 1970s. AI is an indicator of how much absorbing and non-absorbing spectral radiance ratios in an atmosphere with aerosols differs from that of a purely molecular atmosphere [Herman *et al.*, 1997]. AI uses radiance ratio at 340 and 380 nm wavelengths, that is, the near ultraviolet region. In this region, the surface reflectivity over both land and oceans are low. In a molecular atmosphere, due to the strong wavelength-dependence of scattering at the shorter wavelengths, there is large difference in radiances between 340 and 380 nm wavelength. The

presence of ultraviolet-absorbing aerosols like dust tends to reduce this difference and can therefore be easily detected [*Herman et al.*, 1997].

Daily AI data have been obtained from Total Ozone Mapping Spectrometer (TOMS) onboard Nimbus 7 satellite for the period of January, 1979 to December, 1990 and onboard Earth Probe (EP) satellite for the period January, 1997 to December, 2001 at a spatial resolution of  $1.00^{\circ} \times 1.25^{\circ}$ . Data from the Ozone Monitoring Instrument (OMI) onboard Aura satellite (equator passing time is local afternoon) were used for more recent period encompassing January, 2005 to December, 2013 at a spatial resolution of  $1.00^{\circ} \times 1.00^{\circ}$ . The data for the period 1991-1992 were not considered to avoid contamination of the dust signal by volcanic aerosols due to the eruption of Mount Pinatubo. No such contamination of the dust signal due to El Chichon eruption in 1982 was found and therefore the data for the 1982-1983 periods have been retained. Also, the data for the period 2002-2004 were discarded due to calibration problem with TOMS EP. The daily AI data for a total of 26 years were screened to enumerate the percentage of days each year when AI exceeded a threshold value of 1.5 (AI-1.5). This gave an indication of the percentage of days each year when there was significant amount of dust activity in the region. Taking other thresholds for AI like 1.0 or 2.0 has yielded more or less the same results with some increase and decrease respectively in the area extent of the main dust activity regions.

There are two major caveats while using AI data: (1) although dust is ultraviolet absorbing aerosol, black carbon can equally absorb in the ultraviolet region. Since the main regions of dust activity are arid in nature, the possibility of black carbon contaminating the dust signal is minimised. (2) The AI retrieval is highly dependent on the height of the dust aerosols with dust in the upper layer being more effectively detected than near the surface [*Herman and Celarier*, 1997]. There is a possibility that AI may actually represent dust that is being transported.

However, several studies have shown that over the dust source regions the frequency of days when AI attains high values are much greater than in other regions [example *Prospero et al.*, 2002; *Ginoux et al.*, 2012].

### **3.3.3. MODIS deep blue aerosol optical depth**

The MODIS deep blue aerosol optical depth employs the blue channel of the satellite instruments. At this wavelength, the surface reflectance is low, but the presence of dust creates spectral contrast [*Hsu et al.*, 2004, 2006]. This deep blue algorithm is mainly used for retrieving dust over bright land surface and unlike AI data it is not sensitive to height of the aerosol layer. MODIS/Aqua deep blue aerosol optical depth was used for the period 2003-2010 in order to compare with the  $\tau_{du}$  obtained from the regional climate model.

### **3.3.4. AERONET Data**

The Aerosol Robotic NETWORK (AERONET) is a globally distributed network dedicated towards monitoring the levels of aerosol over a location using ground-based Cimel sun photometers [*Holben et al.*, 1998]. AERONET makes direct sun measurements at 8 wavelengths: 340 nm, 380 nm, 440 nm, 500 nm, 675 nm, 870 nm, 940 nm and 1020 nm. Of these, 940 nm is used for retrieval of water vapour and the rest are use for retrieval of  $\tau$ . The accuracy of  $\tau$  varies between 0.01 for wavelengths greater than 440 nm and 0.02 at shorter wavelengths. Data from AERONET are obtained at three levels: Level 1.0 gives unscreened data, Level 1.5 gives cloud-screened data and Level 2.0 gives cloud-screened, quality assured data. For the present purpose, daily cloud-screened and quality-assured Level 2.0 data for  $\tau$  at 500 nm wavelength has been used from 8 selected stations spread out in different regions around the AS. The main aim of using AERONET data is to compare the model results over land.

### 3.4. Other Data

#### *Climate Indices data*

El Nino-Southern Oscillation (ENSO) was represented using Extended Reconstructed Sea Surface Temperature (ERSST) NINO3.4 index for October to December (OND) of each year for the period 1978 to 2013. NINO3.4 index uses SST in the region 5N-5°S and 170-120°W. A year was designated as an El Nino (warm) year when NINO3.4 index exceeded a value of 1.0. Years having NINO3.4 indexes less than -1.0 were taken as La Nina (cold) years. Those years when NINO3.4 index was in between -1 and 1.0 were regarded as normal years. Dipole Mode Index (DMI) representing the phase and amplitude of Indian Ocean Dipole (IOD), averaged over September to November (SON), was determined using ERSST data by calculating the difference in SST anomaly between western tropical IO (10°S-10°N and 50°E-70°E) and eastern tropical IO (5°S-10°S and 90°E-110°E). The region chosen for this calculation is much similar to the boxes used by *Saji et al.* [1999] and *Meyers et al.* [2007] for defining IOD. A year was regarded as a positive (negative) IOD when the DMI index was above 0.5 (below -0.5). A normal year was regarded as one which had DMI index between -0.5 and 0.5.

#### *Chlorophyll concentration and Fluorescence Line Height data*

Chl *a* pigment concentration has been used as a proxy to phytoplankton biomass. Daily MODIS/Aqua Standard Mapped Image Chl *a* concentration data at 4 kilometer resolution have been obtained for the period October 2002 to 2011. Chl *a* retrieval by MODIS/Aqua is achieved by exploiting the remote sensing reflectance at blue and green spectral region. Under open ocean conditions, Chl *a* concentrations is proportional to the ratio of the remote sensing reflectance at blue and green wavelengths. The algorithm that is used to retrieve Chl *a* measurements is Ocean

Chlorophyll three-band Algorithm for MODIS (OC3M) [O'Reilly *et al.*, 2000] which uses remote-sensing reflectance ( $R_{rs}$ ) at 443 nm, 488 nm and 551 nm wavelengths. OC3M is an empirical algorithm in which Chl *a* concentration is determined as:

$$\text{Log}_{10}(\text{Chl}) = 0.283 - 2.753R + 1.457 R^2 + 0.659 R^3 - 1.403R^4 \dots\dots\dots (v)$$

$$\text{Where, } R = \log_{10} [\max (R_{rs443}), (R_{rs488}) / (R_{rs551})] \dots\dots\dots (vi)$$

It often happens that dust particles suspended in the water gives a false impression of increased Chl *a* concentrations and can lead to a spurious correlation between dust and Chl *a* [Claustre *et al.*, 2002]. To confirm that any Chl *a* response following a dust storm is not a remote sensing artefact, MODIS/Aqua Fluorescence Line Height (FLH) data have also been used. FLH is defined as the departure of the signal at 678 nm wavelength from the baseline that joins 667 nm and 748 nm wavebands. FLH has been used because only phytoplankton fluoresces in the ocean at 678 nm wavelength sensed by MODIS and hence can be effectively used as a proxy for biological activity [Hu *et al.*, 2005; Lin *et al.*, 2011].

***Supporting data***

Climate Prediction Center modeled monthly soil moisture data were used at spatial resolution of 0.5°x0.5° for the period 1978 to 2013. Soil moisture is calculated by means of a one-layer water balance model using observed monthly precipitation over land and temperature [Fan and Dool, 2004]. Monthly precipitation data over land were obtained from Global Precipitation Climatology Centre at spatial resolution of 0.5°x0.5° for the period 1978 to 2010 [Schneider *et al.*, 2013]. Additionally, daily rainfall data from TRMM 3B42 version 7 has also been used for the period 1997 to 2013 to explore the rainfall characteristics of the study region and also to compare with RegCM4 simulations. 3B42 data uses microwave data from TRMM as well as

multiple satellites like SSMI, SSMIS, MHS, AMSU-B and AMSR-E (see page xxi for full forms) and is available at  $0.25^\circ \times 0.25^\circ$  spatial resolution. Data for wind vectors, specific humidity, geopotential height and vertical velocity were obtained from NCEP/NCAR reanalysis [Kalnay *et al.*, 1996] and outgoing longwave radiation (OLR) from NOAA [Liebmann and Smith, 1996]. Nitrate data from WOA09 as well as JGOFS have been used to study the impact of dust on Chl *a* concentrations.

## CHAPTER 4

# VALIDATION OF REGIONAL CLIMATE MODEL OVER THE ARABIAN SEA

### 4.1. Approach

The strategy for model validation primarily relies on comparing the  $\tau_{du}$  generated by the model with the  $\tau_{du}$  derived from MODIS/Terra and Aqua observations using the method by *Kaufman et al.* [2005] as described in Section 3.3. MODIS retrieves  $\tau_{du}$  at 550 nm wavelength, while  $\tau_{du}$  from RegCM4 is at 500 nm wavelength. In a simple term,  $\tau_{du}$  is an indicator of the concentration of dust suspended in the atmosphere. As such, it is the net result of soil dust mobilization from disturbed surface and losses due to deposition. Therefore, implicit in this comparison is the assumption that, if the model can simulate  $\tau_{du}$  correctly, it can simulate emission and deposition processes correctly. While, this assumption can work when dust is transported in the lower layers of the atmosphere and dry deposition is the main mode of deposition, the same can fail, if dust travels at a higher level in the atmosphere with predominance of wet deposition. However, since direct estimates of dust emission and deposition are difficult to obtain,  $\tau_{du}$  has been used for comparing the model with the observation. Moreover, since satellite observed  $\tau_{du}$  provide information over large area and over different temporal resolutions, it is well suited for understanding the robustness of the simulated  $\tau_{du}$ . Along with MODIS  $\tau_{du}$ , AI data from OMI/Aura, MODIS/Aqua deep blue  $\tau$  and  $\tau$  derived from AERONET have also been used. Each of these products has been retrieved at different time of the day (no night time retrieval) and uses

different wavelength bands and assumptions regarding the presence of dust in the atmosphere (refer to Section 3.3). Thus, none of these products are directly comparable, but each of them reveals different information regarding the distribution of dust over the AS. RegCM4 simulations, on the other hand, gives dust concentrations at 6 hourly intervals that have been averaged out to give the output. So, RegCM4 simulations contain information about dust both during day and night. Also, it is important to note that different satellite and AERONET stations cover different time periods. This temporal coverage is indicated in Figure 4.1.

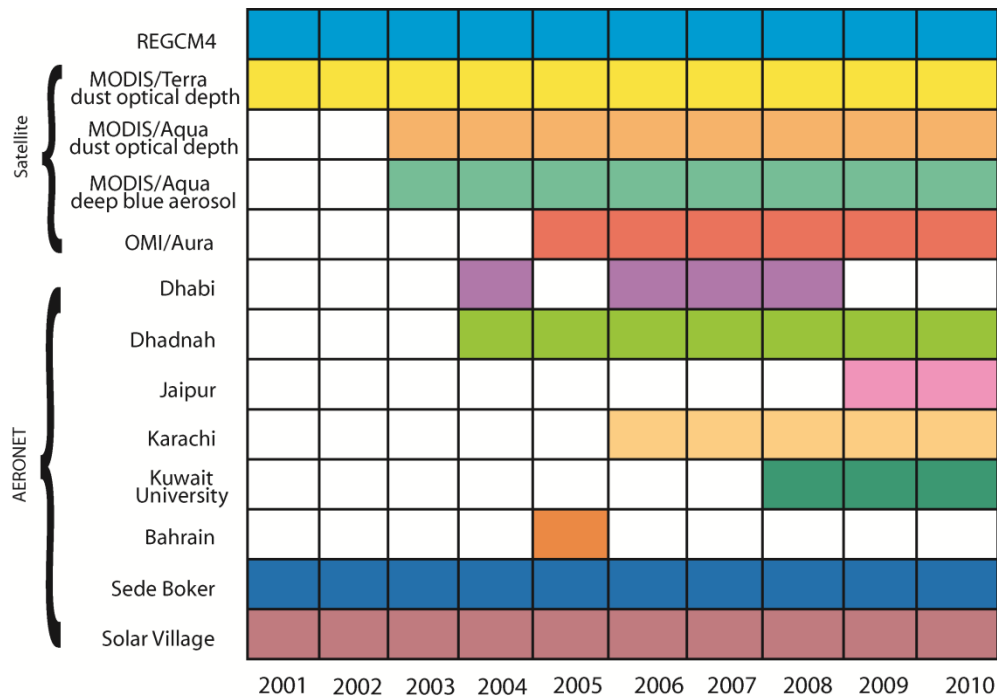


**Figure 4.1** Temporal coverage of different data that have been used to evaluate dust optical depth derived from RegCM4 model.

While trying to validate the model, first the spatial distribution of modeled  $\tau_{du}$  is compared with satellite observations both over ocean and land. Next,  $\tau_{du}$  is compared with  $\tau$  derived from different AERONET stations over land. The temporal evolution of  $\tau_{du}$  is studied for different regions over the AS. It is seen that maximum discrepancy between the model and the

observations is during the SWM. Hence, an attempt is made to unravel what might give rise to this discrepancy by comparing the model forcing fields (wind, temperature, humidity) with the model output.

## 4.2. Comparison with satellite observations

The distribution of annual  $\tau_{du}$  as simulated by RegCM4 model for the entire period of 2001-2010 is shown in Figure 4.2a. Highest  $\tau_{du}$  is seen near the dust sources lying to the west and northwest of the AS.  $\tau_{du}$  decreases steadily towards the east and southeast. When, the different satellite products are taken into account, however, it is seen that there are several lines of disagreements between the different products. These probably arise from: (1) difference in dust retrieval methods and (2) the time when the satellite passes over the region. For example, comparing  $\tau_{du}$  from MODIS/Terra (morning time overpass) with MODIS/Aqua (noon time overpass), it is seen that  $\tau_{du}$  values are more in Terra. This reflects the importance of diurnal cycle of dust emission and transportation. In case of Saharan dust sources, such temporal differences in satellite overpass have proved to be a crucial factor in determining the levels of dust over a region [Laurent *et al.*, 2010; Schepanski *et al.*, 2012]. It has been estimated that diurnal variability of dust mobilization and surface concentrations contribute about 67% and 33% respectively to the annual variances in these parameters [Luo *et al.*, 2004]. If the simulated  $\tau_{du}$  is compared with that derived from MODIS/Terra and Aqua (Figure 4.2b and c respectively), an overall similar pattern of high  $\tau_{du}$  near the principal dust sources and low values away from the dust sources is obtained. Although, there is an agreement in the overall pattern of the distribution of  $\tau_{du}$ , there are certain disagreements in the details. For example, signs of overestimation of  $\tau_{du}$  are seen in the Gulf of Aden and signs of underestimation are seen in the northern AS. A region of high  $\tau_{du}$  in the Red

Sea is also seen in MODIS-derived  $\tau_{du}$ . This is the region where the dust from Nubian Desert crosses the Red Sea through the Tokar Gap [Jiang *et al.*, 2009]. Clearly, MODIS (both Terra and Aqua) and RegCM4 show highest concentrations of dust over the Red Sea region.

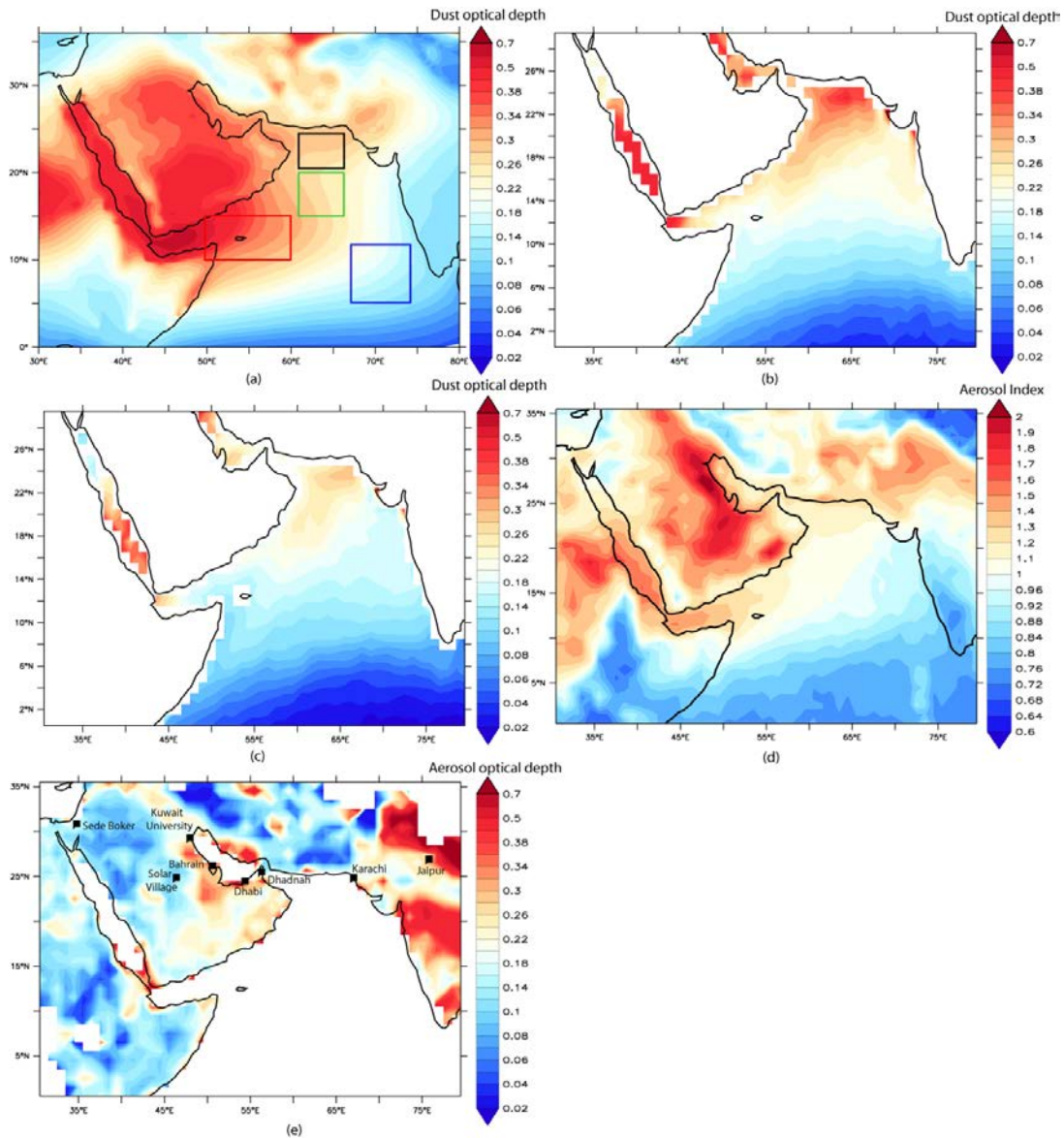


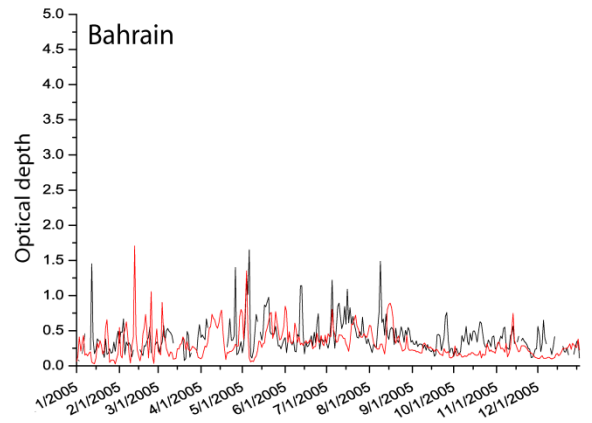
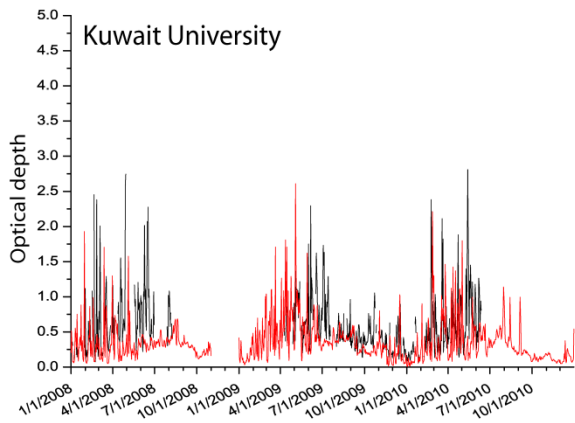
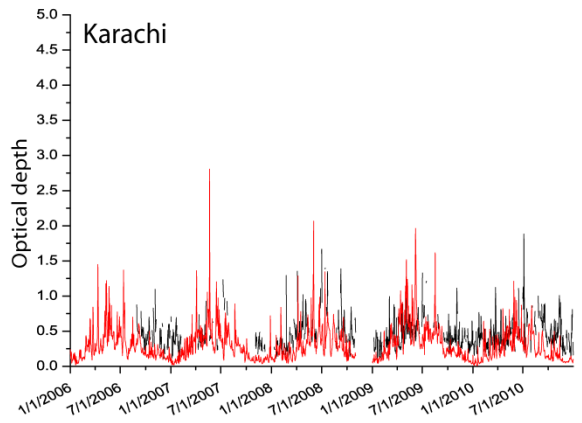
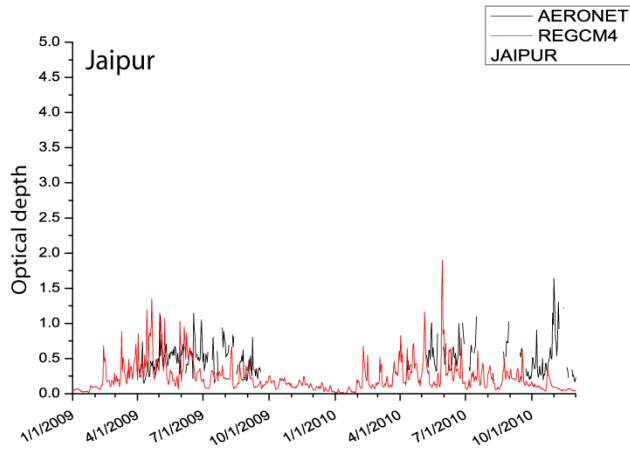
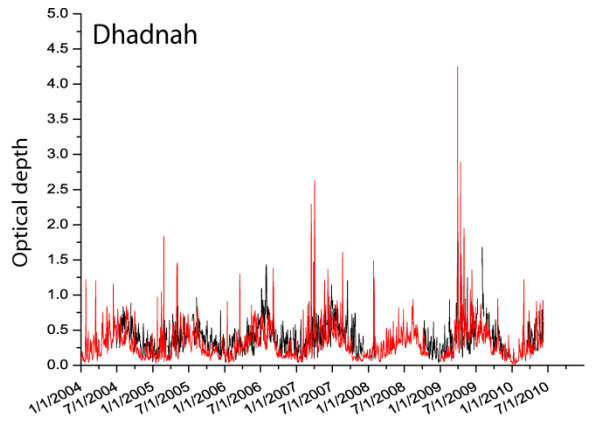
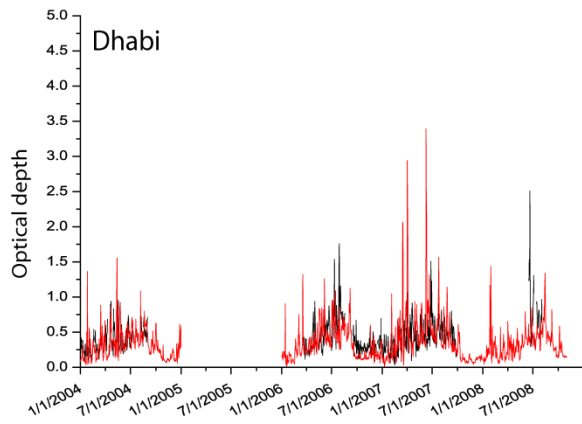
**Figure 4.2** Shading shows the spatial pattern of climatological (2001-2010) distribution of dust optical depth derived from (a) RegCM4 model, (b) MODIS/Terra and (c) MODIS/Aqua (for 2003-2010). The shading in (d) shows the climatological (2005-2010) distribution of Aerosol Index from OMI while that in (e) shows the total deep blue aerosol optical depth from MODIS/Aqua for the period of 2003-2010. The coloured boxes in (a) represents the four regions used to compare time-series of dust in Figure 4.4. The black squares in (e) indicate the locations of the AERONET stations that have been used for Figure 4.3.

Unfortunately, MODIS cannot provide information on  $\tau_{du}$  over land since high reflectivity of land at 550 nm wavelength prevents aerosol retrieval. Thus, only information over dark water surface can be used. In order to investigate the spatial pattern of dust distribution over land, AI data from OMI Aura for the period 2005-2010 has been used (see Figure 4.2d). Note again that AI is qualitative in nature and is sensitive to the height of the dust layer. Hence, a direct comparison between AI and  $\tau_{du}$  may not yield a clear picture, but some important inferences can still be drawn. Because, Aura satellite passes over a region during local noon time (just minutes after the passage of Aqua satellite) and because it detects dust at higher levels more readily, the distribution of AI from OMI Aura reflects the regions where high amount of dust is well mixed within the deep daytime boundary layer. The region of highest AI runs in a northwest-southeast direction from the Tigris-Euphrates Basin into the interior of the Arabian Peninsula along the southern coast of the Persian Gulf. A second region of high AI is seen from the Nubian Desert region into the Red Sea and the Gulf of Aden. The third region of high AI is over the arid regions of Pakistan, Afghanistan and Iran. The high AI in the region to the east is largely the result of anthropogenic contribution to ultraviolet absorbing aerosols. Similar to MODIS  $\tau_{du}$ , it appears that RegCM4 somewhat overestimates dust load over the Gulf of Aden, while that over the Red Sea is represented reasonably well. There also appears to be overestimation over the Arabian Peninsula bordering the northwest part of the Red Sea and underestimation in the northern part of the peninsula along the Persian Gulf coast. Similar patterns of over/underestimations are also revealed by the MODIS/Aqua deep blue  $\tau$  (see Figure 4.2e). Unlike AI, MODIS deep blue product fails to provide retrieval over dark surfaces and is not sensitive to the height of the aerosol layer, but is affected by the presence of biomass burning aerosols. Therefore, the high levels of  $\tau$  over India are largely contributions of biomass burning aerosols. There appears to be

overestimation over the entire Arabian Peninsula with respect to deep blue  $\tau$ . Also, the dust over the Nubian Desert region is not captured in the deep blue  $\tau$ , a feature that is well represented both in the model and AI retrievals. This type of differences in dust concentrations between the different satellite retrievals is documented for Sahara Desert as well [example, *Laurent et al.*, 2010; *Johnson et al.*, 2011; *Schepanski et al.*, 2012]. An attempt is made in the later part of this chapter to address the issue of discrepancies between the model and satellite observations.

### **4.3. Comparison with AERONET observations**

Further comparison of the modeled  $\tau_{du}$  has been done by taking daily AERONET data into account (see Figure 4.3). This has been done by considering  $\tau$  at 500 nm wavelength for 8 AERONET stations whose locations are shown in Figure 4.2e. These AERONET stations have been selected based on their proximity to the dust source regions. When considering AERONET data it is important to note that since the AERONET stations are located in populated areas, the  $\tau$  values may be influenced by local pollutions. It was reported by *Eck et al.* [2008] that the aerosols over United Arab Emirates and the adjacent Gulf region is a mixture of coarse desert dust and fine pollutants. Comparing  $\tau$  from AERONET with  $\tau_{du}$  from RegCM4 yields some differences between the two at daily scales with RegCM4 not capturing some high aerosol events and overestimating some other events. However, for all stations, the model seems to capture the seasonal cycle (high dust during summer and low during winter) appreciably well, which gives some confidence in the modeled dust cycle. The agreement is best for Solar Village which is a dust-dominated region lying in the heart of the Arabian Peninsula.



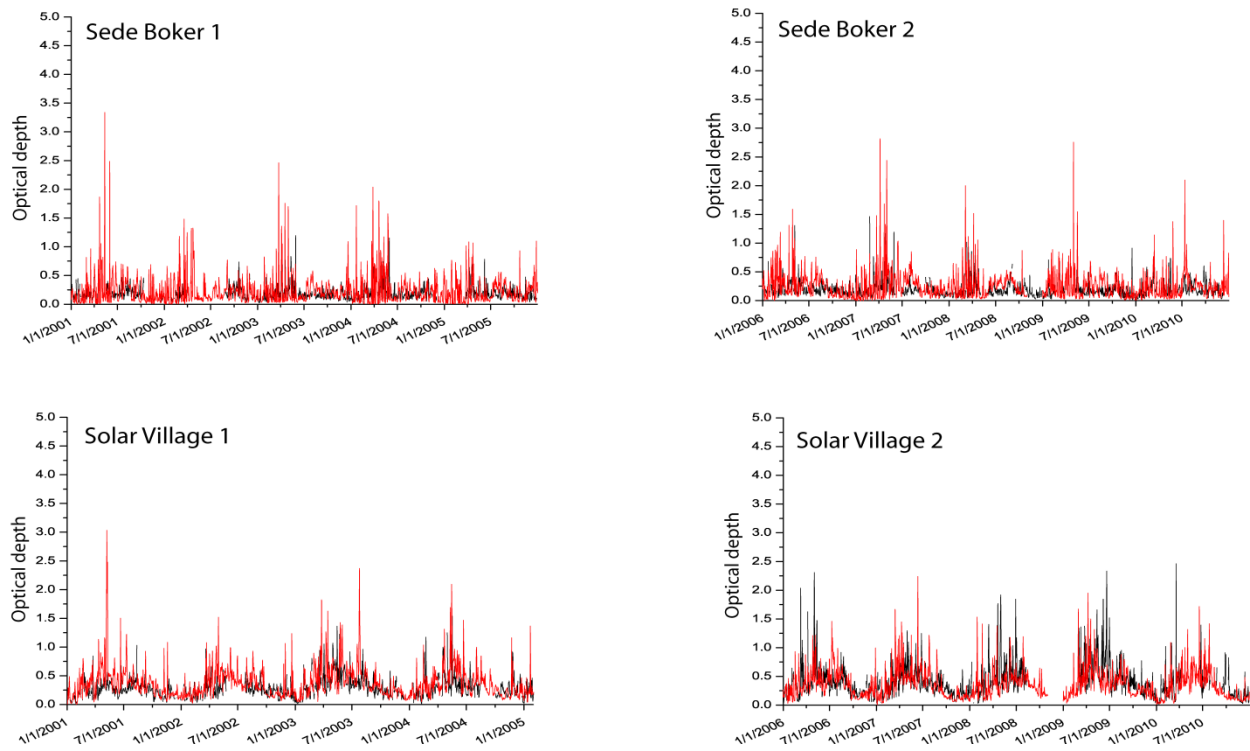


**Figure 4.3** Time-series of daily aerosol optical depth for selected AERONET stations (in black) and dust optical depth generated by the RegCM4 model (in red). The locations of the stations are marked in Figure 4.2e. The time-series have been broken up into two parts for Sede Boker and Solar Village as the data in these stations are available for 10 years.

#### 4.4. Comparison of model forcings with output

The temporal nature of evolution of modeled  $\tau_{du}$  over the different regions of the AS is shown in Figure 4.4 and is compared with  $\tau_{du}$  derived from MODIS/Terra.  $\tau_{du}$  is characterised by NEM minima and SWM maxima. While, the model captures the overall seasonal cycle of the evolution of  $\tau_{du}$  well, there are certain disagreements in details. The greatest disagreement between modeled and observed  $\tau_{du}$  is noticed during the SWM time. RegCM4 overestimates  $\tau_{du}$  over the southern AS and underestimates  $\tau_{du}$  over the northern AS during SWM.

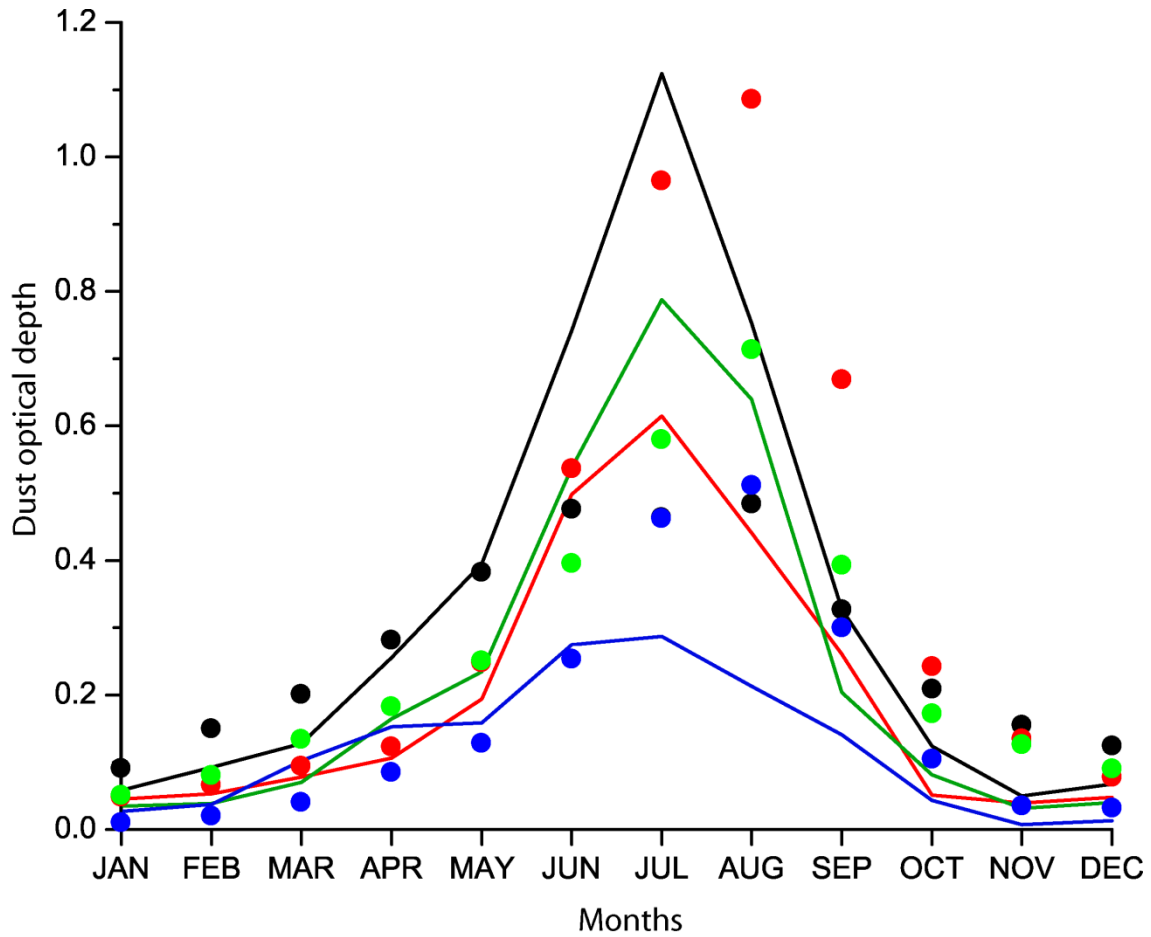


**Figure 4.4** Temporal evolution of dust optical depth over different regions of the Arabian Sea. The regions represented by each colour in the time series are indicated by the boxes in Figure 4.2a. The lines show the monthly climatology of dust optical depth obtained from MODIS/Terra observation for the period 2001-2010, while the small circles represent the same but for RegCM4.

Since the greatest departure of the simulated  $\tau_{du}$  from observations is during the SWM, a closer look at the conditions prevailing during the SWM is attempted to understand the main source of discrepancy between the model and the observations. It is seen in Figure 4.5a (and as pointed out earlier) that there is overestimation of simulated  $\tau_{du}$  over the Gulf of Aden (Figure 4.5b and c) and underestimation of simulated  $\tau_{du}$  in the northern AS. When considering AI for SWM (Figure 4.5d), the tract of dust from Nubian Desert into Red Sea and up to the Strait of Bab el Mandeb is

a much more prominent feature compared to MODIS observations. There is overall increase in dust activity over the Arabian Peninsula and southwest Asia. The high level of dust during SWM is also seen in the MODIS/Aqua deep blue product (Figure 4.5e). It was shown by *Ginoux et al.* [2012] that over the Arabian Peninsula and Middle East, the maximum contribution of dust to deep blue  $\tau$  is during May to July. When taking AI and deep blue  $\tau$ , it appears that over land there is underestimation of  $\tau_{du}$  over the Tigris-Euphrates region and overestimation northern part of the Red Sea region.

In order to examine the factors that might contribute to the high level of dust in the mouth of the Red Sea, the model output fields have been compared with the model forcing fields for the SWM period. For this, wind speed, temperature and relative humidity from NCEP/NCAR reanalysis have been compared against the same generated by the model. These are compared at the surface level which corresponds to 1008mb for RegCM4 and 1000mb for NCEP/NCAR reanalysis. This comparison is shown in Figure 4.6.

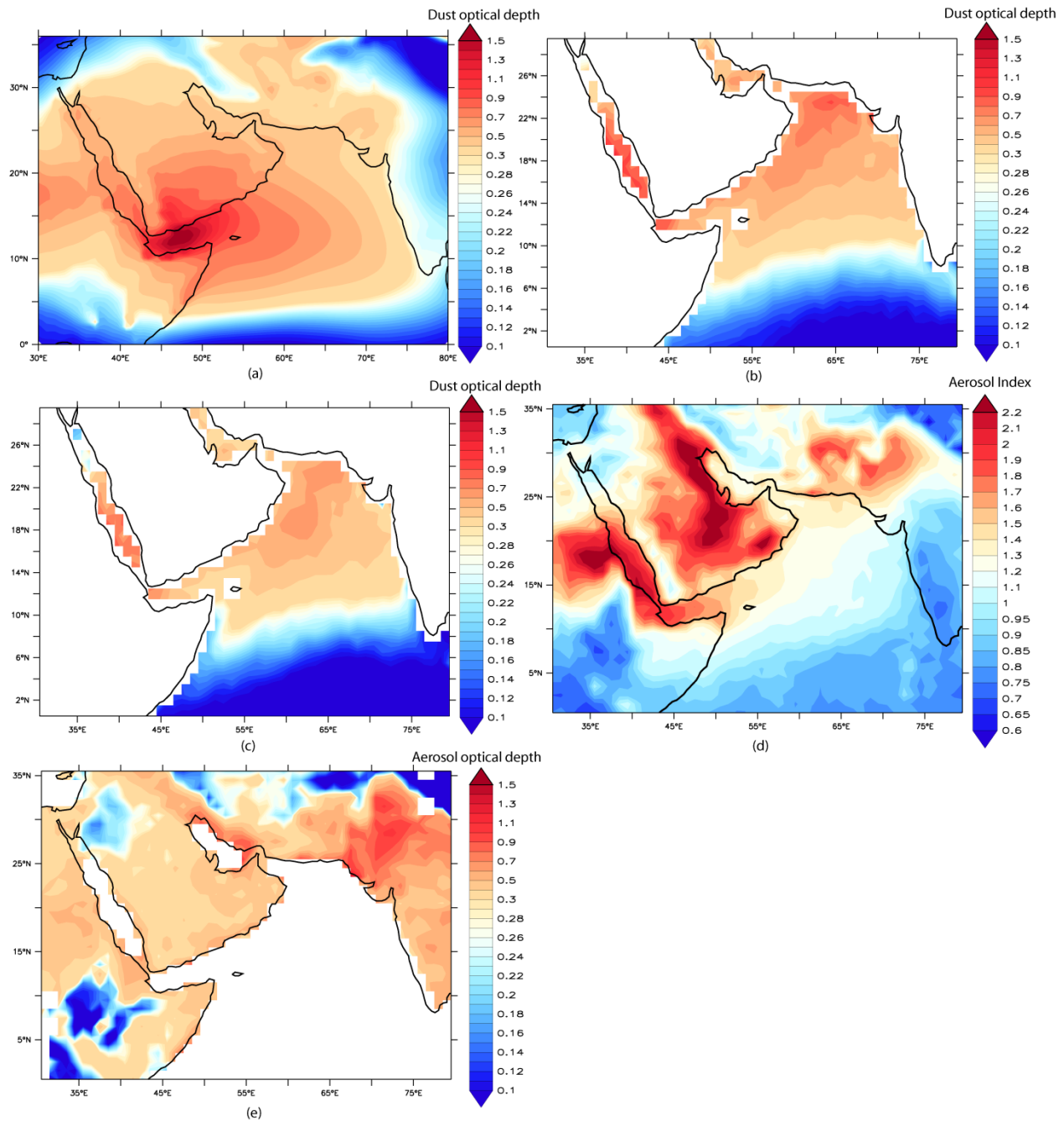


**Figure 4.5** Spatial pattern of climatological (2001-2010) distribution of dust optical depth derived from (a) RegCM4 model, (b) MODIS/Terra and (c) MODIS/Aqua (for 2003-2010) during southwest monsoon (SWM, June-September). The shading in (d) shows the climatological (2005-2010) distribution of OMI Aerosol Index for SWM while that in (e) shows the deep blue aerosol optical depth from MODIS/Aqua for the SWM of 2003-2010.

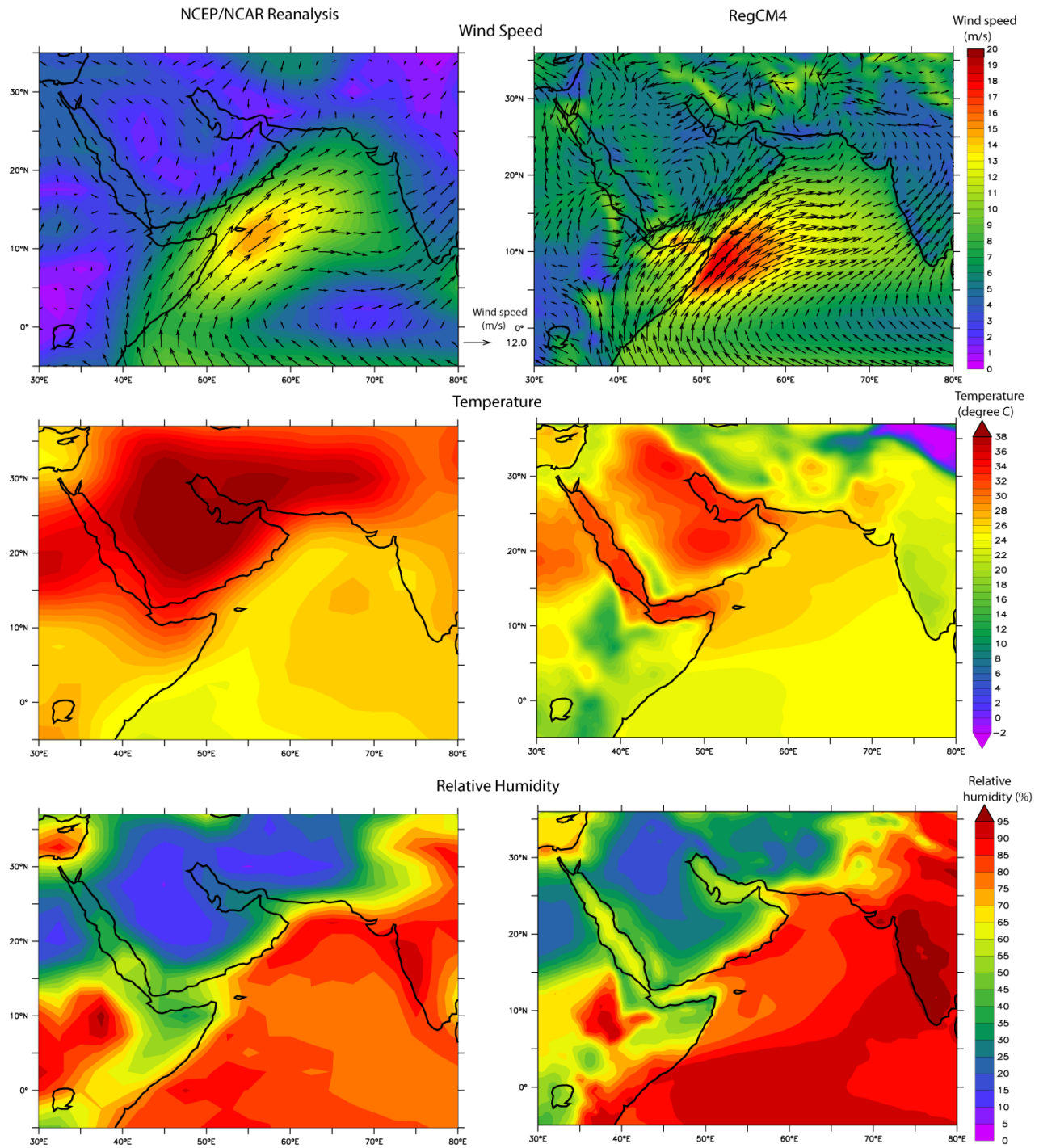


**Figure 4.6** Comparison between the meteorological fields from NCEP/NCAR reanalysis used to force RegCM4 model (left) and simulated meteorological fields (right) during the southwest monsoon. Shown are wind speed (in shading, unit:  $\text{m s}^{-1}$ ) overlaid with the vectors (top panel), temperature (middle panel) (unit in  $^{\circ}\text{C}$ ) and relative humidity (bottom panel) (expressed as %) at 1000 mb pressure level for NCEP/NCAR reanalysis and 1008mb pressure level for RegCM4 simulation.

In general, the model captures the dominant features of the spatial pattern of wind, temperature and relative humidity reasonably well though there are some differences in the details. It is seen that overall, RegCM4 simulated wind speed is of greater magnitude than NCEP/NCAR reanalysis which implies that wind friction velocity available for soil erosion (an important step in calculating dust emissions) will be overestimated. The greatest difference between the modeled and the reanalysis wind field lies off the coast of northeast Somalia which is the main axis of the Findlater Jet. Simulated wind speed exceeds the wind speed obtained from reanalysis product by about  $4 \text{ m s}^{-1}$  in the core of the wind maxima. Findlater Jet can blow dust off the northeast Horn of Africa and restricts dust to the western part of the AS. So, intensified Findlater Jet might result in the high levels of dust in the Gulf of Aden. Another difference between the model and the reanalysis is seen with respect to the wind vectors over the Arabian Peninsula. Whereas, the reanalysis show mostly northwesterlies over much of the Arabian Peninsula, the model shows intrusion of wind from the AS and the Persian Gulf over large part of the peninsula.

Taking the case of temperature, it is seen that overall modeled temperature is lower than that from NCEP/NCAR reanalysis. This is most prominent over the Arabian Peninsula, Iran, Pakistan, Afghanistan and India. As dust is allowed to interact with the forcing variables, the presence of dust leads to cooling of the surface temperature by blocking the shortwave radiation. A lowering of temperature will lead to lowered dust generation by dry convection, which may explain the underestimation in  $\tau_{\text{du}}$  over northern AS. However, such a lowering of temperature by dust feedback is not apparent in the Gulf of Aden.

Simulated and reanalysis relative humidity generally agree well, though with some exceptions. It is seen that model simulates higher level of relative humidity in south and east AS and over southwest Asia. While higher relative humidity may lead to more precipitation and removal of

dust by wet deposition over southern part of AS, the same cannot be true for southwest Asia since relative humidity is much lower than the saturation level. Since the humidity and  $\tau_{du}$  is inversely related, it would seem that the pattern of distribution of relative humidity is unable to explain the discrepancy between simulated and observed  $\tau_{du}$ . Also shown in Figure 4.7 is the comparison in the pattern of precipitation distribution for SWM between the model and that obtained from Tropical Rainfall Measuring Mission (TRMM). It is seen that the model, though captures the pattern, overestimates precipitation along the west coast of India, southern AS and over the northern AS. Precipitation is an important mean of removing dust from the atmosphere, thereby affecting  $\tau_{du}$ . It will be shown in Section 5.2 that dust is transported at higher levels over the southern AS and at comparatively lower levels over the northern AS. So, while, increased precipitation over the northern AS can act to remove dust and reduce  $\tau_{du}$ , the same may not hold entirely for overestimation of  $\tau_{du}$  over southern AS. The increased precipitation, may remove dust only from the lower level.

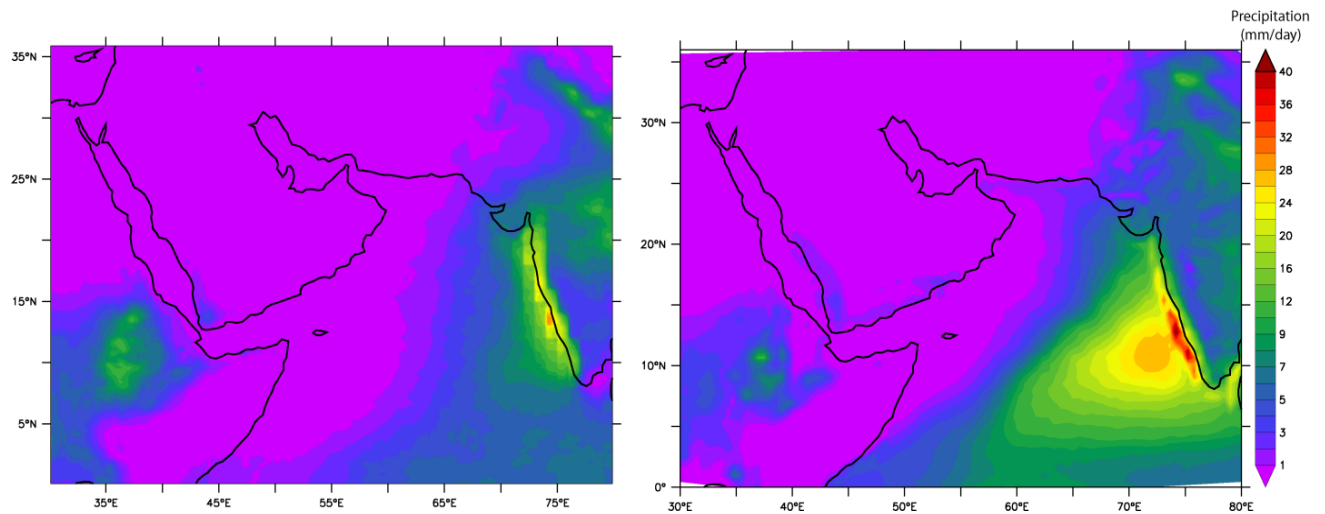


**Figure 4.7** Comparison of precipitation ( $\text{mm day}^{-1}$ ) between TRMM (left) and that generated using RegCM4 model (right) over the Arabian Sea and the surrounding regions for the southwest monsoon period.

## 4.5. Summary

Overall, the model represents the seasonal cycle and the spatial distribution pattern of dust over the AS reasonably well, with some differences with the observations regarding the details of the dust distribution and the relative strength of each dust source. There is an overestimation of  $\tau_{du}$  over the southern and western AS, especially in the Gulf of Aden and there is an underestimation of  $\tau_{du}$  over the northern AS. It can be concluded that the overestimation of  $\tau_{du}$  over the southern AS is primarily the result of an intensified Findlater Jet in the model during the SWM period that brings more soil material from northeast Africa and blocks the crossing over of dust from the Arabian Peninsula and Africa into the open AS at lower levels. The underestimation in the northern AS appears to arise from the simulated colder surface temperature which will have negative impact on the development of dry convection.

# CHAPTER 5

## DUST CYCLE OVER THE ARABIAN SEA

### 5.1 Dust Emission

The emission of dust from the soil surface vulnerable to erosion is the first step in understanding the dust cycle. Determining the amount of dust that is emitted along with the factors responsible is a prerequisite in studying the dust load in the atmosphere and ultimately its climatic effects. Here, the seasonal cycle of dust emission around the AS is studied first, followed by a detailed analysis of the meteorological factors responsible for dust emission in selected regions.

#### 5.1.1. Seasonal cycle of dust emission

The seasonal cycle of dust emission in the arid and semi-arid regions surrounding the AS is presented in Figure 5.1. The main regions from where significant quantity of dust (greater than  $500 \text{ mg m}^{-2} \text{ day}^{-1}$ ) is mobilized at different times of the year are: the Thar Desert, the Tibetan Plateau, the southeastern flank of the Caspian Sea, southwest Asia, the entire Arabian Peninsula, the Nubian Desert and Somalia. During the NEM time high dust emissions are seen over southwest Asia and the Tibetan Plateau (see Figure 5.1a). With the progress of the year, dust activities in these regions shrink, while those over other regions gain momentum. High emission in excess of  $5000 \text{ mg m}^{-2} \text{ day}^{-1}$  is seen over the northwest Arabian Peninsula and over the Sistan region in Iran during SIM (Figure 5.1b). High dust emission of  $1000 \text{ mg m}^{-2} \text{ day}^{-1}$  is seen over the Thar Desert. With the advent of SWM season, the regions of high dust emission shifts to the southern part of the Arabian Peninsula and the northeast coast of Somalia (Figure 5.1c). Finally,

FIM is the most tranquil time of the year when the dust emission around the AS is at its minima (Figure 5.1d).

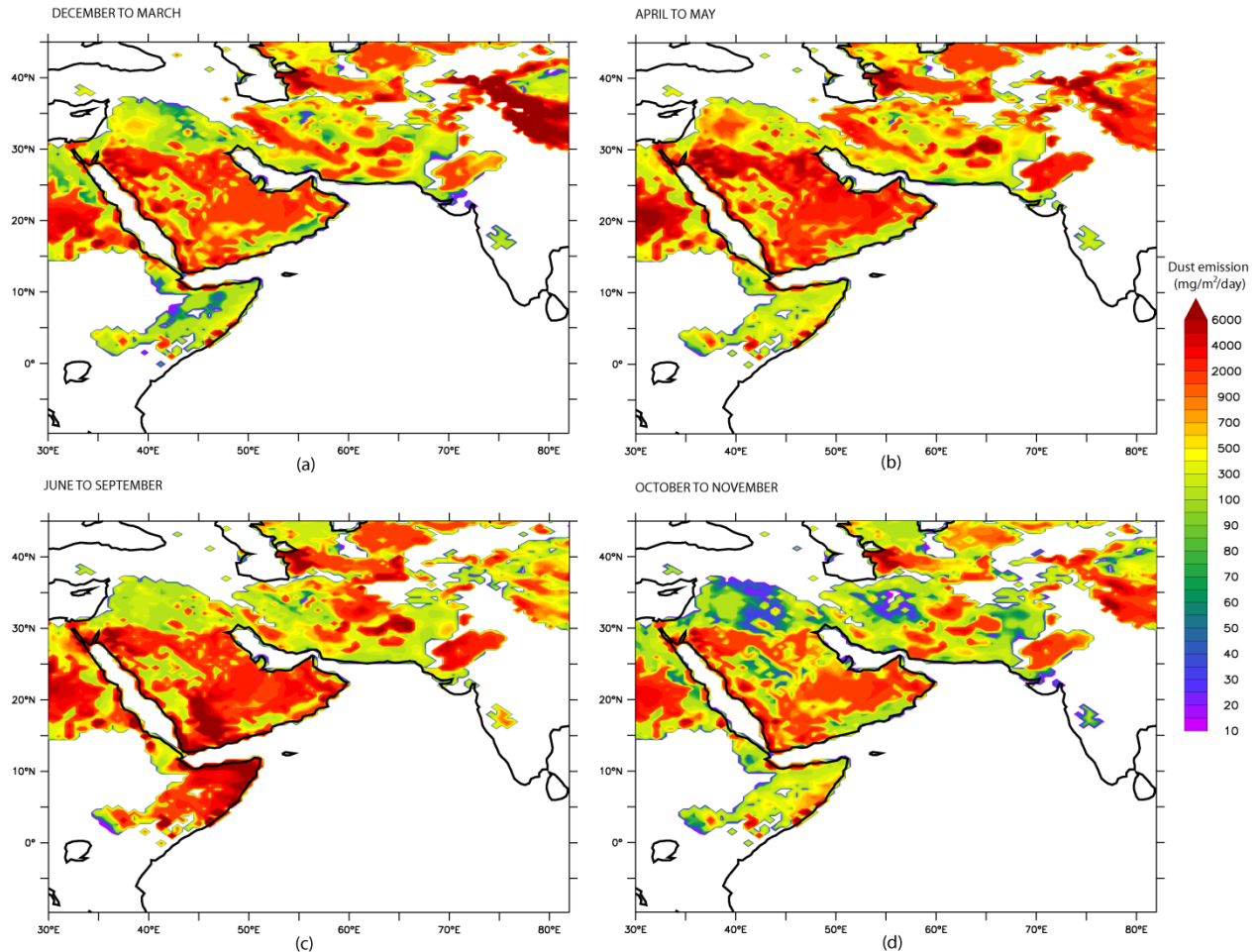


**Figure 5.1** Seasonal cycle of dust emission in the regions surrounding the Arabian Sea for (a) northeast monsoon (b) spring intermonsoon (c) southwest monsoon and (d) fall intermonsoon.

Comparison of dust emission from RegCM4 with some other models yield emission ranges from  $55 \text{ mg m}^{-2} \text{ day}^{-1}$  to about  $600 \text{ mg m}^{-2} \text{ day}^{-1}$  [Ginoux *et al.*, 2001] and  $20 \text{ mg m}^{-2} \text{ day}^{-1}$  to  $1700 \text{ mg m}^{-2} \text{ day}^{-1}$  [Zender *et al.*, 2003]. While the former study uses maximum diameter of dust of  $6 \mu\text{m}$ , the latter study uses maximum diameter of dust of  $10 \mu\text{m}$ . Therefore, most of the coarse mode aerosols which are important in the dust source regions are discounted in their studies. Note that RegCM4 use maximum diameter of dust of  $20 \mu\text{m}$ . It is seen from RegCM4 simulations that the

contribution of dust particles having diameter less than 5.0  $\mu\text{m}$  to total dust emission is less than 30%. Since the maximum emission is around 5000  $\text{mg m}^{-2} \text{day}^{-1}$ , the maximum contribution of particles having diameter less than 5.0  $\mu\text{m}$  becomes 1500  $\text{mg m}^{-2} \text{day}^{-1}$ . This falls within the range of emissions that have been obtained from other global models.

**Table 5.1** Dust emissions in the regions around the Arabian Sea (0-36°N latitude, 32-75°E longitude) during different seasons

Season	Emissions ( $\text{mg m}^{-2} \text{day}^{-1}$ )	Contribution to total annual emission (%)
NEM	456.3	26.6
SIM	604.1	17.8
SWM	795.4	46.8
FIM	297.4	8.8

Table 5.1 lists season-wise total dust emissions around the AS. If the main regions of dust mobilization are compared with the orography as shown in Figure 5.2, few features emerge. The Thar Desert is associated with topographic low; the dust sources of southwest Asia are mainly intermontane in nature; the dust sources to the southwestern part of the Arabian Peninsula lie in the piedmont of the northwest-southeast oriented Asir Mountains to the south and Hejaz Mountains to the north; the regions of high dust emission over northeast Somalia are associated with the highlands in Somali and Ethiopia. This conforms to the fact that the highlands provide the required sediments that are eroded by the rivers and are deposited when the rivers debouch on a plain. These sediments derived from the highlands are the main material for transport [Prospero *et al.*, 2002]. Also, the presence of highlands surrounding the main dust emission

region is important in channelizing the wind that pick up dust. Examples are the east-west blowing Tokar Jet through the Tokar Gap in Sudan [Jiang *et al.*, 2009], the northwesterly *Shamals* that blow along the axis of the Persian Gulf channelized by the Zagros Mountains to the north and the Arabian Plateau to the south [Perrone, 1979] and the *Levar* wind that blow in the north-south direction and picks up dust in the Sistan region [Kaskaoutis *et al.*, 2014].

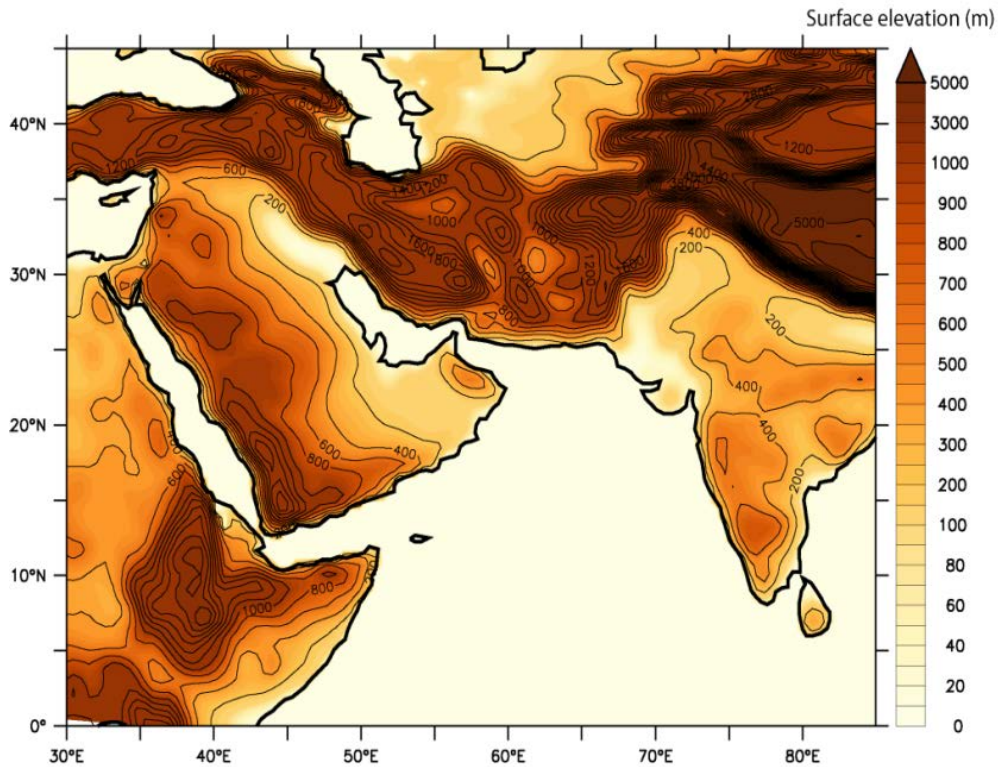


**Figure 5.2** Map showing variation in elevation over the landmass surrounding the Arabian Sea.

### 5.1.2. Region-wise meteorological conditions favouring dust emissions

The seasonal cycle of dust emission is explored further by looking at the time of the year when maximum dust emission is noticed over a region. This is depicted in Figure 5.3 which classifies the dust source regions according to the season when dust emission over the region is at its peak. It is seen from the figure that maximum dust is mobilized around the AS during SWM time. This

is followed by NEM time over southwest and central Asia and SIM over the northern part of the Arabian Peninsula. There are only 2 isolated pockets (one in Iran and other in southwest Arabian Peninsula) where dust emission peaks during the FIM, probably related to the transition of conditions between SWM and NEM. Based on the seasonal distribution of the peak period of dust emission 11 representative regions have been selected for further analysis of the meteorological conditions that lead to dust emission. The size of the boxes has been chosen such that they encompass the regions that have typical characteristics associated with dust emissions for that region. The main characteristics of the regions are discussed in details below.

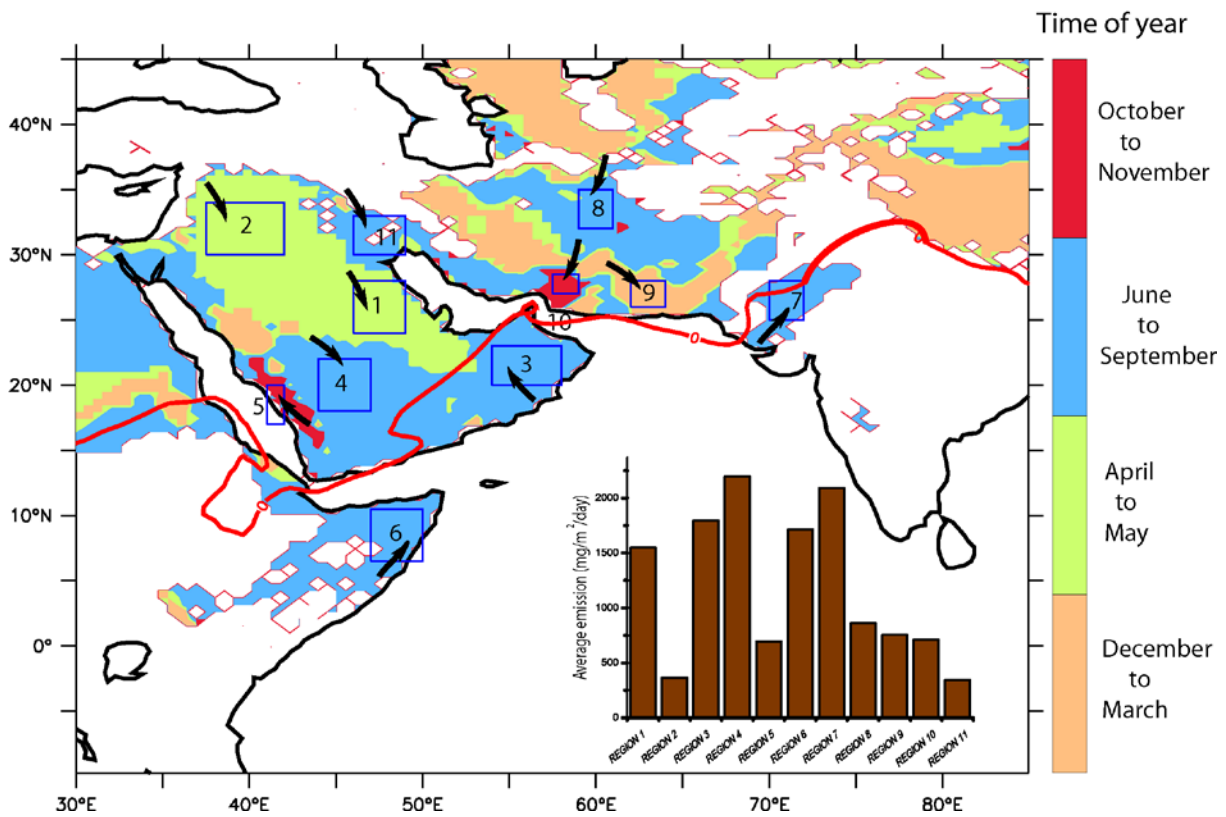


**Figure 5.3** Time of the year when the maximum dust emission takes place in regions surrounding the Arabian Sea. The boxes mark the regions that have been taken up to study the meteorological conditions responsible for dust emission. The thick red line marks the position of the intertropical convergence zone during the southwest monsoon period demarcated as the zone where the meridional component of the wind becomes zero. The arrows mark the prevailing wind directions during the time of maximum dust emission over a region. The column graph shows average emission (unit  $\text{mg m}^{-2} \text{day}^{-1}$ ) for each of the 11 regions denoted by the boxes.

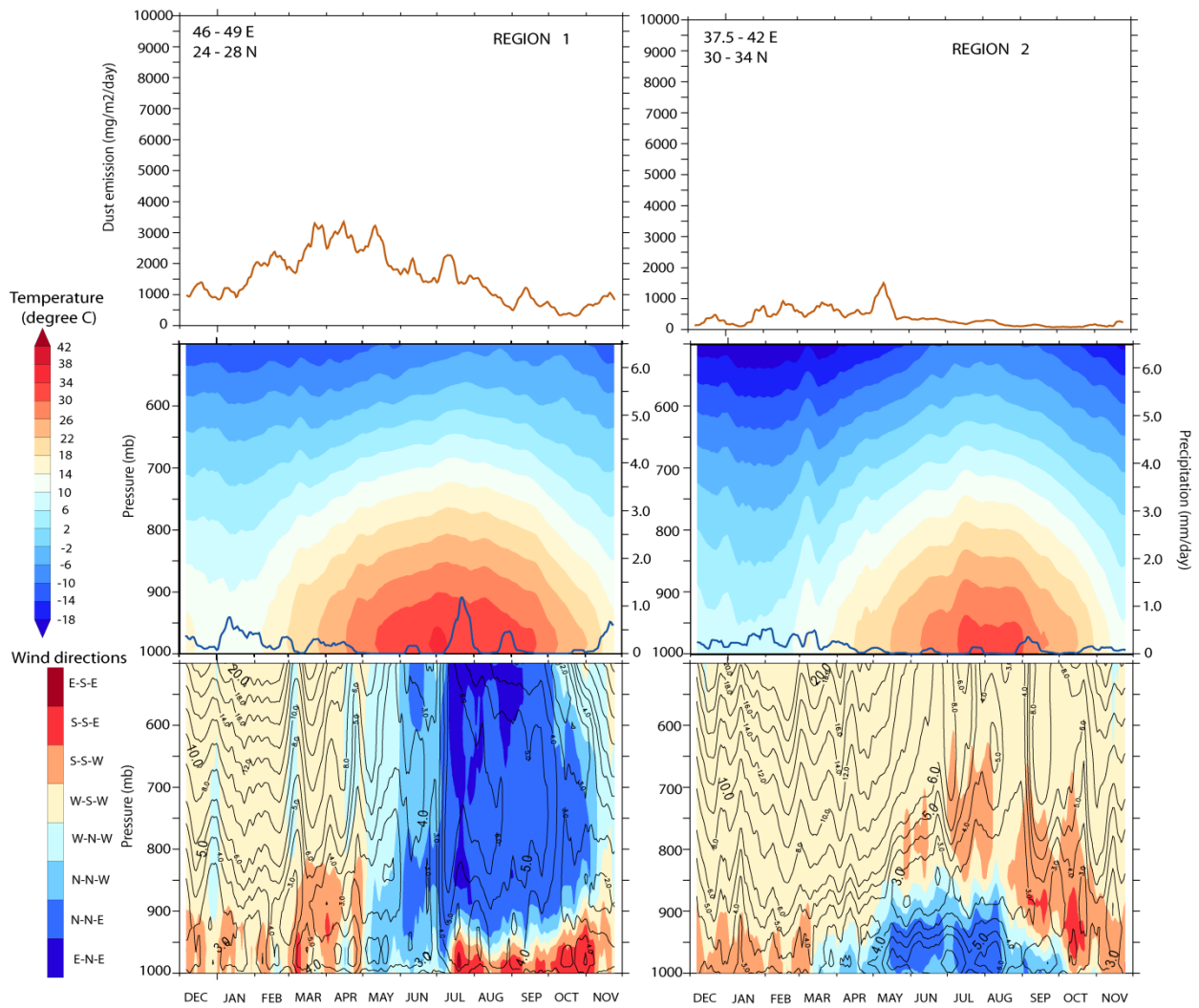
**Region 1:** Region 1 encompasses the central part of the Arabian Peninsula with the Rub al Khali Desert as the main dust source. Dust emission starts picking up from March and reaches its peak during April-May. Although, this is the time of the year when the temperature starts to increase, the highest temperature is attained during June-July period. During the winter time, the atmosphere over this region is stably stratified with low surface wind speed and high wind speed aloft. However, with the increase in temperature there is a breakdown in the stratification of the atmosphere as convection system sets up. This mixes the momentum from the geostrophic layer above into the surface frictional layer and results in an increase in surface wind speed and a reduced wind speed aloft. The main time for rainfall is between January and April and is related to the westerlies. The model also shows another peak during July associated with the incursion of the southeasterlies, although this is not captured in TRMM rainfall distribution for the region. Recall that wind from the AS and the Persian Gulf penetrated too much inland into the Arabian Peninsula during the SWM period (Figure 4.6 in Chapter 4). This could probably give rise to the wetness in this region as seen in the model. However, this does not seem to affect the seasonality of dust emission which is further confirmed by comparison with AERONET station in the Solar Village (Figure 4.3 in Chapter 4). During the time of maximum dust emission the surface wind speed is high and the wind direction is northwesterly. This type of situation is associated with summer *Shamals* that are associated with winds blowing in response to the pressure gradients set up by the intensification of the summer time low pressure over the Arabian Peninsula [Membery, 1983; Rao, 2003]. Dust entering higher levels of the atmosphere is transported towards the east.

**Region 2:** Located to the northwest of Region 1, Region 2 experiences maximum dust emission during May which is the driest time of the year. The region receives winter rainfall associated with westerlies. The peak dust emission period coincides with high temperature and set up of

convection by breakdown of the geostrophic flow. This leads to the highest mean surface wind speed of about  $5 \text{ m s}^{-1}$  being observed during the month of May. The convection mechanism helps to lift dust to very high levels in the atmosphere and its subsequent transport at higher levels. However, the region experiences much less temperature and precipitation compared to Region 1. Similar to Region 1, dust emission over this region is associated with northeasterly and northwesterly winds associated with the *Shamal* weather system. Another factor that can give rise to dust emission here during the spring time is the *Sharav* cyclone [Alpert and Ziv, 1989; Dayan et al., 2008] resulting from temperature contrast between the warm North African continent and the cold Mediterranean Sea. These cyclones are characterised by warm front to the east and cold fronts to the west. *Sharav* cyclones travel eastwards and are capable of entraining huge volume of dust into the atmosphere.

**Region 3:** Region 3 is located in Oman. Maximum dust emission over this region takes place during June-July. This is the time of the year when the temperature, precipitation and wind speed is at its annual maximum. Dust emission is associated with incursion of the southeasterly wind associated with the SWM system over the AS. Dust emitted from this region is carried in northeasterly direction after being lifted into higher levels in the atmosphere by convection. It has been conceived that the precipitation in this region is important in producing and transporting the material that is blown as dust [Zender et al., 2003] because of the temporal overlap in the period of maximum dust emission and summer precipitation. Another important means of dust mobilization in this region is the *Haboobs*, which are giant walls of dust formed from the leading edge of the cold downdrafts in a region of vigorous convection [Membrey, 1985; Miller et al., 2008]. They can be about a kilometre in height and their passage are characterised by sharp drop in visibility. These *Haboobs* can range in size from 20 km to more than 2000 km and can

travel at a speed of 35-40 km hr<sup>-1</sup>. [Miller et al., 2008]. Several *Haboobs* have been reported by Miller et al. [2008] to have formed over the Al Hajar range in northeastern Oman and subsequently moved westward with the prevailing southeasterly (also shown in Figure 5.4). Thus the incursion of moisture from the Gulf of Oman associated with the SWM wind system is a requisite for *Haboob*-like dust storm initiation.



See next page for figure caption.

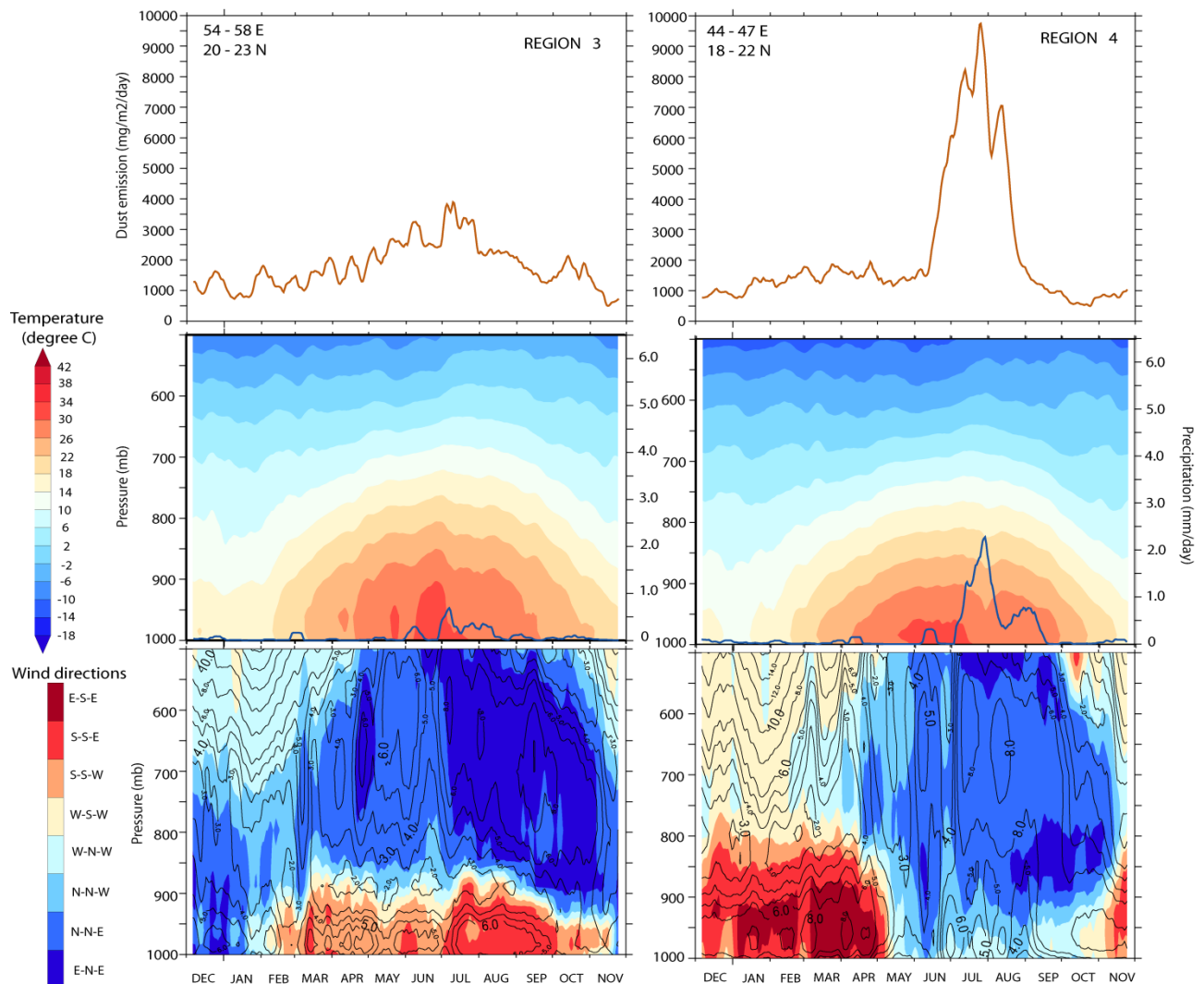


**Figure 5.4** Annual cycle of meteorological conditions that are associated with dust emission in the different regions surrounding the Arabian Sea. Shown are the fields for Region 1 to 4 as demarcated in Figure 5.3. The top panel for each region shows dust emission; the shadings in the middle panel shows the time versus height evolution of temperature and the blue curve shows the distribution of precipitation; the bottom panel shows the time versus height evolution of wind direction (shading) and wind speed (contours). All fields shown are daily climatologies that have been smoothed by ten days' running mean.

**Region 4:** Region 4 lies in the southwestern part of the Arabian Peninsula. The region is characterized by dust emission maxima during the month of July. Interestingly, the wind speed is comparatively lower than other times of the year; however the atmosphere over the region shows signs of intense turbulence due to the high heat over the region. This is evident from the time

versus height evolution of the wind speed which signs of break-down of the atmospheric stratification from May to September. Like most of the regions over the Arabian Peninsula, the prevailing wind direction associated with dust emission is northwesterly.

**Region 5:** Dust emission in this elongated region located bordering the Red Sea is at its height during the months of October-November. There is a secondary maxima during May-June. The October-November period is associated with minimum precipitation and the fall of the temperature curve. Dust emission is related to the southeast component of the wind over the Arabian Peninsula which displays maximum wind speed ( $\sim 10 \text{ m s}^{-1}$ ) during this time of the year [Pedgley, 1974]. The outblowing wind from the Arabian Peninsula into the Red Sea further gains momentum on interaction with the complex topography of the region. The scarp face of the Arabian Plateau runs almost parallel to the Red Sea. Any gaps in these highlands give rise to the cross-wind component across the axis of the Red Sea [Clifford *et al.*, 1997; Jiang *et al.*, 2009]. This topographically-reinforced wind is the main harbinger of dust storms in this region.

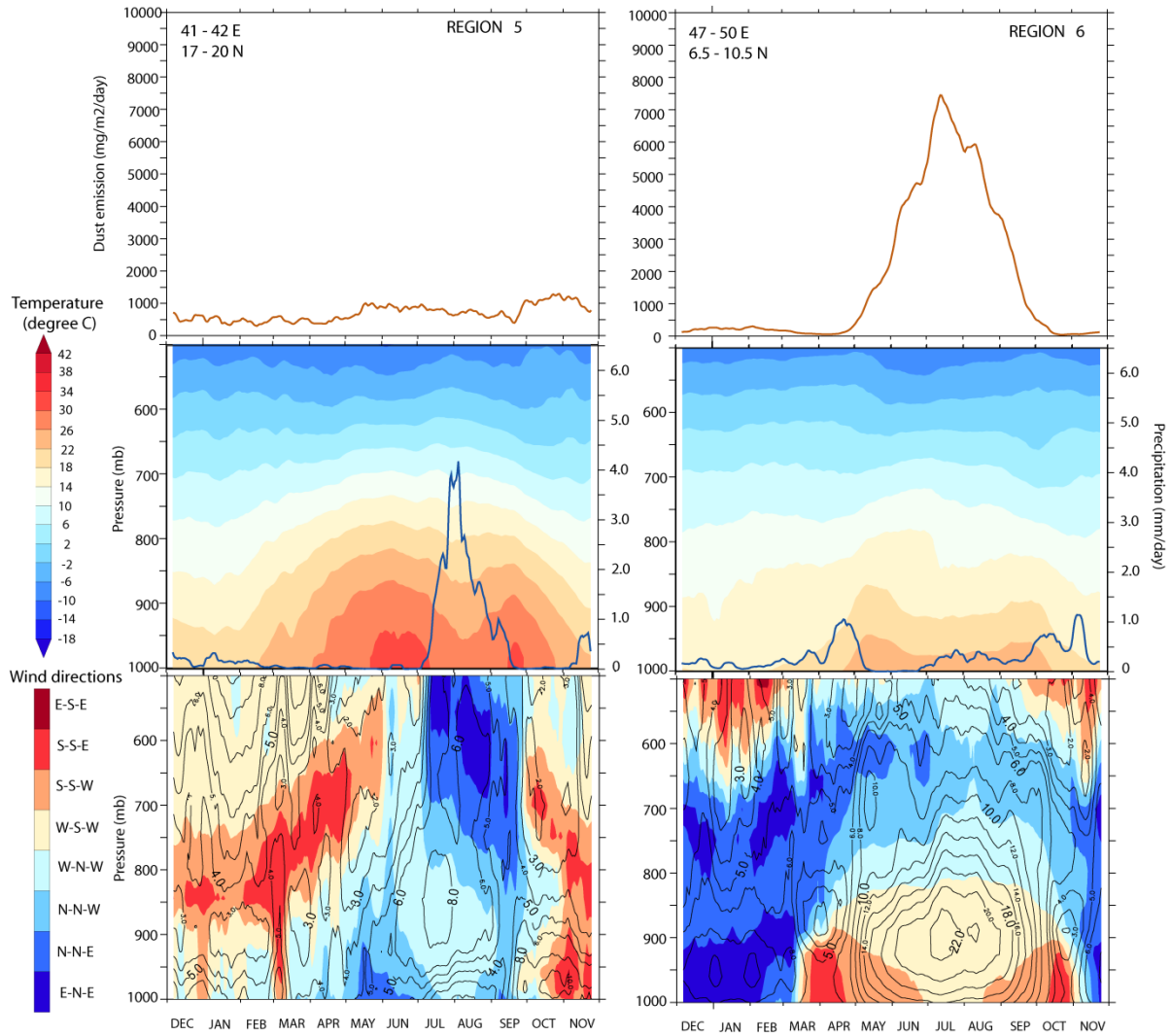
**Region 6:** The SWM wind system is responsible for maximum dust emission over northeast Somalia during the month of July. Somalia experiences rainfall maxima twice a year: Gu from April to June and Deyr from September to November [Leon and Legrand, 2003]. Maximum dust emission takes place during the intervening dry period. This is related to the Findlater Jet [Findlater, 1969; Findalter, 1977] which forms the part of the SWM wind where the maximum cross-Equatorial energy is concentrated. The wind speed at the surface is as high as  $16 \text{ m s}^{-1}$ . The maximum wind speed ( $22 \text{ m s}^{-1}$ ) is concentrated at 900 mb pressure level. Above that, the wind speed goes on decreasing to about  $4 \text{ m s}^{-1}$  at 500 mb pressure level. Also, there is a 2-layer structure of the wind with the predominance of southwesterly at lower levels and northwesterly at higher levels. Restricted by the presence of the East African Highland to the west, the

Findalter Jet picks up soil particles from the Mudug Plain in east-central Somalia and the Guban: a xeric grassland bordering the coastal region of Somalia which is crisscrossed by numerous ephemeral streams or wadis.

**Region 7:** This region encompasses the Thar Desert lying in the Indo-Pakistan border. The maximum dust activity is seen during the summer months of May-June [Middleton, 1986; Deepshikha et al., 2006] associated with the intense summer heat over the Indian Subcontinent. This marks the development of the convective unstable boundary layer. Dust activity is associated with the westerly winds locally known as Loo. With the onset of precipitation from the SWM wind, the dust activity subsides. Similar to region 6, there is a 2-layer structure of the wind: southwesterly in the lower levels and easterlies in the upper levels. Therefore, dust picked up by the prevailing wind is transported to the east near the surface, but are transported towards south and west in the upper levels.

**Region 8:** The border region between Iran and Afghanistan is a very active dust source supplying high amount of dust to the AS. The region receives rainfall in winter associated with the migration of the western disturbances from the Mediterranean region. Highest dust emission is seen during the month of August associated with the high heating that sets up a convection system. The region is dotted with numerous ephemeral lakes formed by the drainage of the Helmand River. The drying of these lakes during the summer months leads to the uplift of loose soil particles [Rashki et al., 2013]. The northerly *Levar* are the main dust raising winds and the dust is transported in a southerly direction. Wind speeds of about  $12 \text{ m s}^{-1}$  are indicated by the model during the month of August. The occurrences of dust storms in this region has been related to the intensification of high pressure over the Caspian Sea and low pressure over the Indo-Iranian region extending into the Arabian Peninsula [Kaskaoutis et al., 2014]. This leads to

increased pressure gradient, which is conducive towards the blowing of *Levar*. The mountain-valley like nature of the topography of the region channelizes the wind which leads to the formation of a low-level jet [*Kaskaoutis et al.*, 2014] that is important in picking up dust.



See next page for figure caption.

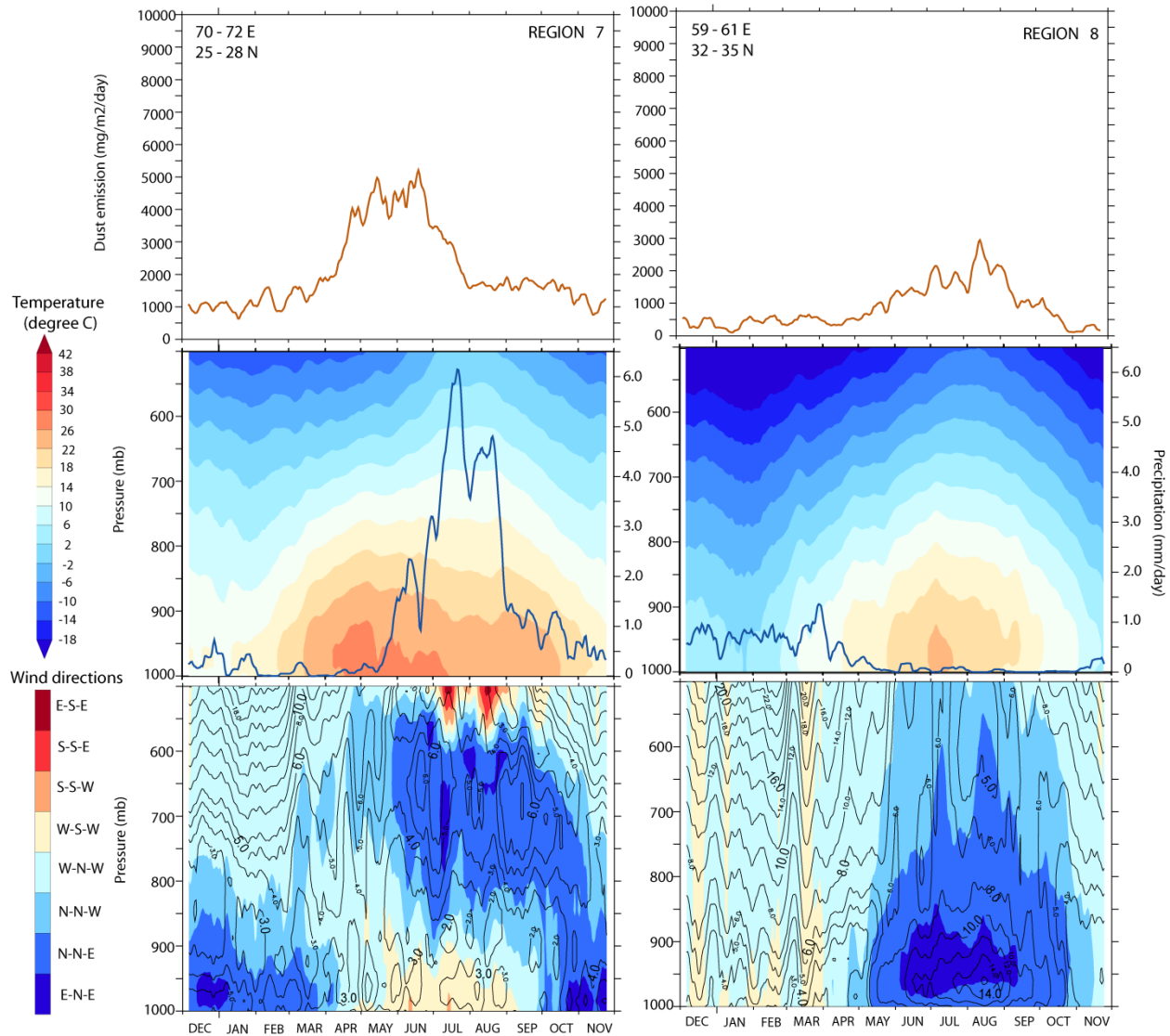


**Figure 5.5** Same as for Figure 5.4 but for Regions 5 to 8.

**Region 9:** Region 9 lies in the Makran region bordering Pakistan and Iran. There are two rainfall peaks: one during the winter and the other during the summer. Within this narrow band, the precipitation appears to be associated both with the SWMs and the winter time western disturbances. The highest dust emission is noticed in this region during the winter months of January-February. This is associated with the northwesterly wind system known as winter *Shamals* [example *Abdi Vishkaee et al., 2012*]. During the winter time *Shamals* are caused by

low pressure systems that move eastwards from the Mediterranean region as cold fronts. These systems are responsible for bringing rainfall over southwest Asia. On losing moisture when moving over the arid land, the wind lifts up dust along the leading edge of the cold front. The dust is transported from northwest to southeast direction along the path of the front. Thus, unlike other regions, the dust storms here are not associated with high heating of landmass and development of convective layer as is indicated by the stratified vertical profile of the wind.

**Region 10:** Region 10 lies in the coastal part of Iran to the north of the Strait of Hormuz. September-October is the time of the highest dust emission in this region. The location of this region coincides with the location of the ITCZ during the SWM time (refer to Figure 2.1b). Therefore this is a region of transition where the moist monsoon wind system meets the dry continental outflow. The region receives winter rainfall. The time of highest dust emission coincides with the dry time of the year along with high temperature and northerly wind having speed in excess of  $10 \text{ m s}^{-1}$ . The vertical profile of the wind shows the existence of a convection system in response to the summertime heat. This dry convection is instrumental in raising dust into the higher levels of the atmosphere. In a similar manner to Region 8, the wind blows in response to the north-south pressure gradient existing during this time of the year and is mainly responsible for transporting dust to the southwest. It is also seen from *Kaskaoutis et al.* [2014] that with the progress of the SWM season, the high pressure over the Caspian Sea becomes more established which might explain why dust activity is experienced in this region during the waning phase of the boreal summer. The wind is northerly throughout the entire vertical extent of the atmosphere during the dust-raising season.

**Region 11:** This region lies in the lower Tigris-Euphrates basin in Iraq in the head of the Persian Gulf. Dust emission reaches its maximum value during the months of June-July. The region

receives winter rainfall. Therefore, dryness sets in during the following summer with temperature soaring to more than 40°C. The pressure gradient between the high over the Mediterranean and the Indo-Iranian low is a critical factor for the blowing of dust-lifting wind [Rao *et al.*, 2003; Awad and Mashat, 2013]. This dust-lifting wind known as summer *Shamal* is from northwesterly direction and blows along the axis of the Persian Gulf. The highest wind speed of 6 m s<sup>-1</sup> is seen during this time of the year. Overall, below 700 mb pressure level the dust is transported towards the southeast and above 700 mb the transport direction is shifted northeastwards.

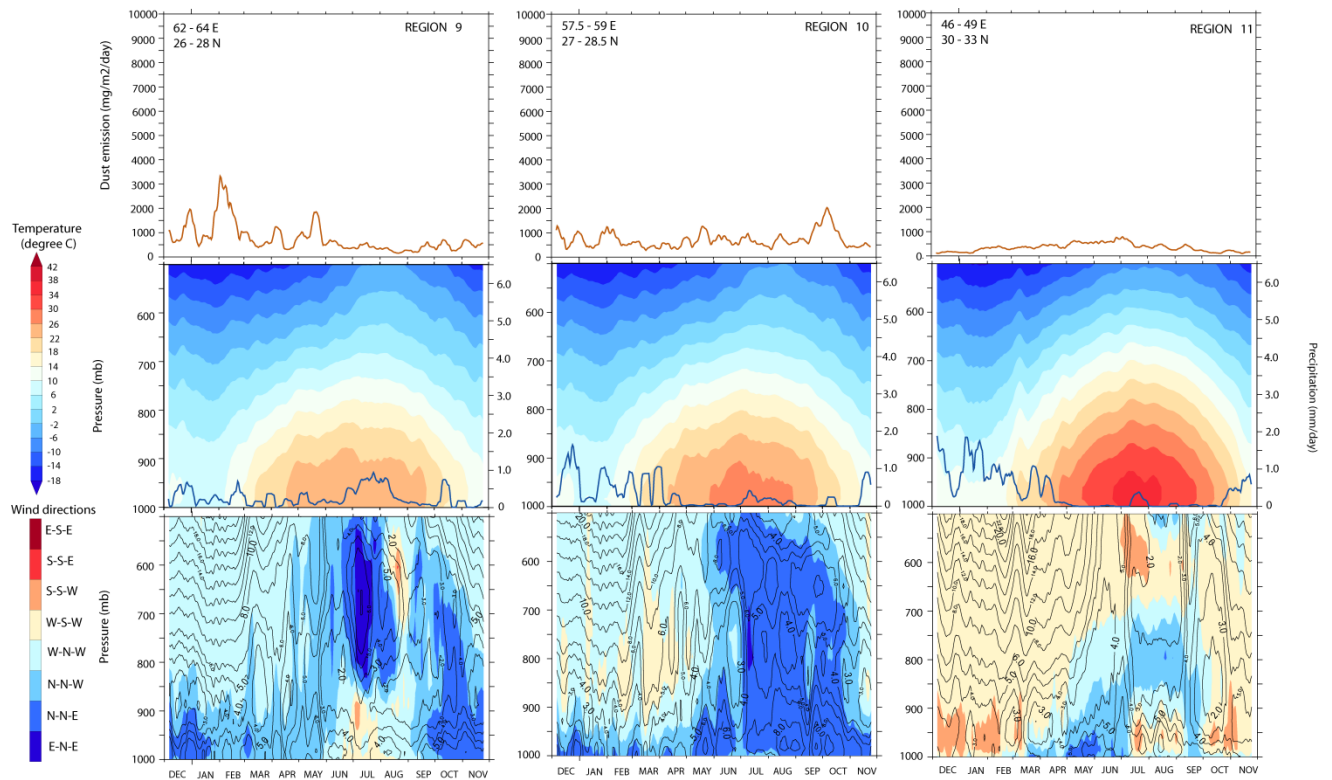


**Figure 5.6** Same as for Figure 5.4 but for Regions 9 to 11.

## 5.2. Dust transport

It is evident from the discussions in section 5.1 that the maximum dust emission takes place during the boreal summers. However, in different regions surrounding the AS dust emissions are

associated with different factors and different types of wind regimes. Accordingly, it can be expected that there will be diverse routes of dust transport across the AS and into India. In this section the dominant dust transport routes are discussed with greatest emphasis on the SWM time when  $\tau_{du}$  is highest over the AS.

The pattern of dust concentration at different pressure levels in the atmosphere along with vectors of dust mass flux for SWM are shown in Figure 5.7. Maximum dust concentration (in excess of  $300 \mu\text{g kg}^{-1}$ ) is seen in the southern part of the Arabian Peninsula, over Somalia, Nubian Desert in Sudan, Sistan region in Iran and central Asia, the Rigestan and Margo Desert in southern Afghanistan and the Thar Desert in the Indo-Pakistan border. Dust concentration varies between  $60\text{--}100 \mu\text{g kg}^{-1}$  over Iran and Iraq. As a comparison, it was seen over Iran that mean concentration of PM10 and PM2.5 over Iran during the summer time was about  $250 \mu\text{g kg}^{-1}$  and  $58 \mu\text{g kg}^{-1}$  respectively [Shahsavani *et al.*, 2012]. Over the AS, the dust concentration ranges between  $80 \mu\text{g kg}^{-1}$  in the west to less than  $15 \mu\text{g kg}^{-1}$  in the southeast.

At the lowest level of the atmosphere, that is at 999 mb, maximum dust flux takes place by the Findlater Jet from Somalia towards a northeast direction transporting dust into Yemen and Oman. Dust is then circulated towards northwest into the Arabian Peninsula along with dust generated from Oman. A large quantity of dust is transported from the southeastern tip of the Arabian Peninsula towards the Gulf of Aden, but the presence of the Findlater Jet [Findlater, 1969] restricts this dust to the western part of the Arabian Sea. At surface level the presence of this Jet prevents the entry of dust from the Middle East into the AS leading to very little dust over the AS. This was also seen by the *in situ* measurements by Tindale and Pease [1999]. Dust from the Nubian Desert is transported in an eastward direction through the gaps in the highland that border both sides of the Red Sea. Dust from central Asia and the Sistan Basin is transported

towards the south through the gaps in the mountains. However, the spreading of the dust over the AS is blocked by the cold SWM wind system. Within the deserts in the southern part of Afghanistan, dust is circulated in an anticlockwise direction by the prevailing wind. Similarly, over the Thar Desert, an anticlockwise trajectory emerges with dust transport to the northeast in the south and towards the AS in the north.

Above the Findlater Jet, at 797 mb pressure level, dust from the Arabian Peninsula shrouds the atmosphere over the southern and central AS. The axis of maximum west to east dust flux is around 15°N latitude. Over the northern Arabian Peninsula, the anticyclonic wind is prominent. Air mass blowing outward from this Arabian high pressure primarily carries dust. Northwesterly wind transport dust over the Red Sea that meet the northeasterly wind blowing out from the Arabian Peninsula giving rise to high dust concentration over the southern part of the Red Sea and the Gulf of Aden. Over the AS, north of 20°N, dust is transported from southwest and central Asia. At 652 mb pressure level, the direction of dust-flux becomes more north-south oriented. The dust fluxes from southwest and central Asia are towards southwest. Those from the Arabian Peninsula are towards the southeast, but take on an eastward route east of 60°E. Dust from the southern Arabian Peninsula travels over the Findlater Jet to reach Somalia. At this level dust is transported from the Arabian Peninsula across the Red Sea into the African continent. Dust from the Thar Desert is transported into the AS, while dust from central Asia transported over northern India and into Tibet.

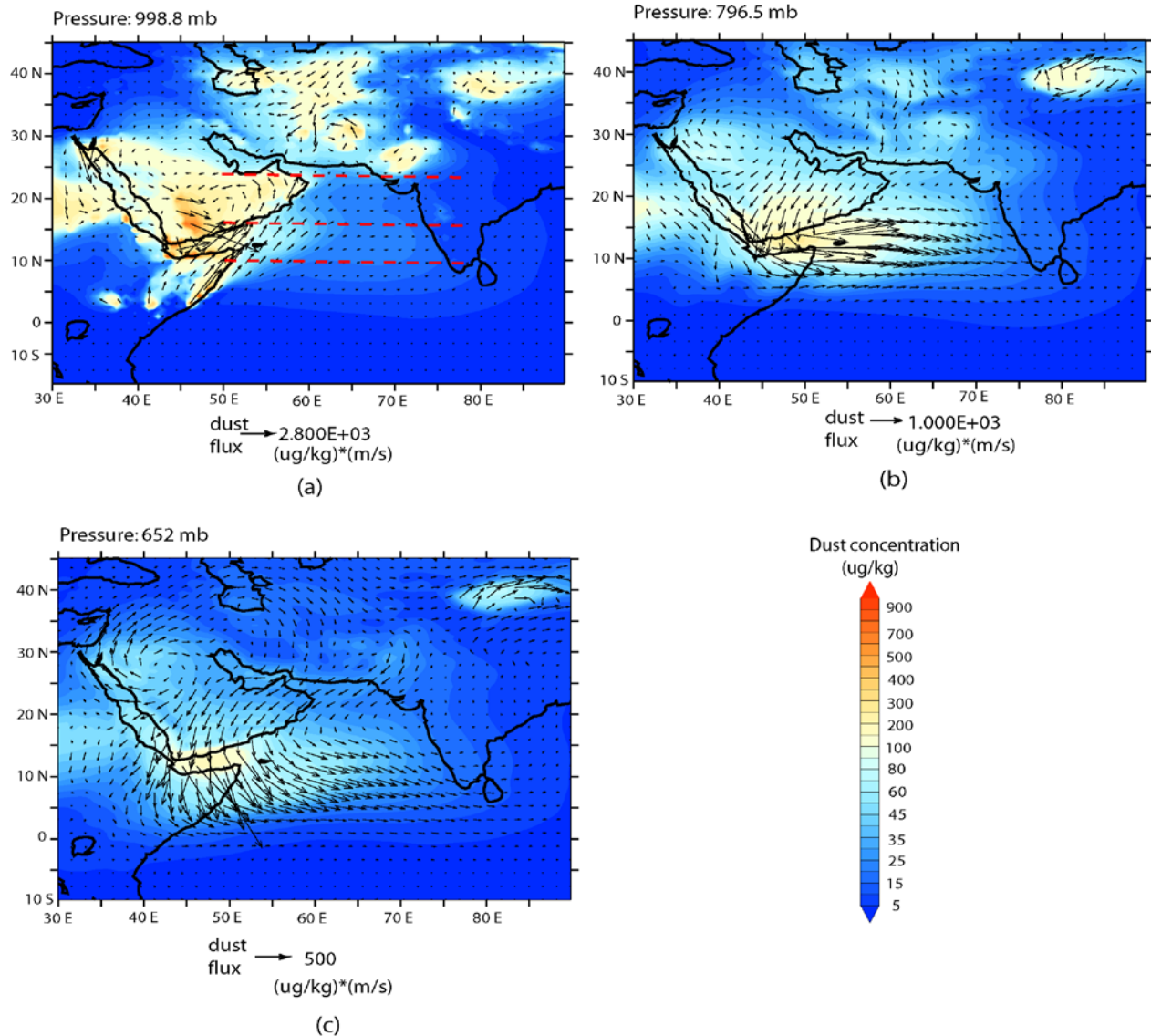


**Figure 5.7** Dust concentrations (shadings) and the dust mass flux vectors ( $\mu\text{g kg}^{-1} \text{m s}^{-1}$ ) over the Arabian Sea during the southwest monsoon season for the different pressure levels at which maximum dust transport takes place. The red dashed lines in (a) indicate the sections along which dust concentration is depicted in Figure 5.8.

Thus, it is clear from the above discussions that the dust transport routes vary greatly over the AS within small vertical distances with the dust transport from the Arabian Peninsula and the Asian landmass being undercut by the pristine marine airmass. The airmasses blowing out from the

high pressure systems situated over the Arabian Peninsula and the Caspian Sea are the main carriers of dust over the AS.

The vertical variation of dust concentration over the AS due to the seasonally varying monsoonal wind system is examined by looking at the longitude-height section of dust in Figure 5.8. These sections are constructed along 10°N, 16°N and 24°N latitudes as indicated by the dashed lines in Figure 5.7a. As expected, dust concentration is much higher during the SWM (exceeding 200  $\mu\text{g kg}^{-1}$  in the western AS) compared to the NEM (about 50  $\mu\text{g kg}^{-1}$ ). Another fact that becomes prominent is that the height of maximum dust transport across the AS is much shallower during the NEM compared to the SWM. Apart from the factors explained in the previous paragraphs, this is also related to the subsidence during the NEM period [example *Krishnamurti et al.*, 1998]. The height of maximum dust transport over the AS during the NEM is around 900 mb and shows little variation from north to south. Over India, the height of dust layer increases to about 800 mb. Over the northern AS (section along 24°N latitude) the dust concentration is higher and the height of maximum dust concentration over the AS is slightly shallower compared to the southern AS. Overall, at all latitudes, there is predominance of fine mode dust (particle size less than 2.5  $\mu\text{m}$ ) during the NEM. In the northern AS, the contribution of the coarse fraction somewhat increases due to greater proximity to the dust sources: one in the west over the Arabian Peninsula and the second in the east over the Thar Desert.

On contrary to the NEM period, during the SWM, there is a wide gradient in the height of maximum dust transport over the AS. At 10°N latitude, a tongue of high dust concentration (in excess of 300  $\mu\text{g kg}^{-1}$ ) with almost complete predominance of fine mode particles juts out at 700 mb pressure level. While at 50°E, the height of highest dust concentration touches the surface level, it gradually dislodges itself from the ground to about 750 mb pressure level east of 65°E.

This essentially reflects the undercutting of the dusty airmass by the moist SWM wind system so that the vertical variation of particle size from the surface varies from fine to coarse to again fine.

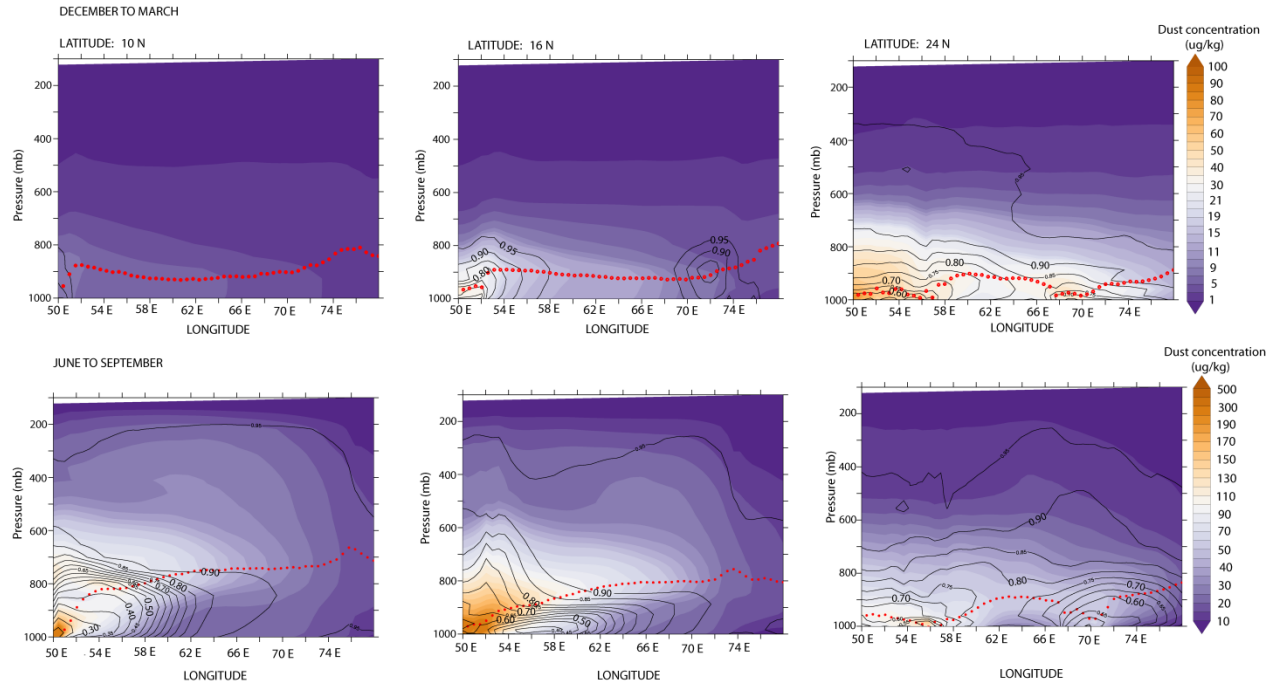


**Figure 5.8** The longitude-height variation of dust concentrations over the Arabian Sea during the northeast monsoon (top panel) and the southwest monsoon (bottom panel) period for 10°N (left), 16°N (centre) and 24°N (right) latitudes as marked by the red dashed lines in Figure 5.7a. The shading shows dust concentration, the contours are the fraction of dust that have diameter lesser than 2.5  $\mu\text{m}$  and the red dots mark the height at which maximum dust is concentrated.

At 16°N latitude, the height of maximum dust concentration (more than 500  $\mu\text{g kg}^{-1}$ ) is at 800 mb pressure level with the plane of this height of maxima sloping upward from west to east. At the surface level, the coarsest fraction of dust is concentrated at 56°E longitude. This indicates the dust transported from Somalia by the Findlater Jet. At 50°E longitude there is a secondary region of high concentration of coarse dust which is the contribution from the Arabian Peninsula. At 24°N latitude maximum dust is transported across the AS at 900 mb pressure level with dust concentrations varying between 50 to 150  $\mu\text{g kg}^{-1}$ . This dusty layer touches surface at 56°E and 70°E longitude over the dust sources. Overall, it appears that during the SWM over the southern

AS, dust travels at higher levels in the atmosphere due to the concentrated energy of the Findlater Jet which prevents dust from northeast Africa and Arabia from entering into the AS. The core of the dust layer slopes towards the surface as the energy of the Findlater Jet weakens over the northern AS.

On considering the magnitude of the dust flux during the SWM season over the AS, it is seen that maximum dust flux takes place at 14°N at 800 mb pressure level. This is shown in Figure 5.9a where the magnitude of dust flux (in  $\mu\text{g kg}^{-1} \text{ m s}^{-1}$ ) is shown along 64°E. However, the dust within this core is primarily fine mode with the coarser dust particles travelling much close to the surface. At around 200 mb pressure level a secondary region of high dust flux emerges. This 200 mb pressure levels roughly corresponds to about 11.8 km altitude level, that is, nearly the top of the tropical troposphere. This dust flux at 200 mb is related to the easterly return flow of the monsoon wind system. This is shown by the wind vectors at 267 mb pressure level in Figure 5.9b. Thus, the dust being transported to the Indian Subcontinent from the Middle Eastern deserts between 800 to 700 mb pressure levels is being re-circulated back at about 200 mb pressure level. This takes place in the southern branch of the upper-level anticyclone which is an integral part of the Indian summer monsoon. At this level, the dust can be transported by the easterlies over the Arabian Peninsula and into the African continent. Here, the monsoon system of wind acts like a chimney which sucks in the dust at lower levels of the atmosphere and pumps out the same at the top of the troposphere. Vertically, this results in a layer of clean airmass being sandwiched between two layers of high dust flux.

This double peaks in dust transport in the atmosphere over the AS is a product of the monsoon pump, which is evident from the temporal evolution of the magnitude of dust flux over the

central AS (represented as 64-66°E longitude, 14-16°N latitude as shown in Figure 5.9b) depicted in Figure 5.9c.

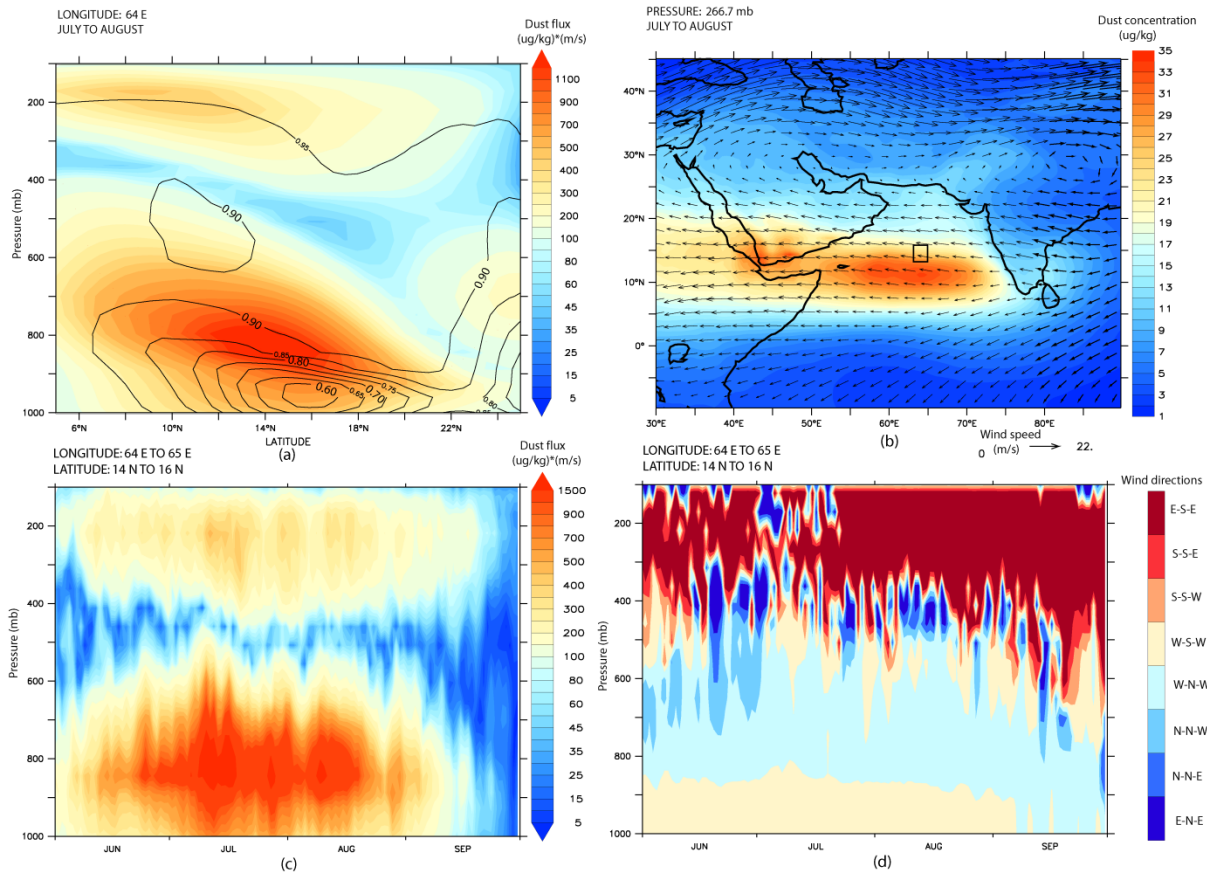


**Figure 5.9** Magnitude of dust mass flux over the Arabian Sea during the southwest monsoon period. (a) Shading shows the latitude-height variation in the magnitude of dust mass flux along 64°E longitude and the contours show the contribution of the fraction of dust that have diameter less than  $2.5 \mu\text{m}$ . (b) Shading shows the concentration of dust at 267 mb pressure level and the vectors are the wind direction. (c) Time versus height evolution of dust mass flux and (d) the corresponding wind directions within the box marked out in (b).

The evolution of the region of secondary dust flux at 200 mb pressure level mirrors the evolution of the dust flux at 800 mb pressure level. The maximum magnitude of this flux is during July-August at the peak of the SWM season and subsides gradually during the month of August. The vertical variation of wind direction (Figure 5.9d) also reflects the action of the monsoon wind

system in forming this structure of dust mass flux: southwest in the surface layer, turning aloft to westerly and northerly and finally easterly between 350 to 100 mb pressure levels. It has been recently seen by several studies that the ascending branch of the Asian monsoon is very efficient in transporting aerosols and pollutants into the upper Troposphere and the Stratosphere [example *Randel et al.*, 2010; *Vernier et al.*, 2011]. Through this pathway Asian dust can enter the upper atmosphere, be transported far away from the source and significantly affect the climate for much longer time period over a much larger region.

The principal routes through which dust is transported during the different times of the years are indicated schematically in Figure 5.10.

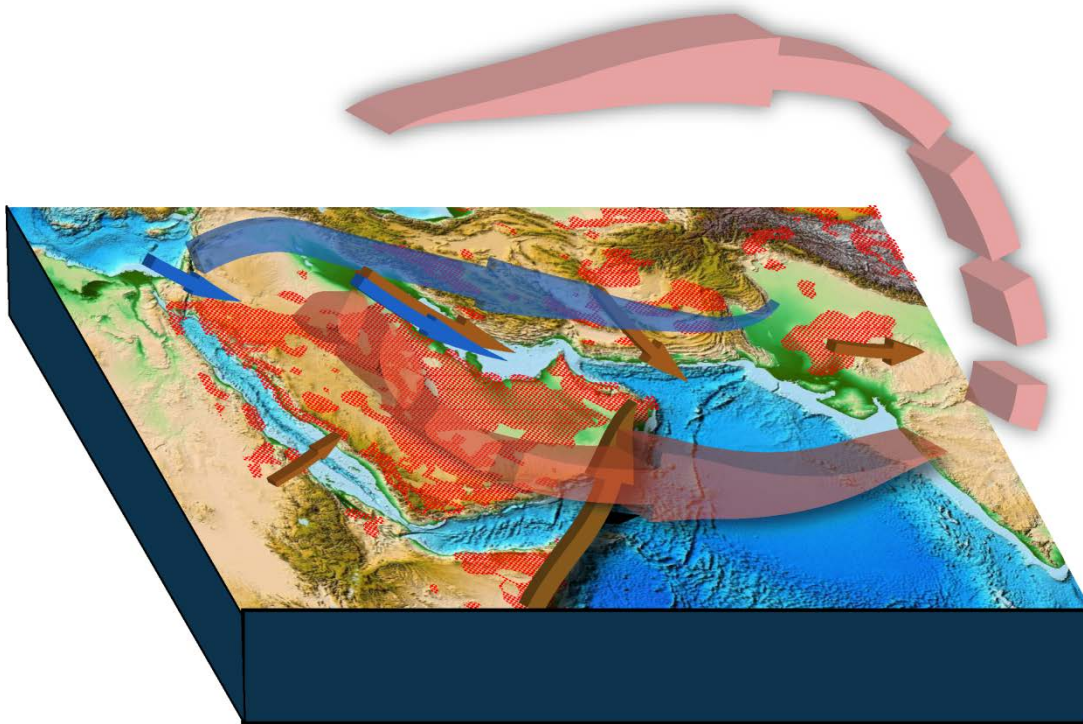


**Figure 5.10** Schematic representation of the different routes through which dust is transported over the Arabian Sea. The base map indicates the topography of the region generated from ETOPO-01. The red stippling indicates the regions where average dust emission exceeds  $1000 \text{ mg m}^{-2} \text{ day}^{-1}$ . The warm colour indicates dust transport routes during the southwest monsoon period and the cold colour indicates dust transport routes during the northeast monsoon period.

### 5.3. Dust deposition

The seasonal variation in dust deposition is shown in Figure 5.11. Dust deposition follows the same seasonal cycle as dust emission with the highest deposition over the western AS during the SWM period. The regions of dust emission are also the regions of highest deposition with almost the entire deposition being dry in nature. Over the AS, dust depositions vary between less than  $10 \text{ mg m}^{-2} \text{ day}^{-1}$  to more than  $200 \text{ mg m}^{-2} \text{ day}^{-1}$ . Comparing this value of deposition with other global model results, it is seen that dust deposition varies between  $14 \text{ mg m}^{-2} \text{ day}^{-1}$  to about  $137 \text{ mg m}^{-2} \text{ day}^{-1}$  [Ginoux *et al.*, 2001] and  $17 \text{ mg m}^{-2} \text{ day}^{-1}$  to about  $173 \text{ mg m}^{-2} \text{ day}^{-1}$  [Zender *et al.*, 2003]. Deposition reduces exponentially in magnitude towards the southeastern AS. With the decrease in the concentration of dust, wet deposition gains importance. Wet deposition is also related to the magnitude and timing of the precipitation over a particular region (see Figure 5.12). During the NEM, high contribution of wet deposition is seen over (1) the eastern shores of the Mediterranean along the storm track and (2) south of  $15^{\circ}\text{N}$  latitude over the AS. As the ITCZ is approached, 80% of deposition takes place in the wet form. With the transition of the year into SIM, the region of wet deposition over the Mediterranean is reduced, while maximum wet deposition is seen between the Equator and  $10^{\circ}\text{S}$ . With the advent of the SWM, maximum wet deposition takes place along the west coast of India under the mechanical effect of orography of the Western Ghats. Table 5.2 lists the total amount of dust deposited in the AS during different seasons and the contribution of wet deposition.

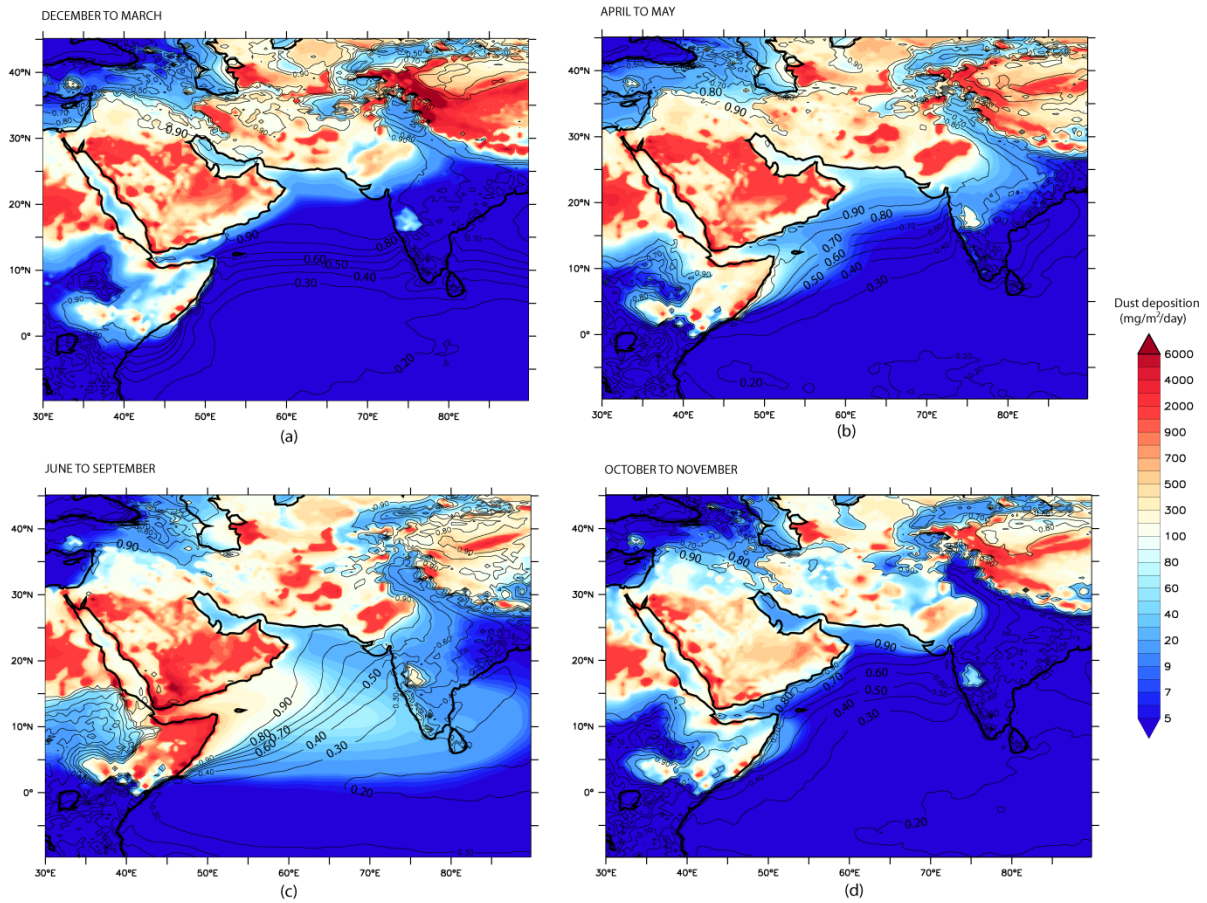


**Figure 5.11** Seasonal cycle of dust depositions (blue-red shading) over the Arabian Sea and surroundings for (a) northeast monsoon (b) spring intermonsoon (c) southwest monsoon and (d) fall intermonsoon. The contours mark the contribution of dry deposition to total deposition.

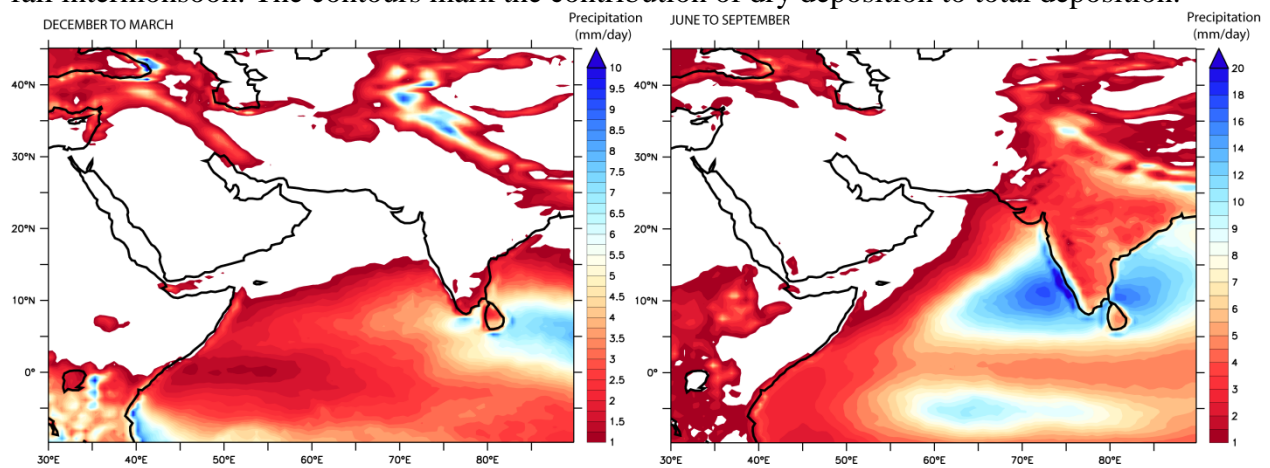


**Figure 5.12** Distribution of precipitation over the Arabian Sea and surroundings during the northeast monsoon (left) and southwest monsoon (right).

**Table 5.2** Dust depositions into the Arabian Sea (5-25°N latitude, 50-78°E longitude) during different seasons

Season	Total depositions* (mg m <sup>-2</sup> day <sup>-1</sup> )	Contribution to total depositions (%)	Wet depositions (%)
NEM	8.0	6.8	6.25
SIM	24.5	10.4	15.51
SWM	93.1	79.2	15.90
FIM	8.4	3.6	17.86

\* Note that land has been masked out and most of the emitted dusts are deposited very near to the dust sources.

#### 5.4. Summary

To sum up, certain salient features of the dust cycle over the AS have been revealed by the RegCM4 model. These features can be summarized as under:

- 1) Overall, 47% of dust emissions from the dust source regions surrounding the AS and 79% of dust depositions into the AS takes place during the SWM season. The importance of wet deposition increases with increasing distance from the dust sources.
- 2) Maximum dust emission is associated with the summertime heating of the Asian landmass and high wind speed. During the winter time, passage of cold fronts from the Mediterranean region is important in dust mobilization.
- 3) During the SWM period, the ITCZ divides the dust sources surrounding the AS into two distinct regions: (1) to the east and south of the ITCZ, dust emission is accomplished by the SWM wind system and it depends on the strength of the monsoon winds (2) to the

north and west of the ITCZ, dust emission is accomplished by the northwesterly and northerly wind system and it depends on the surrounding high pressure regions.

- 4) Within the region influenced by the SWM wind system, dust is blown off from the northeast Horn of Africa by the Findlater Jet at the lower levels. However, the jet restricts dust to the western part of the AS. Dust from the Middle East and southwest Asia (that originates from the west and the north of the ITCZ) meets the SWM wind along the ITCZ and overrides the monsoon wind system. The confluence zone of these two wind systems, lying on both sides of the ITCZ, follows an inclined plane in the vertical. The plane touches the surface in the north and west and rises to higher pressure level in the south and eastern AS.
- 5) Dust from the southwest Asia and Middle East is re-circulated westwards at the top of the Troposphere by the easterly wind that develops during the SWM season. This is accomplished by the southern branch of the upper level anticyclone of the monsoon system. This can potentially transport dust long distances and influence the climate of places far removed from the dust sources.

## CHAPTER 6

# INFLUENCE OF CLIMATE MODES ON DUST OVER THE ARABIAN SEA

### 6.1 Influence of ENSO

The understanding of what controls the interannual variability of dust over the AS has been a research problem that has not been addressed adequately. For example, it has been seen for the Atlantic Ocean region that the different climate modes like ENSO [*Prospero and Lamb, 2003*] and the North Atlantic Oscillation [*Moulin et al., 1997*] exert a significant influence on dust generation in the Sahara-Sahel region and its transport routes. However, no such clear consensus has been arrived at for the north IO. The emergence of such an understanding is crucial in order to relate how dust aerosols affect the different aspects of climate over the AS. This chapter deals with the possible control that different climate modes might exert on the interannual variability of dust generation and its subsequent transport over the AS.

Two most important climate modes that have the potential to impact the northern IO are ENSO [*Trenberth, 1997; Kumar et al., 2006*] and the IOD [*Saji et al., 1999*]. While ENSO has its origin in the tropical Pacific Ocean, IOD is an equivalent of ENSO in the tropical IO. Most often, it has been seen that ENSO and IOD work hand in hand, each complimenting the effect of the other [*Meyers et al., 2007*]. For example, during the positive phase of ENSO and IOD, there is an anomalous cooling of the SST over the eastern tropical IO and western Pacific and suppression of convective activity over this region and vice versa. Also, the tropical western IO experiences

anomalous warming (cooling) during positive (negative) IOD [Saji *et al.*, 1999]. Section 6.1 tries to unravel if ENSO have the potential to significantly affect dust activity around the northwest IO. The case of IOD will be taken up in Section 6.2.

### 6.1.1. Relation between dust, precipitation and soil moisture

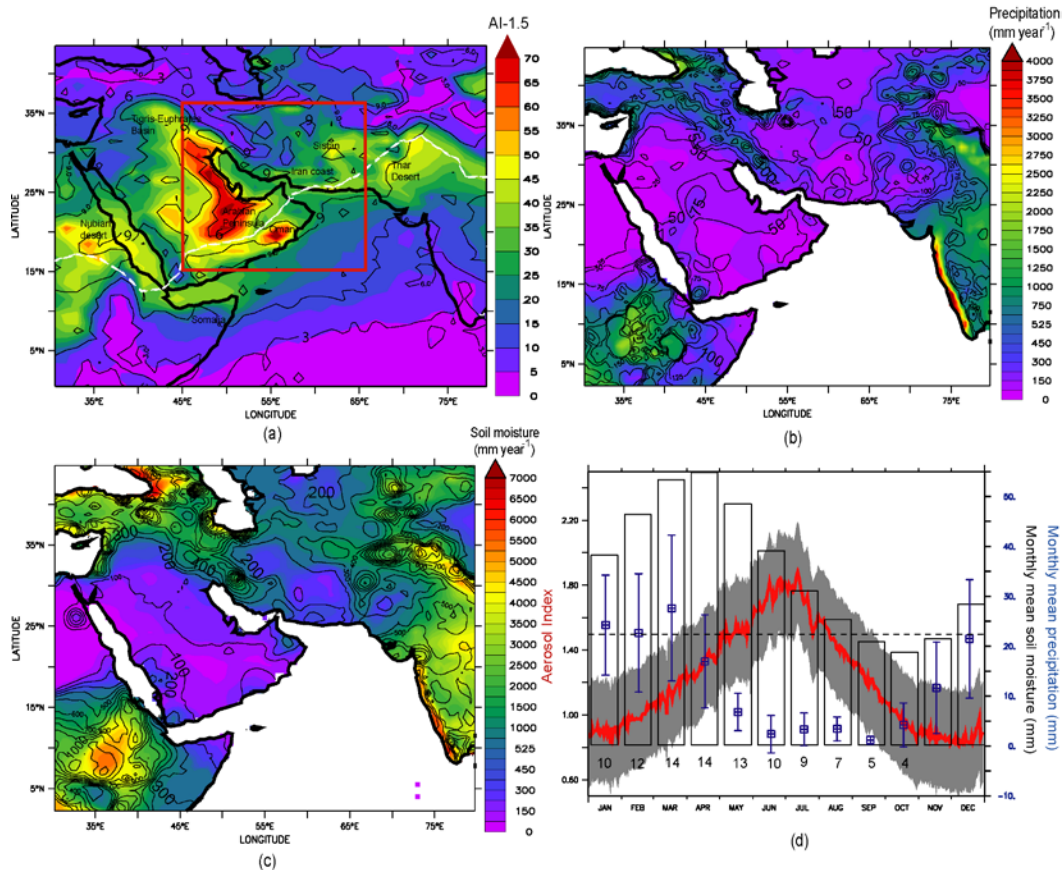


**Figure 6.1** Climatological (1979-2013) distribution of AI-1.5, precipitation and soil moisture over the Arabian Sea and the surrounding landmass. Shadings in (a), (b) and (c) show AI-1.5, precipitation and soil moisture respectively and the black contours are their standard deviations. The white dashed line in (a) shows the mean position of the ITCZ determined as the location where the northward component of the wind becomes zero during boreal summers. The red box in (a) represents the region SAME which has been taken up for further study. The temporal evolution of AI, precipitation and soil moisture over SAME is depicted in (d). Thick red curve shows the daily climatology of AI with the standard deviations of AI represented by the shaded region. The tiny blue squares indicate monthly climatology of precipitation plotted along with their error bars. The hollow black rectangles are the monthly mean climatology of the soil moisture. The numbers below the rectangles indicate the standard deviations of soil moisture.

The interannual variability of dust aerosols over the AS has been studied by using the time-series of 26 years AI-1.5 data as has been explained in Section 3.3. The climatological distribution of AI-1.5 over the study region shows 3 distinct belts of dust activity (Figure 6.1a). These are: (1) the arid region shared by the borders of northwest India, Pakistan and Afghanistan along with few pockets in Iran, (2) the Middle East dust belt stretching from the Tigris-Euphrates Basin to the southern Persian Gulf coast, into the Arabian Peninsula and up to Oman coast. This is one of the dustiest places of the globe with some regions experiencing more than 70% days with AI greater than 1.5 and (3) the Nubian Desert in Sudan funnelling dust mainly into the Red Sea. The characteristics of these regions have been discussed in Section 5.1. The high values of AI-1.5 over northern India are to a large extent the contribution from black carbon aerosols arising out of anthropogenic activities [Menon *et al.*, 2002]. Interestingly, the regions exhibiting the highest variability in AI-1.5 are located in the periphery of the regions that experience highest dust activity. The greatest standard deviation (SD, exceeding 9) is seen along a crescent-shaped track running from Syria to the Tigris-Euphrates region in Iraq and extending into the coastal part of Iran lying to the north of the Persian Gulf. While these regions have natural sources of dust from the numerous salt-lakes and river sediments, anthropogenic contribution to the dust load are also considerably important [Ginoux *et al.*, 2012]. Precipitation and soil moisture are the two most important factors dictating dust generation over a region. If the distribution of AI-1.5 is compared with the distribution of precipitation (Figure 6.1b) and soil moisture (Figure 6.1c), it is seen that the main dust regions have annual precipitation and soil moisture of less than 150 mm and 300 mm respectively. These regions also have very little variability of precipitation (SD is ~50 mm) and soil moisture (SD is ~100 mm). Precipitation and soil moisture values are considerably more in the periphery of the regions having the highest AI-1.5 and so is the

variability in these two parameters. In fact, the regions having high variability in precipitation (SD is more than 150 mm) and soil moisture (SD is more than 400 mm) have a good correspondence with the regions that have high variability in AI-1.5. For example, along the axis of the Tigris-Euphrates Basin, the values of AI-1.5 is somewhat low and the rainfall and soil moisture are comparatively high. Here the SDs of all the three parameters is high. A similar case is noticed in the southern part of the Arabian Peninsula and over Iran and parts of Afghanistan. However, along the southern coast of the Persian Gulf over the Saudi Arabian Plateau, where the highest AI-1.5 is encountered, rainfall and soil moisture are the lowest. The SDs of these parameters is also very low over this region.

The region enclosed by the red box (42-66°E longitude and 15-36°N latitude) in Figure 6.1a has been taken up as representing southwest Asia and the Middle East (SAME) to examine the seasonal cycle of AI. This box has been chosen such that it encompasses the regions that have the highest AI-1.5 values. Another consideration is that, the atmosphere over the AS is influenced greatest by the dust transported from SAME. Recall, that dust from the northeastern Africa is mostly confined to the west of the AS by the Findlater Jet (Section 5.2). Climatologically, the area averaged AI within SAME exceeds 1.5 about 26 % days in a year, mainly from the beginning of May to middle of August (see Figure 6.1d) and reaches a peak during June-July. Dust activity is lowest during November to January. The area-averaged SD of AI-1.5 within SAME is about 7. More than 60% of the rainfall is concentrated during the winter months of December to March and peaks during January (about 30 mm, Figure 6.1d). The wetness due to winter precipitation is reflected in the soil moisture as well, although, the response is delayed by a month (Figure 6.1d). The climatological monthly mean soil moisture is about 35 mm and it peaks to more than 50 mm during March -April. This is also the time when

the highest variability (SD 14 mm) of soil moisture is seen. Thus, from the spatial and temporal pattern of AI-1.5 it appears that the variability of the annual dust activity which peaks during the summer months is possibly to a large extent related to the variability of precipitation and soil moisture during the previous winter. While the entrainment of dust in the atmosphere depends on wind speed and are often associated with synoptic scale events, the threshold friction velocity required to erode the soil increases under wet conditions [Fecan *et al.*, 1999]. Therefore, the conditions that dictate precipitation during boreal winters are crucial to dust production.

### 6.1.2. Relation between AI-1.5 and ENSO

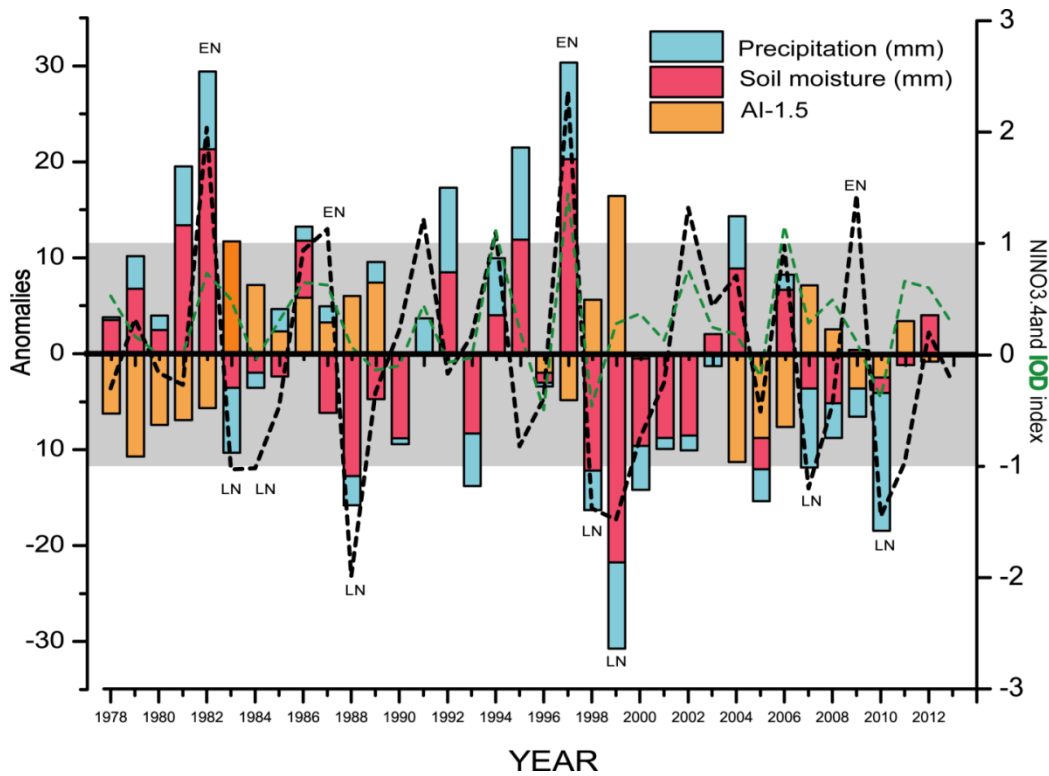


**Figure 6.2** Time-series of anomalies of AI-1.5, soil moisture and precipitation (rectangles) and NINO3.4 and IOD index (dashed lines). The NINO3.4 and IOD index of previous years are collocated with the current years' anomalies. The 4 El Niño (EN) and 7 La Niña (LN) years when AI data are available are indicated on top and the bottom of the anomaly respectively.

The anomalies of AI-1.5, soil moisture and precipitation are seen to have definite relation with NINO3.4 index within SAME (see Figure 6.2). Soil moisture and precipitation have been considered for winter time (October to May). For example, for the El Nino of 1982 (that is NINO3.4 index for OND 1982), AI-1.5 for the year 1983 and precipitation and soil moisture from October 1982 to May 1983 have been considered. It is seen that the positive anomalies of AI-1.5 are generally in tandem with negative anomalies of soil moisture and precipitation. The El Nino conditions are characterized by negative AI-1.5 anomalies and positive soil moisture and precipitation anomalies. The opposite is true for La Nina years. The correlation coefficient between NINO3.4 index and AI-1.5 of the corresponding years (example: both NINO3.4 and AI-1.5 of 1982) is -0.12 which is not significant. However, the correlation coefficient between NINO3.4 and AI-1.5 of the following years (example: NINO3.4 of 1982 and AI-1.5 of 1983) is -0.52 which is significant at 99% (see Table 6.1). The correlation coefficient between NINO3.4 and precipitation is 0.58, while that between NINO3.4 and soil moisture is 0.56. Both correlation coefficients are highly significant at 99% level. This indicates that during the El Nino years a wet anomaly prevails over the northwest rim of the IO during the boreal winters [Syed *et al.*, 2006; Mariotti, 2007], which is the principal rainy season for this region. This wet anomaly during El Nino leads to a general increase in the soil moisture content and therefore less dust emission and dust activity over the AS and surroundings during the following summer. On the contrary, dry conditions during the winters of the La Nina years are conducive to increased soil dryness and subsequent enhanced dust activity over the region. Highest positive departure of 16.43 in AI-1.5 is seen in the year 2000 following one of the most intense La Nina of the last three decades in 1999 when the NINO3.4 index was -1.48. This departure is about 50% of the long time AI-1.5 climatology within the defined region. The maximum negative departure of -11.31 is seen,

however, in the year 2005, although 2004 had comparatively low NINO3.4 index value of 0.71. A lag correlation between NINO3.4 index and annual average AI (instead of AI-1.5) yielded a correlation coefficient of -0.37, which is just below the 95% significance level.

**Table 6.1** Correlation coefficients between climate modes and AI-1.5, precipitation and soil moisture

Climate Mode	Current year AI-1.5	Following year AI-1.5	Current year AI	Following year AI	Soil Moisture (October to May)	Precipitation
NINO3.4	-0.12	<b>-0.52</b>	-0.35	-0.37	<b>0.56</b>	<b>0.58</b>
DMI	-0.02	-0.07	-0.13	0.07	0.38	0.38

Note: The numbers in bold indicate the correlation coefficients that exceed 99% significant level.

This negative correlation between ENSO and AI-1.5 has been investigated further by looking at the spatial pattern of the distribution of correlation between the two variables. It is seen in Figure 6.3a that the entire northwest IO shows negative correlation between NINO3.4 index and AI-1.5. The region of significant correlation extends from the Tigris-Euphrates basin southeastwards along the Persian Gulf into the AS. The other regions of significant correlations are: (1) northeast from Iran into Afghanistan and (2) across the central part of the Arabian Peninsula. The high correlation over the AS is obviously the result of dust transported from the surrounding arid and semi-arid regions. The spatial nature of correlation between NINO3.4 and precipitation (see Figure 6.3b) shows the main axis of positive correlation between the two is the eastern coast of Mediterranean, along the axis of the Tigris–Euphrates Basin, the southern shore of the Caspian Sea, the Dasht-e-Kavir and Dasht-e-Lut Desert in Iran and across Afghanistan-Turkmenistan border region. The correlation between NINO3.4 index and soil moisture (contours in Figure 6.3b) also reflects the similar pattern of response as precipitation. The exceptions are: (1) the

zone of significant positive correlation between NINO3.4 and soil moisture is restricted to the west of 70°E and does not touch the southern shores of the Caspian Sea, while that between precipitation and NINO3.4 extends much more eastwards and (2) some scattered pockets of positive correlations between NINO3.4 and soil moisture is seen over the Arabian Peninsula.

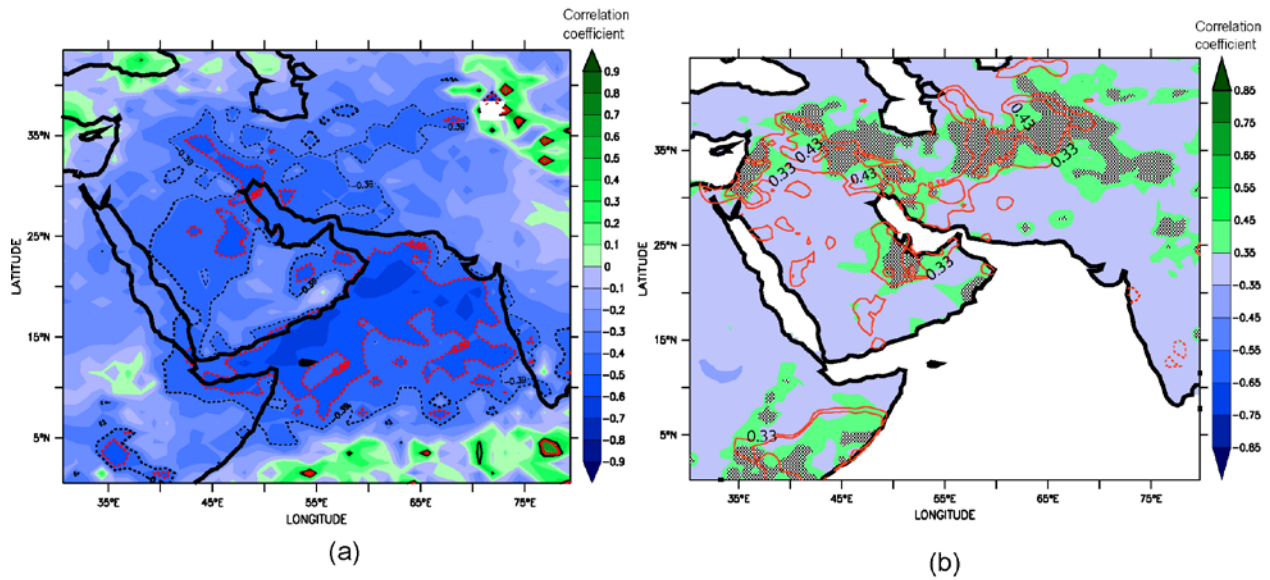


**Figure 6.3** Map showing spatial pattern of the correlation between (a) ENSO and AI-1.5 and (b) ENSO and precipitation and soil moisture. (a) Shading shows the distribution of correlations between ENSO and AI-1.5. The black and red dashed contours enclose the regions where the correlation exceeds 95% and 99% significance levels respectively. (b) Shaded map shows the correlation between NINO3.4 and precipitation from October-May. Only the regions that have correlation coefficient exceeding 95% significance level are shaded, while the stippling encloses the regions that have correlation coefficient exceeding 99% significance level. The red contours marked 0.33 and 0.43 indicate the regions that have correlation between NINO3.4 and soil moisture (October-May) exceeding 95% and 99% significance levels respectively.

Over land, the region where AI-1.5 responds negatively to El Nino lies within the zone where precipitation and soil moisture responds positively (at 95% significance level) to El Nino. This implies that the changes in precipitation modulated by ENSO have the potential to impact the dust production and transport. The region where precipitation responds significantly to ENSO is mainly affected by the low pressure system from the Mediterranean during the winter time,

which is the main source of moisture for this region [Martyn, 1992]. The exception is in the central part of the Arabian Peninsula where precipitation and soil moisture do not have significant positive correlation with ENSO, but AI-1.5 has significant negative correlation with ENSO. No significant change in air temperature over this region during the summer following an ENSO event is discerned. Trajectory analysis has shown that most of the dusts over the central part of the Arabian Peninsula are either transported from the Iraqi dust sources or from Rub Al Khali with June as the time of highest transport [Notaro *et al.*, 2013]. So the high negative correlation between NINO3.4 and AI-1.5 in the central part of the Arabian Peninsula may possibly indicate transported dust. The other region of exception is in northeast Oman where, although AI-1.5 shows significant negative response, winter precipitation (and soil moisture) does not have any apparent significant relation with ENSO.

### **6.1.3. How ENSO modulates interannual variability of AI-1.5?**

The warm and cold phases of ENSO have been known to influence the meteorological conditions over the IO and the surrounding regions manifold. For example, the negative impact of El Nino on the Indian summer monsoon has been the focus of several studies in the past [example Ropelewski and Halpert, 1987; Torrence and Webster, 1999; Kumar *et al.*, 2006]. Wet conditions over the Middle East and central Asia have been related to El Nino [Nazemosadat and Ghasemi, 2004; Mariotti *et al.*, 2005; Mariotti, 2007], while intense La Nina conditions have been associated with the prevalence of severe droughts [Barlow *et al.*, 2002; Hoell *et al.*, 2014].

The linkage between dust conditions over the northwest IO and the phase and amplitude of ENSO is largely unknown. One of the potential candidates for such a link could be the modification to the strength of convection over the Indo-Pacific warm pool (IPWP) region. The

climatological SST for the period September to March over the eastern tropical IO (taken as 0-10°S, 90-110°E) is about 28.47°C. During the warm (cold) phase of ENSO, when the NINO3.4 index exceeds 1 (less than -1), the SST anomaly can be about -0.50°C (0.50°C). Such a persistent SST anomaly over IPWP during the boreal winters leads to modification of the atmospheric conditions over the region. This has far-reaching influence on the meteorology over the northern IO and its surroundings. This is depicted in Figure 6.4, which shows the differences in the atmospheric circulations and the resulting atmospheric moisture content anomaly between the El Nino (a and b) and La Nina (c and d) years. Figure 6.4 has been constructed for the months of December to March when SAME receives maximum precipitation. A near see-saw pattern of meteorological conditions is evident between IPWP and SAME when the different phases of ENSO are considered. During the El Nino years the vertically integrated moisture flux is away from IPWP leading to a negative anomaly of specific humidity (Figure 6.4a). This is due to suppression of convective activity over IPWP as indicated by positive OLR anomaly (Figure 6.4b). Such a scenario is triggered by an anomalous descent over IPWP (Figure 6.4b) during the boreal winters due to El Nino-induced cooling of the SST. This is concomitant with a negative OLR anomaly (increased convection), positive specific humidity anomaly and an anomalous moisture flux towards the entire tropical IO. As is seen in Figure 6.4b, an anomalous ascent develops over SAME and the tropical IO. However, the association between El Nino and moisture flux over SAME is not very prominent.

The La Nina years, on the contrary, are associated with vertically integrated moisture flux towards IPWP and away from SAME (Figure 6.4c). The effect of such a moisture flux on the anomaly of vertically integrated specific humidity over the entire region is much more dramatic during La Nina years compared to El Nino years. This is indicated by the deficits (excess) of 300

$\text{g kg}^{-1}$  seen over SAME (IPWP), which accounts for ~17% of the vertically integrated specific humidity during normal years. This is also supported by negative OLR anomaly over IPWP extending into the central IO and a positive OLR anomaly (decreased convection) over SAME (Figure 6.4d). This situation results from an anomalous ascent over IPWP, which is in concert with an anomalous descent over SAME extending into northern India (Figure 6.4d). An anomalous anti-cyclonic circulation develops during the La Nina years (Figure 6.4d) strengthening the already persistent Arabian high pressure cell. This can dampen the effect of migration of moisture-laden low pressure systems as a part of the western disturbance. This entire set-up leads to the observed patterns of precipitation anomaly in winter. The memory of the precipitation is retained in the moisture content of the soil during the following summer. The moisture content of the soil ultimately has bearing on the dust emission and dust load over the northwest IO.

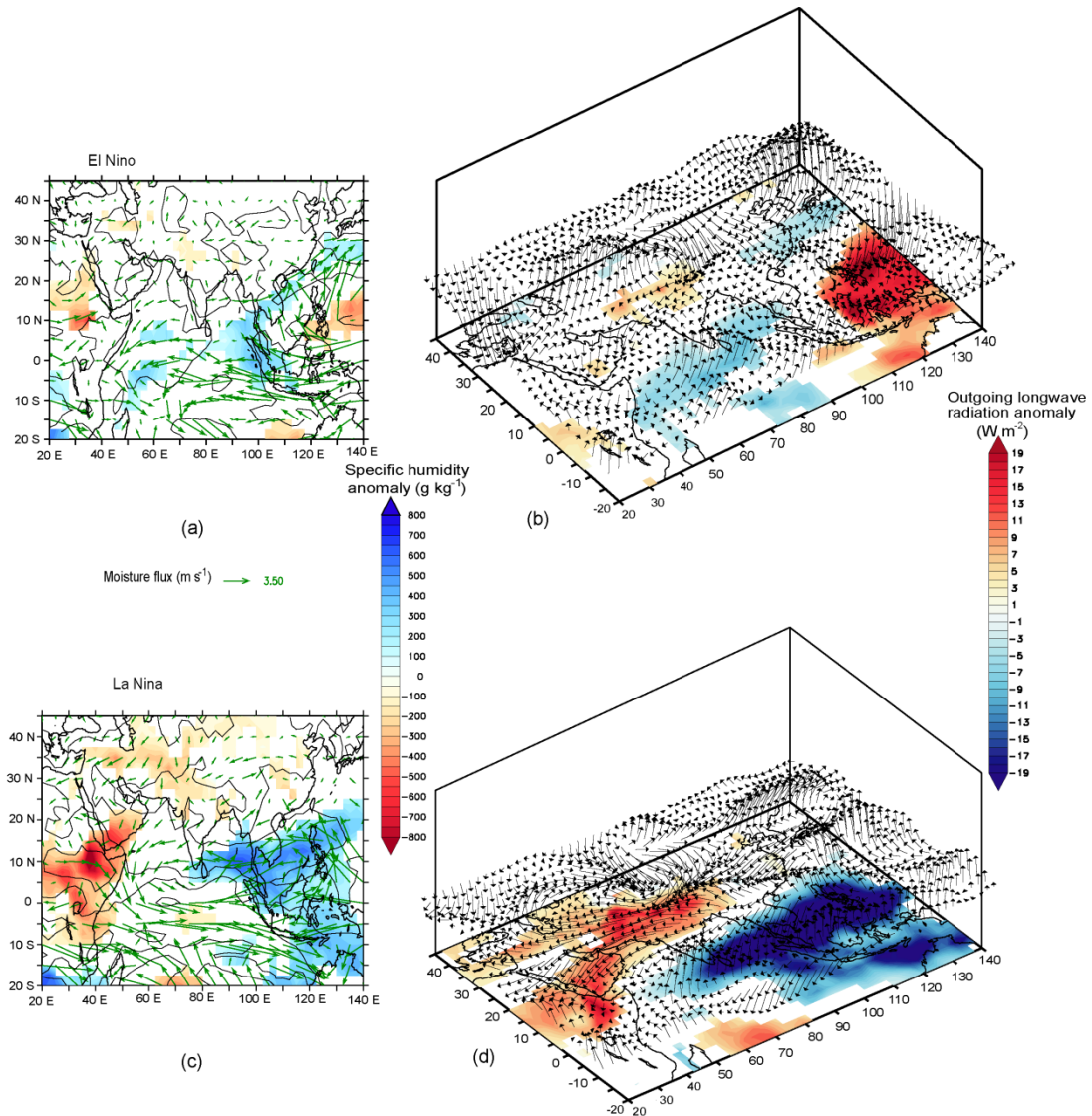


**Figure 6.4** Comparison of anomalies of vertically integrated specific humidity, moisture flux (a and c), OLR and wind vectors (b and d) during December to March of El Niño (a and b) years and La Niña (c and d) years. Anomalous conditions during El Niño (La Niña) years are obtained by differencing the meteorological fields during the years when NINO3.4 index exceeded value of 1.0 (less than -1.0) from the years when NINO3.4 index was between -1 and +1. The blue (red) shades in (a) and (c) indicate positive (negative) vertically integrated specific humidity anomaly (expressed as g kg<sup>-1</sup>) and the vectors are the vertically integrated moisture flux anomaly (expressed as kg kg<sup>-1</sup>\* m s<sup>-1</sup>). The shading in (b) and (d) show the anomaly in OLR. The vectors are the wind anomaly (horizontal and vertical) at 300 mb pressure level. The vertical component of wind anomaly has been multiplied by 10. For specific humidity and OLR, anomalies at 95% significance levels are shown. The black contours enclose the regions where the magnitude of vertically integrated moisture flux anomaly exceeds 95% significance level.

Such observed enhanced subsidence leading to suppression of precipitation (and consequently dust production) over SAME is consistent with the mechanism of monsoon-induced subtropical desert formation proposed by *Rodwell and Hoskins* [1996]. This is also supported by the model experiment of *Barlow et al.*, [2007]. The basis of this mechanism is intense convection over IPWP can lead to generation of warm Rossby-like wave packets that propagate towards the west. Upon interacting with the mean westerly flow over SAME during the boreal winters, the air parcel cools which thermodynamically forces a descent over the region. This stabilizes the atmosphere thereby reducing the propensity to precipitate. Thus, ENSO modulation of the strength of convection over IPWP can, in turn, remotely control dust activity over SAME. Higher than normal SST and strong convection over IPWP during La Nina leads to suppression of precipitation and more dust emission over the northwest IO. Opposite conditions prevails during El Nino.

The delayed effect of an ENSO event persists during the boreal spring and summer of the following year. During the year following an El Nino event, there is widespread warming over the tropical northern IO making the IO warm pool water much more prominent [*Xie et al.*, 2002; *Du et al.*, 2009; *Schott et al.*, 2009] and the extent and intensity of AS upwelling is much reduced [*Izumo et al.*, 2008]. This is accompanied by increased rainfall over the eastern AS since the increased SST is conducive towards evaporation and moisture flux to the west coast of India [example *Izumo et al.*, 2008]. The increased rainfall leads to a Matsuno-Gill pattern in the upper levels of the troposphere [*Kumar and Hoerling*, 2003; *Yang et al.*, 2007]. On the other hand, following a La Nina year, there is a basin-wide cooling with a decrease in rainfall which affects its feedback to the atmospheric circulation.

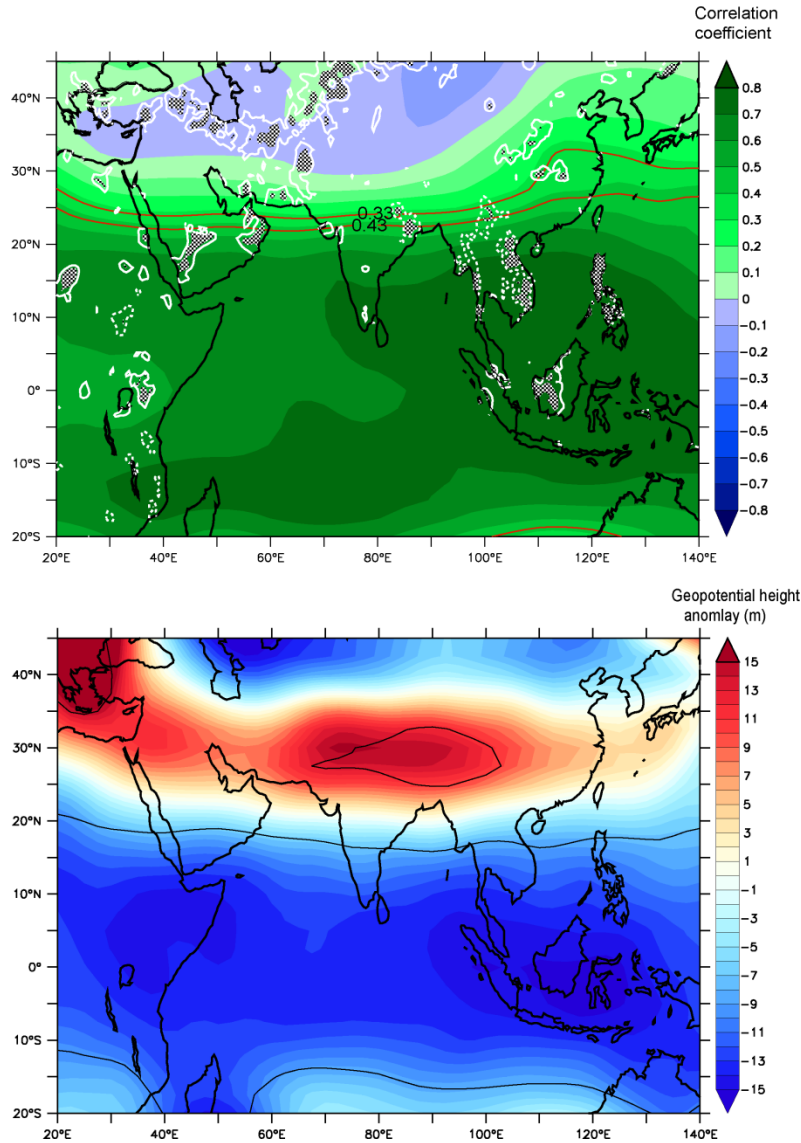


**Figure 6.5** Relation between ENSO, AI-1.5 and geopotential height during the summer following an ENSO. (a) Shading shows correlation between NINO3.4 index and geopotential height at 300 mb for April to August of the following year. The regions exceeding 95% and 99% significance levels are shown by red contours marked as 0.33 and 0.43 respectively. The white contours enclose the regions where correlation between NINO3.4 and precipitation for April to August exceeds 95% significance level. Continuous contours are for positive and dashed contours are for negative correlations. The stippling indicates the regions where correlation between NINO3.4 and precipitation exceeds 99% significance level. (b) Difference in geopotential height at 300 mb pressure level between years having positive AI-1.5 anomaly and negative AI-1.5 anomaly. Red (blue) shades show the regions of positive (negative) anomaly. The contours enclose the regions having anomaly greater than 95% significance level.

This is depicted in Figure 6.5a which shows the correlation between NINO3.4 index for OND and the geopotential height at 300 mb pressure level for April to August (the time when maximum dust is transported across the AS) of the following year. A highly significant positive correlation is seen between NINO3.4 and geopotential height throughout the entire tropical band. This implies that during the summer following an El Nino (La Nina) year, there is increase (decrease) in geopotential height over the Indo-Iranian region. Such a set-up following El Nino is not favourable towards the development of the circulation that leads to dust transport. This is further evident when one considers the difference in geopotential height at 300 mb pressure level between the years that have positive AI-1.5 anomaly and the years that have negative AI-1.5 anomaly (see Figure 6.5b). A significant lowering of the geopotential height, nearly parallel to the 20°N latitude, was discernible during the years having positive AI-1.5 anomaly. Although not as prominent, a significant increase in geopotential height in the north (over Tibetan region) and northwest (southeast Europe) is also seen. This provides the required north-south and northwest-southeast gradient for dust transport to take place. The pattern of geopotential height anomaly in Figure 6.5b closely follows the pattern of correlation between geopotential height and NINO3.4 index in Figure 6.5a. This may also explain the region of negative correlation in Figure 6.3a between NINO3.4 and AI-1.5 in northeast Oman since the dust activity there is principally related to the monsoon circulation [Ackerman and Cox, 1989] (also discussed in Section 5.1). It has been seen that the increase in gradient in geopotential height between the Caspian Sea and Indo-Iranian region intensifies the *Levar* winds that are important for dust storms in the Sistan region of Iran [Kaskaoutis et al., 2014] (see Section 5.1). This type of situation favourable for dust activity develops during the summer following a La Nina year as is seen by the correlation between the geopotential height and the NINO3.4 index. The low rainfall following a La Nina

event will also result in the persistence of this dust-laden layer. The difference in AI-1.5 between La Nina years and normal years is shown in Figure 6.6.

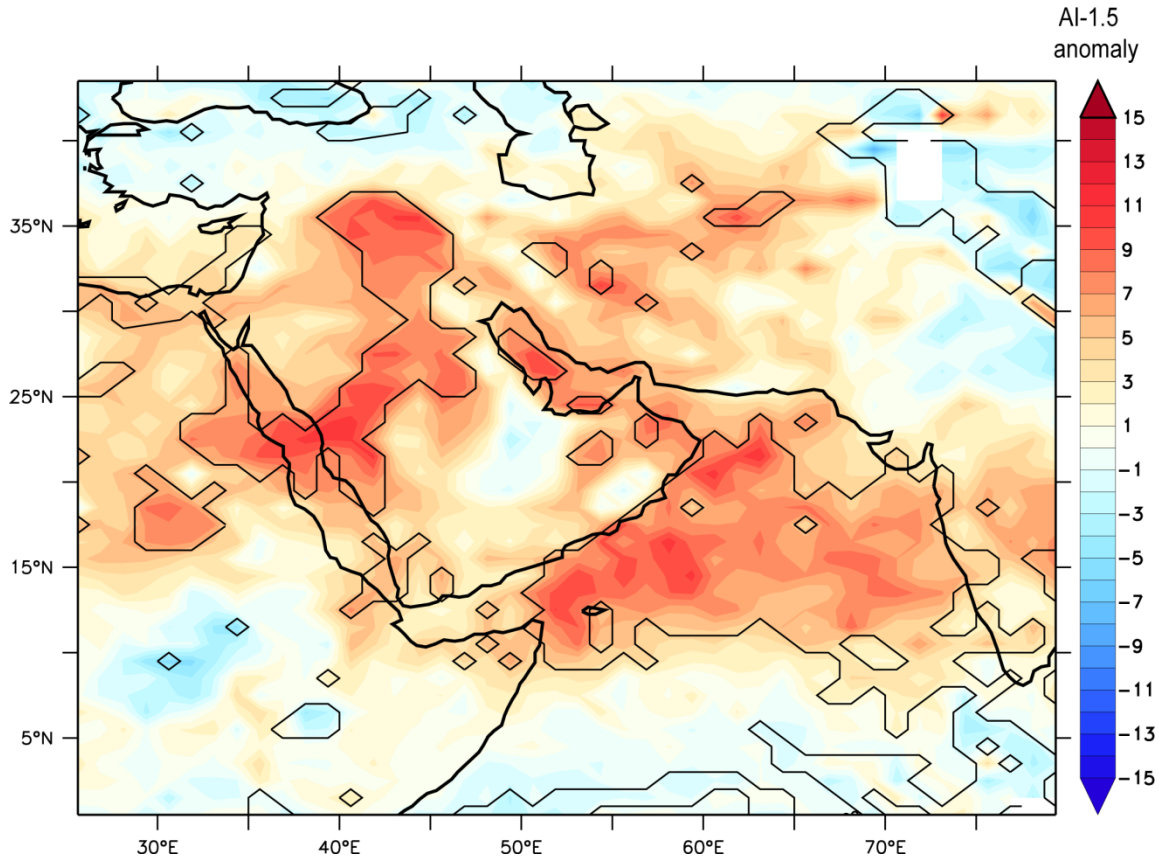


**Figure 6.6** Anomaly of AI-1.5 during the years following La Nina. The contours enclose the regions that have anomaly significant at 95%.

## 6.2. Influence of IOD

Though the correlation coefficient between DMI and AI-1.5 of the following years is of the same sign as that between ENSO and AI-1.5, the value is very small (-0.07) and is not significant. This leads to the conclusion that while the coupled air-sea interactions prevailing over the tropical IO drives the precipitation anomaly that in turn controls the strength of the dust cycle over the northwest IO, the prime driver of the interannual variability of dustiness over this region is the

phase and amplitude of ENSO. Table 6.1 summarizes the correlations between ENSO and IOD and the levels of dust activity along with the factors that dictate dust generation. The partial correlation between AI-1.5 and IOD adjusted for ENSO is 0.36 which is less than 95% significant level, while the partial correlation between AI-1.5 and ENSO adjusted for the effect of IOD is -0.60 which is significant at 99% level. This explains about 36% of the variability of AI-1.5. Thus, ENSO proves to be a prime driver of the interannual variability of dust activity over the northwest IO impacting the atmospheric composition over this region crucially. It has been proposed that the effect of the IO SST on precipitation over SAME and the surroundings is opposing the effect of the Pacific SST [Mariotti, 2007]. Positive phase of IOD is characterized by increased convection and moisture convergence near the tropical western IO (Figure 6.7a). This leads to moisture flux out of the Arabian Peninsula. However, since most of the positive IOD years are also El Nino years, convection is also prevalent over SAME during previous winters. So, while El Nino years act to increase precipitation and reduce dust, the coincidence of IOD with El Nino will tend to offset this effect. This is probably one reason why the region of significant anomaly in specific humidity and OLR during El Nino time (Figure 6.4a and 6.4b respectively) is not much over SAME but over the tropical IO. However, such is not seen in the case of La Nina. This might be due to the fact that negative IODs are much weaker in magnitude (maximum is -0.49 during 1996) compared to positive IOD (maximum is 1.44 during 1997). Also, during the study period, negative IODs occurred much less than positive IODs. This also explains why the maximum negative departure in AI-1.5 in Figure 6.2 is not seen following an El Nino event, but following a year having low NINO3.4 index.

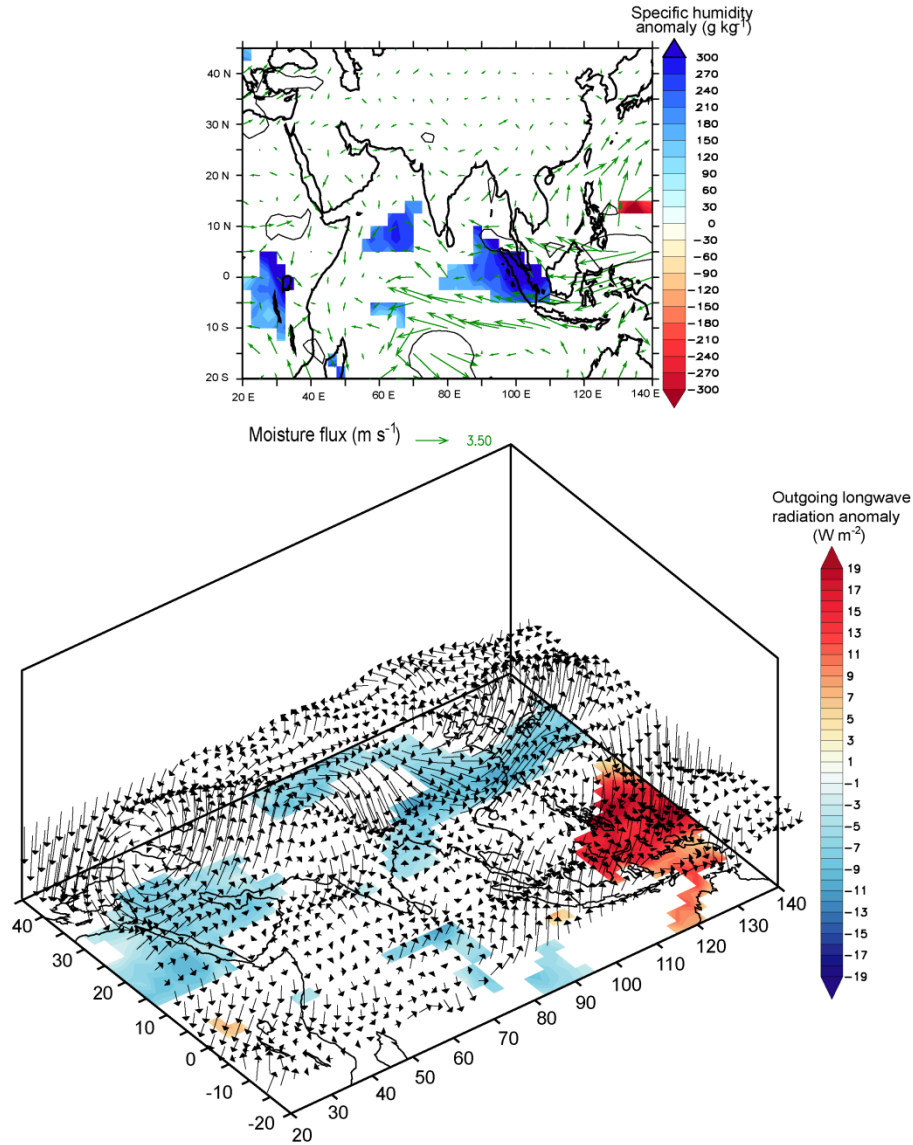


**Figure 6.7** Anomaly diagrams for vertically integrated specific humidity, moisture flux, OLR and wind vectors. (a) Shadings show anomalies in vertically integrated specific humidity (expressed as g kg<sup>-1</sup>) and the vectors indicate vertically integrated moisture flux (expressed as kg kg<sup>-1</sup>\*m s<sup>-1</sup>) during a positive IOD year. The blue (red) shades show the regions where the positive (negative) anomaly of vertically integrated specific humidity exceeds 95% significance level. The black contours enclose the regions where the magnitude of vertically integrated moisture flux anomaly exceeds 95% significance level. (b) Representation of the conditions prevailing after subtracting the conditions prevailing during positive IOD years from the El Nino years. The shading on the horizontal plane represents the OLR anomaly at 95% significance level. The vectors are the wind anomaly (horizontal and vertical) at 300 mb pressure level. The vertical component of wind anomaly has been multiplied by 10.

In reality, it is difficult to separate out the anomalies arising solely due to ENSO or IOD. However, an example of the interaction between El Nino and positive phase of IOD with relation to AI-1.5 is shown in Figure 6.7b. The figure has been constructed by subtracting the meteorological fields (OLR and wind vectors) during purely positive IOD years (defined as NINO3.4 index between -1 and +1 and DMI index above 0.5) from the El Nino years (NINO3.4 index above 1.0). The rationale is the following. Most of the El Nino years have positive phase of IOD associated with them. So it is assumed that subtracting the fields for purely positive IOD years will tend to neutralize positive IOD effect while amplifying the El Nino effect. The years considered as purely positive IOD years are 1978, 1986, 2006, 2008 and 2012. It is seen in Figure 6.7b that once the effect of positive IOD is taken out; there is negative OLR anomaly over SAME with anomalous ascending motion. There is also anomalous descending motion over the IPWP. The central IO shows prominent signs of increased convection (negative OLR anomaly). This depicts how the conditions prevailing over different parts of the tropical Indo-Pacific region may remotely influence the interannual variability in dust load over the northwest IO.

### **6.3. Summary**

To summarize, the chapter shows that dust activity over the AS and the surrounding regions are largely modulated by ENSO. Annual dust activity over this region has an inverse relation with precipitation and soil moisture during the previous boreal winters. These are in turn dependent on the strength of subsidence over the dust source region, which is remotely controlled by ENSO. While La Nina leads to a negative precipitation anomaly and more dust generation during the following summer, El Nino is responsible for an increase in precipitation and suppression of

dust activity. This occurs through the modification to the intensity of convection over the IPWP region by the ENSO system, which affects moisture flux to the dust sources. During the summer following a La Nina, the synoptic situation is that of a lowering of geopotential height over the Indo-Iranian region. Such a set-up favours increased dust transport by increasing the gradient between the Indo-Iranian and the surrounding regions with higher geopotential height. The role of IOD is to oppose the effect of ENSO by modifying the moisture flux in the dust source regions. Overall, ENSO is responsible for 36% of interannual variability of dust activity in the AS and the surrounding regions.

## CHAPTER 7

# INFLUENCE OF DUST ON THE PRIMARY PRODUCTIVITY OVER THE ARABIAN SEA

### 7.1. Influence of dust during winter monsoon

The relation between atmospheric dust aerosols and Chl *a* concentrations over the AS during the NEM period using satellite data and modeling is examined in this section. On an average, NEM has low dust levels in the atmosphere compared to SWM [Li and Ramanathan, 2002]. However, episodic dust storms often occur in association with the *Shamal* weather system [Perrone, 1979; Hubert *et al.*, 1983] in the surrounding arid landmass. Whether any Chl *a* response can be attributed to these episodic dust storms is explored here. The approach used here is to analyze if the oceanic supply of nutrients is adequate to support the observed levels of Chl *a* in a region influenced by dust deposition and to provide an estimation of possible nutrients fluxes due to dust depositions. The period taken for study is NEM of 2002-2003 to 2010-2011 (total 9 NEMs).

#### 7.1.1. Correlations between dust and chlorophyll

Over the AS, a large gradient is seen in dust and Chl *a* concentrations (refer to Figure 2.2). Therefore, in order to study how Chl *a* responds to dust depositions it is important to delineate a suitable region where this signature of dust depositions on Chl *a* can be readily captured. To this end, a correlation map between  $\tau_{du}$  and Chl *a* concentration has been generated. Figure 7.1a shows the distribution of correlation between  $\tau_{du}$  and Chl *a* concentration (along with FLH) in the AS during the NEM.

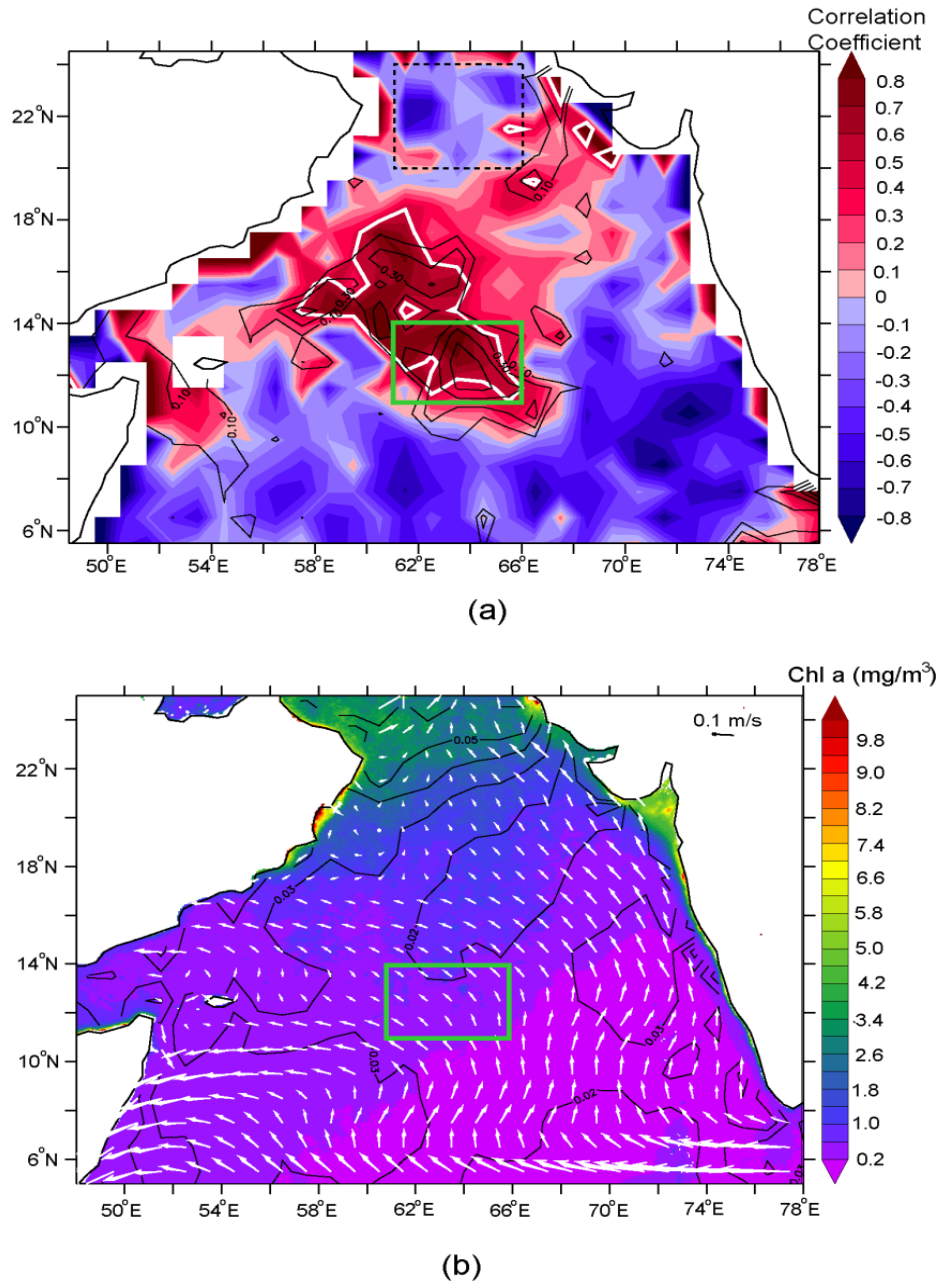


**Figure 7.1** (a) Spatial distribution of correlation coefficient between  $\tau_{du}$  and (b) climatological mean chlorophyll *a* (Chl *a*) concentration ( $\text{mg m}^{-3}$ ) for the NEM of 2002-2003 to 2010-2011 over the AS. In (a) the thick white contours indicate the region having coefficient of correlation between  $\tau_{du}$  and Chl *a* greater than 0.5. The black contours show the distribution of the correlation coefficient between  $\tau_{du}$  and Fluorescence Line Height (FLH). The green box outlines the region central Arabian Sea (CAS), which is considered for studying the effect of episodic dust storms on phytoplankton biomass. The dashed black box demarcates north AS (NAS) (see the text). In (b) the contours indicate the climatological distribution of  $\tau_{du}$  and the vectors represent the current (in  $\text{m s}^{-1}$ ) during the same period.

The  $\tau_{du}$  showed high positive correlation with both Chl *a* (mean value 0.45) and FLH (mean value 0.40) in the central AS (CAS) during NEM period, while the patch of high correlation between  $\tau_{du}$  and Chl *a* extended further north. However, in the north the correlation between  $\tau_{du}$  and FLH was not very high leading to the conclusion that suspended particulate matters probably led to a pseudo correlation. Rest of the AS had little or negative correlation. Though the coastal regions of the AS also showed high positive correlation, for the present study only the open ocean region is considered. This is because: coastal waters usually have high concentrations of nutrients and hence difficult to delineate the signature of atmospheric input and also because retrieval of Chl *a* in coastal waters is a challenge because of the presence of organic matters and suspended particulate matters. Thus, CAS is identified as the open ocean region (having average depth ~4km) where dust has the greatest potential of triggering Chl *a* enhancements. However, CAS had comparatively lower value of  $\tau_{du}$  which was about 0.02 (SD 0.01) (see the contours in Figure 7.1b). In contrast, northern, northeastern and western AS had higher values of  $\tau_{du}$  but very low or negative correlation coefficient with both Chl *a* and FLH. For instance, the northern AS (NAS, defined as 61-66°E, 20-24°N) had mean  $\tau_{du}$  of 0.04 (SD 0.01) and correlation coefficient of -0.17. The climatological NEM average Chl *a* values in NAS and CAS are about 2.0 mg m<sup>-3</sup> (SD 0.55) and 0.3 mg m<sup>-3</sup> (SD 0.08) respectively (Figure 7.1b). The maximum Chl *a* values attained at the peak of the bloom based on 3-day mean climatology during NEM are ~5.0 mg m<sup>-3</sup> and ~0.4 mg m<sup>-3</sup> respectively. Such a north-south gradient in Chl *a* concentrations can be elucidated by the behaviour of the mixed layer (see Figure 7.2), which is a proxy for the intensity of winter convection. The magnitude of the deepest mixed layer attained in NAS at the peak of NEM (end of January to beginning of February) is more than 100m (deepest MLD from Argo was ~122m). However, the influence of winter mixing, although present, somewhat dwindles

towards the south. The deepest Argo-derived MLDs in CAS usually cluster around 80m. Average MLD from Argo during January is 89 m in NAS against 67 m in CAS. Clearly, the deeper penetration of mixing which leads to injection of more nutrients from the subsurface supports the high value of Chl *a* in NAS. The reported NO<sub>3</sub> concentration at the surface is more than 3.0 μM in the NAS in contrast to ~ 2.0 μM NO<sub>3</sub> in CAS [Madhupratap *et al.*, 1996; Morrison *et al.*, 1998]. This is further corroborated by Figure 7.3. The SST increases from 24.5°C in NAS to 26.6°C in CAS, while NO<sub>3</sub> obtained from WOA09, decreases from 2.4 μM in NAS to 0.7 μM in CAS. Note that the NO<sub>3</sub> values from WOA09 are climatological mean for the NEM, while the values of Madhupratap *et al.* [1996] and Morrison *et al.*, [1998] are spot measurements at the peak of NEM of 1995.

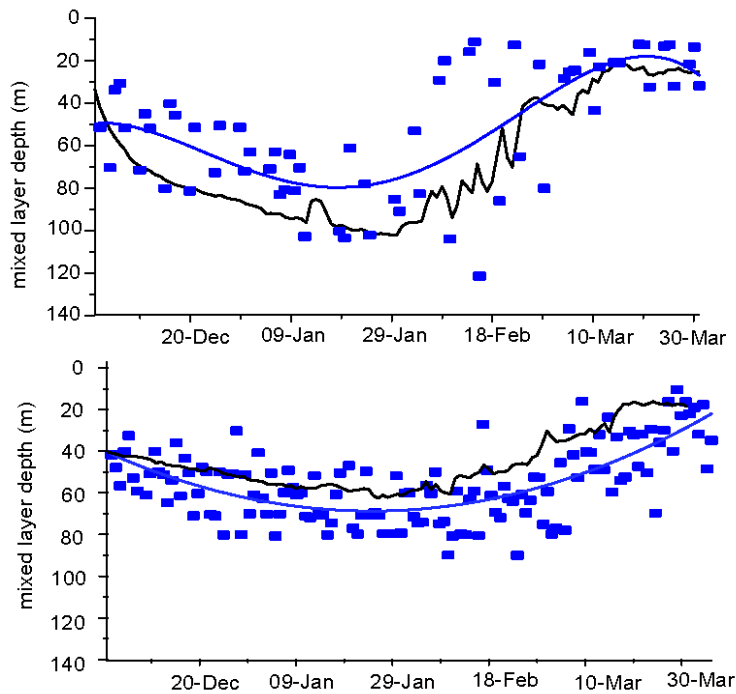


**Figure 7.2** Climatological (2002-3003 to 2010-2011) mixed layer depth (MLD) during the NEM time for NAS (upper panel) and CAS (lower panel). The blue squares are the MLD calculated from Argo data to which a third order polynomial curve was fitted for NAS and a second order polynomial curve was fitted for CAS as indicated by the blue curves. Daily climatology of modeled MLD is shown by the black lines.

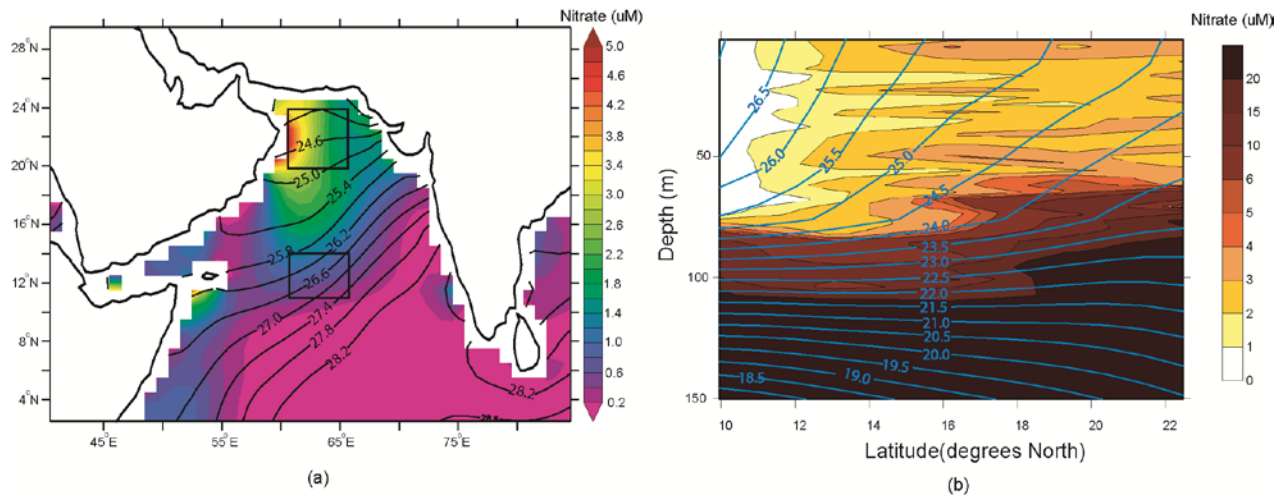


**Figure 7.3** (a) Climatological mean distribution of surface nitrate during the northeast monsoon (shading) overlaid with contours of SST from World Ocean Atlas 2009 (WOA09) and (b) north-south gradient in nitrate values obtained from JGOFS measurements during January overlaid with SST contours from WOA09.

### 7.1.2. Simulated episodic dust depositions

Episodic dust storms during NEM which might influence the region marked from the correlation map (in Figure 7.1a) were identified from NASA Natural Hazards website (<http://earthobservatory.nasa.gov/NaturalHazards/>) for the study period. Further, the near real time MODIS imageries (<http://rapidfire.sci.gsfc.nasa.gov/realtime>) were examined to see the signature of any dust haze over the AS. There were in total 45 dust storms with about 2 to 9 dust storms every year between the NEMs of 2002-2003 to 2010-2011 that had the potential of influencing the Chl *a* in the region. These dust storms either sent off plumes over the AS or much less obvious haze (which is more difficult to identify). The total (wet+dry) dust depositions following each of the episodic dust storms were examined using the results from RegCM4 dust storm simulations. Results are shown in Figure 7.4 for some specific dust storms. High values of dust depositions near the dust sources (similar to that of the distribution of  $\tau_{du}$ )

was seen which was common for all other dust storms. The magnitudes, however, showed a large variation from event to event (see also Table 7.1). For example, dust deposition within CAS varied by about an order of magnitude ranging from  $\sim 10 \text{ mg m}^{-2}$  to more than  $150 \text{ mg m}^{-2}$ . Spatially the dust deposition decreased significantly from northwest AS towards CAS. Total dust depositions is about one order of magnitude higher over NAS (more than  $1000 \text{ mg m}^{-2}$ ) compared to CAS (less than  $100 \text{ mg/m}^2$ ). Comparing the values with those derived from sediment trap, dust depositions ranges from  $33 \text{ mg m}^{-2} \text{ day}^{-1}$  at around  $17^\circ \text{ N}$  to  $4 \text{ mg m}^{-2} \text{ day}^{-1}$  at  $10^\circ \text{ N}$  [Clemens, 1998]. The predominant (more than 90%) size fraction of the deposited dust in CAS were between  $0.01$  and  $1 \mu\text{m}$  (fine mode fraction). Most of the medium to small-sized events were responsible for wet depositions, which varied between  $0.1$  to  $72 \%$ . This has important implications for the bio-availability of Fe as cloud processing of the Fe during wet processes increases the solubility of Fe [see example Duce and Tindale, 1991]. Table 7.1 lists the dust depositions following some of the dust storms.

A comparison of the model simulated  $\tau_{\text{du}}$  with that of remotely sensed data from MODIS/Aqua showed that while the model could successfully reproduce the spatial and temporal pattern of  $\tau_{\text{du}}$ , there is general underestimation with respect to dust storms, which have values of  $\tau_{\text{du}}$  that are well above 1 (Figure 7.4). The extent of underestimation becomes larger towards the southern part of AS. However, in the immediate vicinity of the dust sources the model overestimates. It is important to note that satellite measured  $\tau_{\text{du}}$  captures a snapshot of aerosol each day, while the model is forced by 6-hourly wind. Nonetheless, the underestimations in  $\tau_{\text{du}}$  for some of the highest dust storms are expected to reflect in the dust depositions and the calculations of the possible amount of nutrients that can be derived from dust.

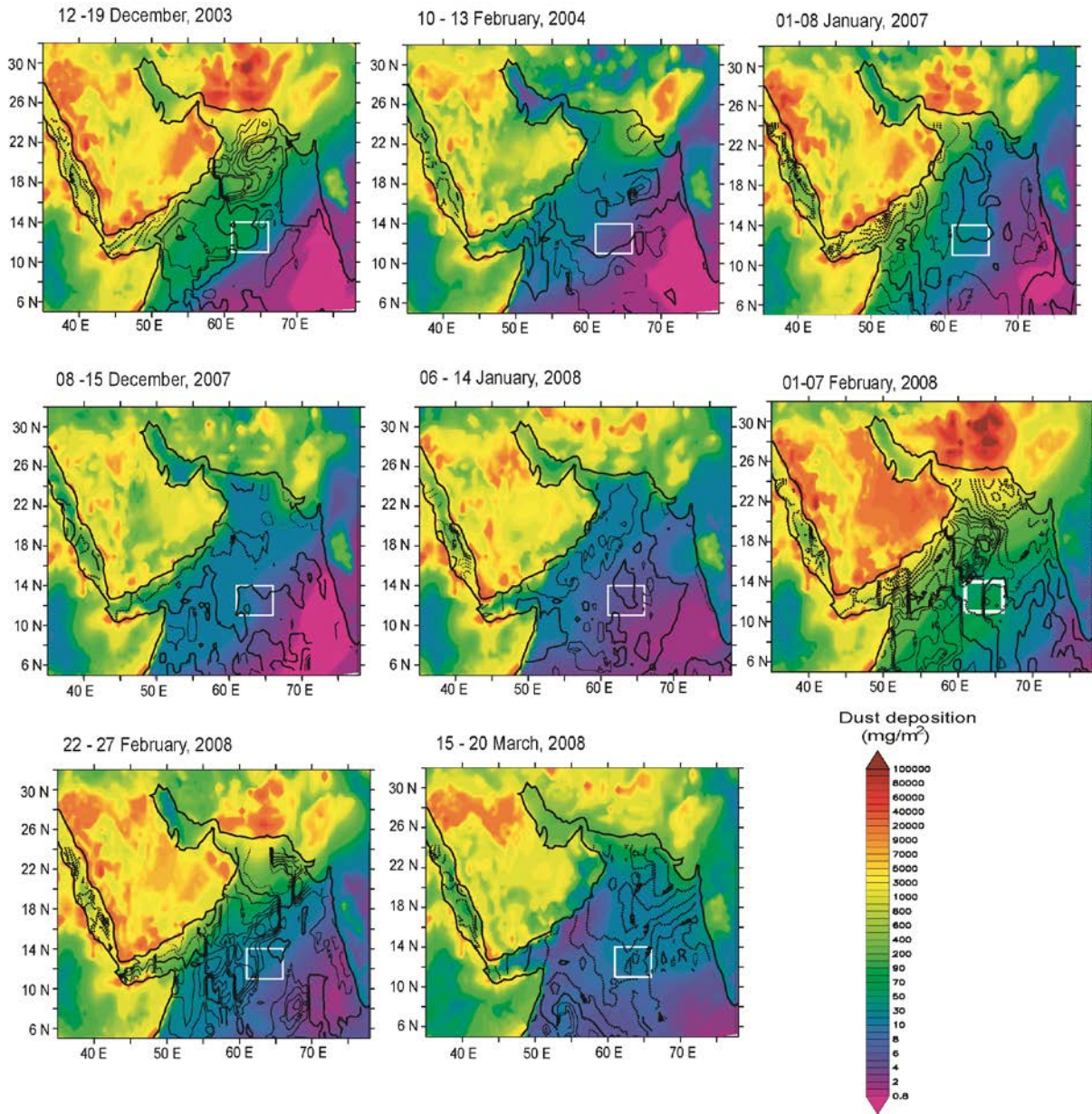


**Figure 7.4** Simulated dust depositions ( $\text{mg m}^{-2}$ ) for the episodic dust storms using RegCM4 model. The black contours indicate the difference between  $\tau_{\text{du}}$  sensed from MODIS/Aqua and model simulation. The value of the thick contour is 0. All contour intervals are 0.1. Continuous contours indicate positive difference and dashed contours indicate negative difference. The white square indicates the study region CAS.

**Table 7.1** Estimated dust deposition in the CAS following dust storms and the possible amount of nutrients that can be derived from dust.

Episode number	* Dust storm detected by satellite	Total dust deposition (mg/m <sup>2</sup> )	Wet deposition (%)	MLD during dust storm (m)	NO <sub>3</sub> supplied (nM)	PO <sub>4</sub> supplied (pM)	‡ DFe supplied (1%)	‡ DFe supplied (10%)	‡ DFe supplied (50%)
E1	12-14 Dec 2003	50	38.0	49	0.32	3.2	0.01	0.10	0.34
E2	09 Feb 2004	5	10.0	59	0.03	0.3	0.001	0.01	0.03
E3	04Jan 2007	23	72.0	58	0.13	1.3	0.003	0.03	0.13
E4	01-03 Dec 2007	9	30.0	35	0.08	0.8	0.001	0.02	0.07
E5	06-07 Jan 2008	5	8.0	50	0.03	0.3	0.001	0.01	0.03
E6	02-05 Feb 2008	161	25.0	56	0.91	9.1	0.02	0.20	1.0
E7	22-23 Feb 2008	12	0.4	45	0.08	0.8	0.002	0.02	0.1
E8	14-15 Mar 2008	12	0.1	22	0.17	1.7	0.003	0.04	0.18

\* The episode dates are given based on satellite detection of the dust storms. It may take few days for the plume to reach CAS. ‡ Unit of DFe is in nM obtained after considering the dust deposition normalized within the mixed layer. DFe (1%), (10%) and (50%) refers to the fraction of Fe in the dust that is soluble.

### 7.1.3. Enhancements of chlorophyll a following episodic dust storms in the central Arabian Sea

Time-series of 3-day composite Chl *a* concentrations were examined within CAS for significant increases in Chl *a* above the background values as well as for the construction of 3-day climatology. The 3-day windows coinciding with the dust storms were discarded to avoid satellite overestimation of Chl *a* concentrations immediately following the dust storms. During the time period under study, 8 episodes of Chl *a* enhancements following the passage of dust storms were discerned (Figure 7.5) when the average Chl *a* enhanced 2 to 4 times the background values in CAS. The criterion chosen to identify the Chl *a* enhancements was that it should be more than 2 SD of the climatological values. These 8 cases were further segregated according to different phases of the mixed layer evolution (Figure 7.6 and Table 7.2). The Chl *a* enhancements during E1 (episode 1) was associated with mature phase of winter convection. E4

and E5 were in the early part of winter convection when the mixed layer was in the deepening phase as inferred from the PWP model. Conversely, the Chl *a* enhancements during E1, E3, E6 and E7 were associated with the shallowing phase of the winter convection. The high Chl *a* episode during E8 took place following the cessation of winter convection when MLD was around 22 m.

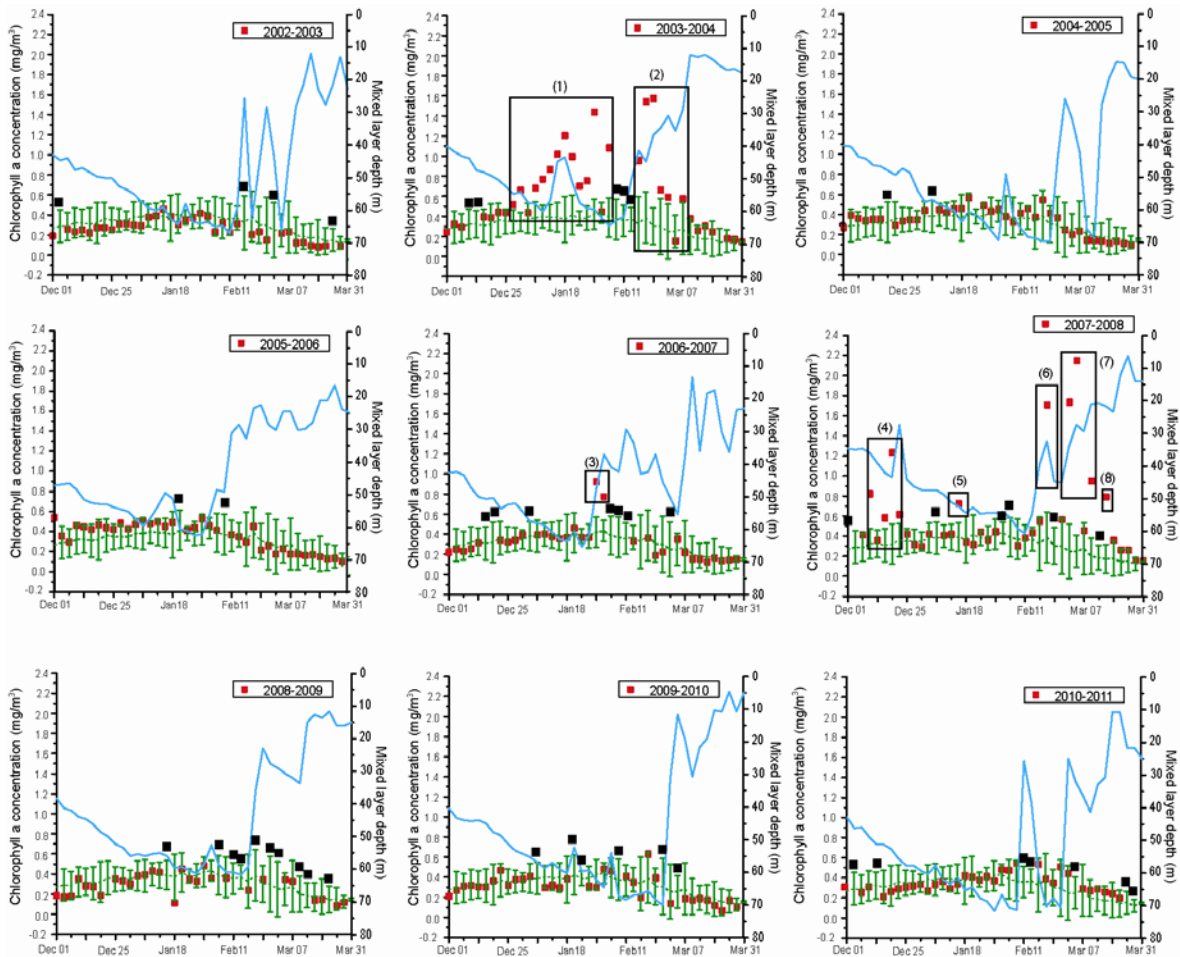


**Figure 7.5** Time-series of 3-day averaged chlorophyll *a* (Chl *a*) concentration ( $\text{mg m}^{-3}$ ) and mixed layer depth (MLD) in central Arabian Sea (CAS) region for the winter monsoon of 2002-2003 to 2010-2011. The green dashed line shows the 3-day Chl *a* climatology and the vertical lines represent their 2 standard deviations; the red squares are the Chl *a* concentrations for each corresponding year; the blue line is the MLD; the black squares indicate the windows when dust storms were observed by satellite around CAS and the hollow black rectangles indicate the cases of Chl *a* enhancement when Chl *a* exceeded 2 SD level. The numbers on the top of the rectangles indicate the episode numbers which are referred in the text as E1, E2 and so on.

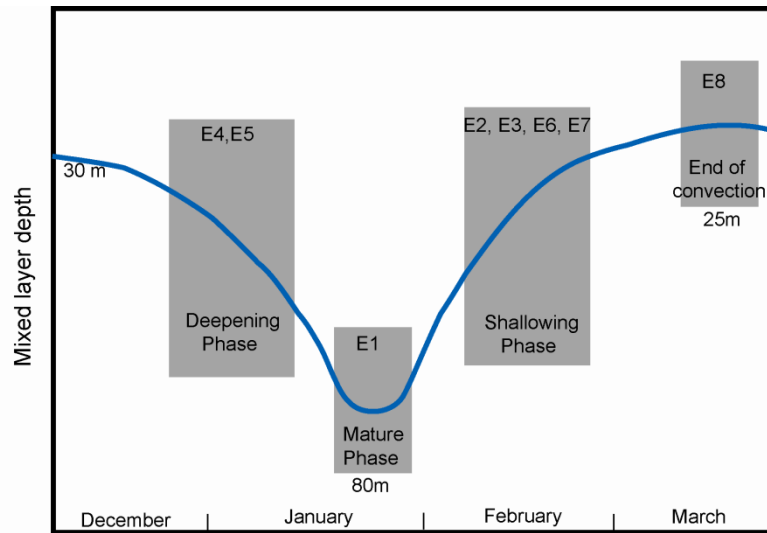


**Figure 7.6** Schematic representation of the time evolution of mixed layer in the Arabian Sea during the northeast monsoon and its association with the episodic chlorophyll enhancements. E1 to E8 indicates the numbers of the episodes of chlorophyll enhancements.

**Table 7.2** Nutrient requirements for the observed surface Chl *a* enhancements in CAS.

Episode Number	Period of the bloom	Maximum Chl <i>a</i> during bloom (mg/m <sup>3</sup> )	MLD during bloom (m)	Total N (C:N:P=106:16:1)	PO <sub>4</sub> (Fe:C=7.5)	DFe (Fe:C=12.8)	DFe (Fe:C=33.9)	
E1	28 Dec 2003-07 Feb 2004	1.40	56 (MP)	3.29	0.20	0.16	0.28	0.74
E2	17 Feb -08 Mar 2004	1.57	36 (SP)	3.69	0.23	0.18	0.31	0.82
E3	30 Jan -04 Feb 2007	0.92	42 (SP)	2.16	0.13	0.11	0.18	0.48
E4	10-24 Dec 2007	1.20	38 (DP)	2.82	0.18	0.14	0.23	0.63
E5	15-17 Jan 2008	0.72	52 (DP)	1.69	0.11	0.08	0.14	0.38
E6	20-22 Feb 2008	1.70	32 (SP)	3.99	0.25	0.20	0.34	0.89
E7	29 Feb-11 Mar 2008	2.14	28 (SP)	5.03	0.31	0.25	0.42	1.12
E8	17-19 Mar 2008	0.79	22 (NC)	1.85	0.12	0.09	0.16	0.42

Units: N and PO<sub>4</sub> are expressed in  $\mu\text{M}$ ; Fe/C, ( $\mu\text{mol/mol}$ ) and DFe in nM . Note the calculated DFe value in CAS is  $\sim 0.2$  nM. The cell Fe/ C quota in the phytoplankton increases with the increase in external DFe availability. MP refers to mature phase of convection-driven mixed layer deepening, SP= shallowing phase, DP=Deepening phase, NC=No convection.

#### 7.1.4. Possible mechanisms leading to phytoplankton blooms in the central Arabian Sea

The pattern of nutrients supply to the AS is primarily governed by the physical processes that control the degree of mixing in the upper layer of the ocean. A deeper mixed layer, as encountered in the NAS, is conducive for supplying higher subsurface nutrients and therefore higher Chl *a* concentrations. A comparatively shallow mixed layer towards the south leads to decreased nutrients supply which is responsible for the lower levels of Chl *a*. It is this set-up which makes CAS a suitable region for detecting the dust induced Chl *a* enhancements. Although dust depositions are expected to have effect on the nutrient stocks within NAS, its effects are largely masked by the huge water column turn-over of nutrients. Dust is more efficient in feeding the phytoplankton stocks in the regions experiencing limited oceanic supply of nutrients. Thus, a low dust flux can have its imprint on the CAS phytoplankton biomass. The region south of CAS has too little oceanic nutrient inventories and/or is too remote from dust sources to have appreciable Chl *a* levels during NEM. So, it is the crucial location of CAS, which hinges on the balance between oceanic nutrients supply and atmospheric depositions, that resulted in the positive correlation between  $\tau_{du}$  and Chl *a*.

There were in total 8 cases of episodic Chl *a* enhancements following passage of dust storms within CAS. However, whether the enhancements can indeed be attributed to atmospheric depositions has to be determined with caution. In general, three factors could lead to the Chl *a* enhancements in the CAS during NEM: (1) advection of nutrients and/or Chl *a* from a region of high production, (2) wind-mixing and/or winter convection and subsequent entrainment of nutrients to the upper ocean and (3) atmospheric deposition of nutrients. Over the CAS, the prevailing ocean surface current at this time of the year is weak ( $\sim 0.1 \text{ m s}^{-1}$ ) and the general direction is from south to north as inferred from Figure 7.1b, which is not congenial for the

advection of nutrients into this region. The same direction was maintained during each of these studied episodes with some changes in magnitudes. Since the region south of CAS is low in Chl *a* and nutrients, advection as a mechanism to support the observed high Chl *a* in CAS can be discounted.

Next, the case of wind-mixing and/or winter convection as potential source of nutrients to the upper ocean is considered by examining the modeled MLD (Figure 7.5 and Table 7.1). Dust storms are generally associated with high wind speed (often exceeding  $10 \text{ m s}^{-1}$ ) that can lead to greater mixing of the upper water column. Indeed, 3 out of the 8 dust storms (E1, E3 and E6) had wind speed greater than  $10 \text{ m s}^{-1}$ . Also the deepening of the mixed layer associated with winter convection leads to gradual build up of nutrients within this layer (see also Figure 7.3), which can potentially support the observed Chl *a* levels. An important observation in this regard is that under dust-storm free conditions MLD has been seen to deepen (due to winter convection or high winds) without any appreciable enhancement (not presented) of Chl *a* indicating that MLD deepening alone cannot mitigate the nutrient(s) limitation in CAS. In view of the above discussion, the requirements of different nutrients (total inorganic N,  $\text{PO}_4$  and dissolved Fe) for the observed enhancements of Chl *a* concentrations have been estimated and compared with the supply of these nutrients.

#### **7.1.5. Requirements versus supply of nutrients**

##### ***Requirements versus supply of nitrate and phosphate***

Table 7.2 shows the requirements of total inorganic N,  $\text{PO}_4$  and dissolved Fe for the observed levels of Chl *a* enhancements following dust storms. For calculating requirements of N and  $\text{PO}_4$ , carbon: nitrogen: phosphorus (C: N: P) ratio of 106:16:1 [Redfield *et al.*, 1963] has been

assumed and C/Chl *a* ( $\mu\text{g carbon}/\mu\text{g Chl } a$ ) ratio of 186 obtained from *in situ* measurements in the AS [Takeda *et al.*, 1995] has been considered. Comparing the values obtained in Table 7.2 with the available nutrients data during JGOFS, it is seen that at the peak of NEM the surface  $\text{NO}_3$  values within CAS ranges between  $\sim 1.0$  to  $3.0 \mu\text{M}$  with an average of  $\sim 2.0 \mu\text{M}$  while the total inorganic Nitrogen ( $\text{NO}_3 + \text{NO}_2 + \text{NH}_4$ ) can be well above  $3.5 \mu\text{M}$  [Morrison *et al.*, 1998]. Madhupratap *et al.* [1996] found surface  $\text{NO}_3$  less than  $2.0 \mu\text{M}$ . Similarly during JGOFS  $\text{PO}_4$  has been seen to vary between  $0.3$  and  $0.5 \mu\text{M}$  within CAS [Morrison *et al.*, 1998]. It is seen that requirements versus the oceanic supply of inorganic N and  $\text{PO}_4$  are in the same order of magnitude given the uncertainties involved and hence can be concluded that inorganic N and  $\text{PO}_4$  were likely not limiting at the time of the dust storms. Although levels of nutrients residing in the mixed layer can vary from year to year, several studies [example Prasanna Kumar *et al.*, 2001] have shown that it is the depth of mixing dictated by the intensity of winter convection that exerts the first order influence on the replenishment of nutrients. The MLD and SST during the times when inorganic N and  $\text{PO}_4$  data were retrieved have been compared with the present episodes leading to the conclusion that there is broad similarity in the intensity of winter convection between these years.

An examination of the dust sample collected on 10<sup>th</sup> April 2013 using high volume sampler at a station in Goa, along the west coast of India, during a dust storm event yielded a  $\text{NO}_3$  concentration of  $\sim 20 \text{ mg g}^{-1}$  of dust (V. Ramaswamy personal communications, 2014). Note that Milli-Q water was used to extract  $\text{NO}_3$  from dust. This when compared to the dust depositions and the depth of mixing within the water column gives an insignificant increase in  $\text{NO}_3$ . This is in agreement with the conclusion drawn by Singh *et al.* [2012] regarding dust aerosol being a limited source of nitrogen and contributing to just 1.2 % of the new production in the AS during

NEM. However, in the case of E7, the requirement of N ( $\sim 5 \mu\text{M}$ ) at the peak of the bloom significantly exceeds that of the estimated instantaneous oceanic supply, indicating that the requirement was likely met from N build up during initial stage of the bloom when the phytoplankton biomass was comparatively low. Similarly,  $\text{PO}_4$  concentration was about  $0.2 \text{ mg g}^{-1}$  of dust, which also results in negligible contribution to the water column. Thus, based on the climatological concentrations of inorganic N (including  $\text{NO}_3$ ) and  $\text{PO}_4$  in the water column and the amount of new nutrients that can be derived from dust, it can be concluded that the main source of N and  $\text{PO}_4$  for these episodes of phytoplankton blooms is the water column. In fact, the climatological concentrations of inorganic N and  $\text{PO}_4$  at the peak of NEM should be able to support Chl *a* levels of  $\sim 1.0 \text{ mg m}^{-3}$ . However, the climatological Chl *a* concentration is about  $0.4 \text{ mg m}^{-3}$ . JGOFS, Landry *et al.* [1998] noted that without any nutrient addition, average phytoplankton growth rate ( $0.5 \text{ day}^{-1}$ ) balances the average grazing mortality rate ( $0.6 \text{ day}^{-1}$ ) in CAS. However, in case of addition of nutrients, the average growth rate becomes  $1.2 \text{ day}^{-1}$ . Also, Goericke [2002] proposed that high grazing rate in the AS likely led to accumulation of excess nutrients in the surface waters. During Here, the possibility of any other nutrient likely limiting Chl *a* concentrations in the AS is explored.

### ***Requirements versus supply of dissolved iron***

It is clear from the previous section that the supply of a nutrient other than N and  $\text{PO}_4$  must have played an important role in episodically enhancing the phytoplankton stocks. Because dust is an important source of Fe it brings forth an interesting possibility that the region might be experiencing some Fe limitation and Fe from episodic dust storms might be leading to the observed episodic Chl *a* enhancements. The main function of iron in the phytoplankton is its role as a catalyst in photosynthesis [Geider and La Roche, 1994]. In Fe limited environments, an

increase in the external supply of dissolved Fe (DFe) will lead to enhanced DFe uptake and specific growth rate. For example, for the oceanic diatom *Thalassiosira oceanica*, an increase in external DFe from 10.6 to 760 pM increases Fe/C ratio ( $\mu\text{mol mol}^{-1}$ ) from 4.9 to 33.9 [Sunda and Huntsman, 1995]. A range of cell Fe/C ratios have been considered to study the DFe requirements under different conditions of availability of DFe and the implied sensitivities: (1) A mean value of 7.5 over the AS based on modelling by Moore *et al.* [2002], (2) based on apparent oxygen utilization, Sunda [1997] arrived at a Fe/C ratio of 12.8 for North Atlantic Ocean during the spring bloom time when primary productivity ranges from 71.3 to 91.1  $\text{mmol C m}^{-2} \text{ day}^{-1}$  [Martin *et al.*, 1993] and (3) a ratio of 33.9 indicator of the highest possible DFe requirements based on laboratory experiments [Sunda and Huntsman, 1995]. Based on the above 3 cell Fe/C ratios (namely 7.5, 12.8 and 33.9) the results for the calculation of DFe requirements are shown in Table 7.2.

Much care is needed in order to ascertain the supply side of DFe. Few sets of *in situ* DFe (defined as Fe that can pass through 0.2  $\mu\text{m}$  filter) measurements exist in the AS during the NEM: (1) surface sampling along 65°E meridional transect and a profile at 15°N by Takeda *et al.* [1995] during end of December, 1992 to beginning of January, 1993 (2) along US JGOFS track by Measures and Vink [1999] during January-February, 1995 as a part of US JGOFS Arabian Sea Process Studies and (3) recently, as a part of the GEOTRACES program, DFe was measured roughly along 69°E, to the east of the present study region during the NEM of 2009 [Nishioka *et al.*, 2013; Vu and Sohrin, 2013]. Two important observations emerge from these studies: (1) a general increase in the DFe concentrations from south to north and (2) within CAS, the ferricline lies at a depth deeper than the nitracline with the difference between the two about 25m. So while the MLD attained at the peak of the NEM can erode the top of the nitracline, it may not be

able to erode the top of the ferricline within CAS. However, within NAS, both nitracline and ferricline can be eroded by the deep mixing under winter convection. This mismatch between the depth of nitracline and ferricline probably has the potential of turning CAS into a Fe-limited region. Being surrounded by dust sources AS receives mineral dust flux throughout the year. Hence, it is first needed to ascertain just the oceanic supply of DFe to see whether the episodic Chl *a* enhancements in CAS can be supported by DFe supplied from the water column alone. For this, the entrainment of DFe with the progress of NEM has been calculated using the profile of *Takeda et al.* [1995] with the assumption that the values reflect the ambient concentrations. This enables to account for the entrainment of DFe with the deepening of mixed layer. The rationale for this assumption is that the DFe values of *Takeda et al.* [1995] is measured earlier in the NEM period compared to *Measures and Vink* [1999] and the values are significantly lower (mean DFe ~ 0.3 nM) compared to those collected by the latter (~1nM). While there are several uncertainties associated with this method, in the absence of more *in situ* DFe measurements, it might be a convenient starting point to understand how oceanic DFe supply is regulated.

The surface DFe values measured by *Takeda et al.* [1995] ranges between 0.15 nM (at 12° 30'N lying within CAS) to 0.47 nM (at 17° 30'N) and at 15°N it is 0.23 nM. The MLD during the study by *Takeda et al.* [1995] at 15°N was around 50m. With the progress of NEM, the deepening of MLD to about 80m within CAS entrains DFe to the surface waters. For an 80m deep MLD, it is estimated that the winter entrainment process results in the mixed layer DFe concentration of about 0.33 nM. This value matches with those from GEOTRACES cruise data collected to the east of the study region with reported value of DFe of 0.35 nM and MLD of around 70m. The available DFe within CAS can be expected to be lower than the above calculated value since the region is situated more south of the location where the DFe profile was collected. The surface

D<sub>Fe</sub> value within CAS is almost 1.5 times less than the surface D<sub>Fe</sub> value at 15°N where the D<sub>Fe</sub> profile has been taken. Accordingly, scaling the D<sub>Fe</sub> value obtained due to winter entrainment at 15°N, the D<sub>Fe</sub> within CAS due to winter entrainment comes to ~0.2 nM. On comparing this value with the D<sub>Fe</sub> requirements estimated from the Fe/C ratios (Table 7.2), it is seen that at Fe/C ratio of 7.5 the entire requirements can be met from the water column for all the cases of Chl *a* enhancements except E7. However, as the Fe/C ratio shifts to higher values, the water column D<sub>Fe</sub> supply becomes increasingly insufficient. For Fe/C ratio of 12.8, episodes E1, E2, E4, E6 and E7 would require an external source of D<sub>Fe</sub>. At Fe/C ratio 33.9, all of the episodic phytoplankton blooms would require external D<sub>Fe</sub>. However, the ratio of 33.9 (mainly applicable for diatoms) is only a theoretical assumption in this case and is highly unlikely as CAS is primarily dominated by Picoplankton.

Next, an aeolian source of D<sub>Fe</sub> is considered. About 3.5% Fe content in the soil dust [*Taylor and McLennan*, 1985] have been assumed. As mentioned earlier, dust deposition within CAS is primarily dominated by fine mode fraction. Upon being deposited on the ocean surface a certain fraction of Fe in the dust is instantaneously dissolved followed by a much longer time dissolution of Fe (ranging from hours to weeks) [*Mackie et al.*, 2006; *Boyd et al.*, 2010]. It has been reported that during May when air masses over the AS comes mainly from the Middle East, thereby enriched with crustal materials, the fraction of labile Fe (II) to total Fe in the fine mode fraction of the aerosol (< 3.0 μm) varies from less than 1% to around 8% [*Seifert et al.*, 1999]. This includes both the instantaneous and the long term soluble Fe fraction. It has also been seen that with increasing distance from land the fraction of labile Fe (II) in the total aerosol can be ~50% [example *Zhuang et al.*, 1992]. By considering D<sub>Fe</sub> constituting 1% (D<sub>Fe1%</sub>), 10% (D<sub>Fe10%</sub>) and 50% (D<sub>Fe50%</sub>) of the total Fe in dust we have calculated the probable ranges of atmospheric

supply of DFe during these episodic events. Based on this, Table 7.1 shows the total amounts of DFe that can be extracted following dust depositions. Note, at this point it has been noticed that considerable underestimation of  $\tau_{du}$  for episodes E1, E6 and E7 (where the  $\tau_{du}$  value exceed 1) which will impact the dust deposited and the amount of DFe that can be possibly derived. A comparison of the possible scenarios when total DFe (dust-derived + oceanic supply) can meet the Chl *a* requirements is depicted in the form of a matrix in Figure 7.7. Maximum cases of Chl *a* enhancements are supported at Fe/C ratio of 12.8 along with DFe<sub>10%</sub> and DFe<sub>50%</sub> (a scenario that is not quite likely). At Fe/C ratio of 7.5, demand for DFe is entirely met from the water column inventory, while at the extreme Fe/C ratio of 33.9 the demand for DFe is too high even at DFe<sub>50%</sub> (an extreme that is also highly unlikely). It is quite possible that Chl *a* during E7 and E8 are likely to draw DFe not only from the immediate dust storm event, but also from previous events as there were continuous pulses of dust depositions during this year (that is NEM of 2007-2008) which would lead to slow build up of DFe within the surface mixed layer. In case of the dust deposition events which are accompanied by significant wet depositions (E1, E3, E4 and E6), the likelihood of bio-availability of Fe increases even for small deposition fluxes. Based on the above calculations in the matrix that highlight the different requirement versus supply scenarios, it can be concluded that the phytoplankton blooms related to episodes E1, E4, E6 and E7 are likely fuelled by dust derived DFe when the Fe/C ratio is 12.8 and about 10% of Fe in dust is dissolved (DFe<sub>10%</sub>). For episode E2, although the requirement of DFe cannot be met by the water column, the calculation implies that dust can support the bloom provided the fraction of Fe that is soluble in dust is much greater than 10%. This in its entirety is conceptualized in Figure 7.8, which shows how the degree of oceanic mixing sets the stage for atmospheric deposition to alter

the biogeochemistry of the region. Following addition of DFe during dust storms there can be multiplication of large sized phytoplankton leading to a bloom condition.

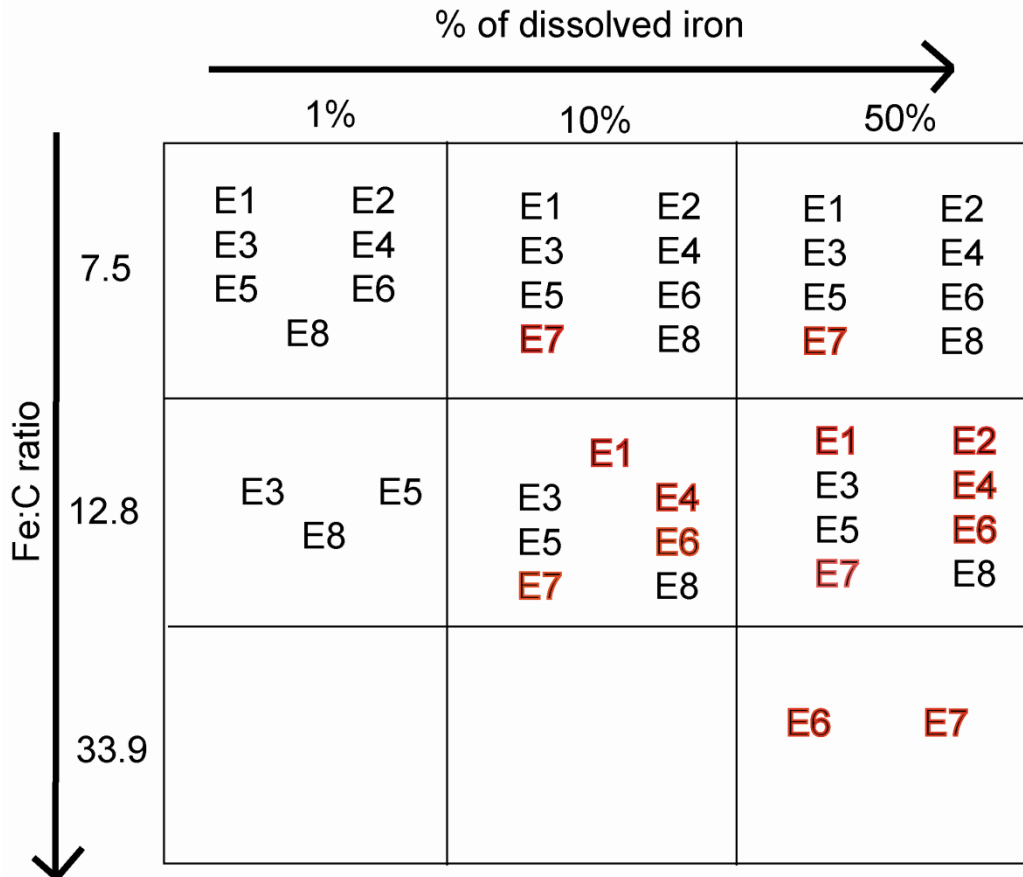


**Figure 7.7** Matrix showing the possible scenarios when observed phytoplankton bloom can be ascribed to be driven by dust depositions and oceanic supply of DFe under varying Fe dissolution threshold and Fe/C ratio. The episodes listed in black are entirely supported by oceanic DFe. The episodes listed in red need an atmospheric source of DFe. The episodes that have not been listed are the ones which cannot be supported even with the atmospheric and oceanic sources of DFe taken together.



ferrihydrite takes hours [Barbeau and Moffett, 2000]; while flagellate mediated phagotrophy can solubilize Fe within a time period of 2 to 10 days [Nodwell and Price, 2001].

Thus, from the above discussion it is evident that the possibility of an atmospheric supply driving the episodic blooms depends on the amount of DFe that can be extracted from the dust depositions and the assumed Fe/C ratios. Although CAS shows a positive correlation between  $\tau_{du}$  and Chl *a*, dust depositions actually leading to phytoplankton blooms has to be dealt with caution as several factors like amount of dust deposition, DFe that can actually be extracted, the MLD and availability of other nutrients come into play. However, the important point remains that although all dust storms are not followed by phytoplankton blooms, these blooms are detected only following dust storms. In the absence of dust storms, even high winds do not lead to blooms indicating nutrient deficiency in the system. This probably arises because the top of the nitracline is shallower than the ferricline. The estimates of dust-derived DFe given by here are only indicative. With the availability of more DFe data from this region, the ranges of DFe that can be supplied by dust can be narrowed down.

#### **7.1.6. Significance of dust deposition related to community structure of the Arabian Sea**

The AS as a whole undergoes a steady transition from a stratified oligotrophic system to a highly productive system characterized by deep mixing with the onset of NEM. Such transition is usually accompanied by community succession: from Picoautotrophs to larger size Microautotrophs, especially Diatoms and Dinoflagellates [Garrison *et al.*, 2000]. However, southwards, within the nutrient-depleted CAS the autotrophic biomass is mainly dominated by Picoplankton followed by Nanoplankton [Garrison *et al.*, 2000]. This north-south distinction in the autotrophic community is also reflected in the grazers consisting of mainly heterotrophic

bacteria indicative of microbial food web within CAS. In contrast, Mesozooplankton makes up much of the food web in the productive parts of AS [Smith and Madhupratap, 2005]. Without any nutrient addition the growth rate ( $\sim 0.4 \text{ d}^{-1}$ ) of the autotrophs within CAS matches the grazing rate ( $\sim 0.5 \text{ d}^{-1}$ ) [Landry *et al.*, 1998]. It has been estimated that grazing accounts for consumption of 29% of the Chl *a* [Caron and Dennett, 1999] within the CAS region. If this amount is added to the levels of Chl *a* sensed by satellites, then the actual requirement for nutrients become even larger. Takeda *et al.* [1995] has demonstrated that phytoplankton in AS achieved a mean growth rate ( $\text{d}^{-1}$ ) of 0.6 following addition of  $\text{NO}_3$  and Fe, in spite of not screening out the grazers. The increase in phytoplankton biomass in their experiment was accompanied by predominance of diatoms leading to the conclusion that phytoplankton growth is co-limited by  $\text{NO}_3$  and Fe, at least in the initial stage of winter monsoon. However, as the winter convection intensifies with time, the nitrate builds up within the mixed layer. Eventually, the phytoplankton growth may be limited by Fe and an adequate atmospheric deposition of DFe can possibly relieve them of Fe stress. It is worth mentioning that the contribution of new Fe to total Fe supply varies from 10% in high-nutrient-low-chlorophyll (HNLC) waters to 50% in Fe-replete waters [see Boyd and Ellwood, 2010 and references therein]. As the  $\text{NO}_3 + \text{Fe}$  addition leads to increased Chl *a*, other nutrients like P and Si becomes limiting. Such a shift in the community with the addition of  $\text{NO}_3 + \text{Fe}$  has important implications for carbon export as this seemingly expands the domain of winter convection much more southwards.

#### **7.1.7. Contribution of dust to interannual variability in the chlorophyll**

The incidences of Chl *a* enhancements following the passage of dust storms leads to the question: how far are the episodic events important in defining the interannual variability of Chl *a* over CAS during NEM? Figure 7.9a clearly depicts the difference between phytoplankton

biomass during the NEMs of the 3 years having highest  $\tau_{du}$  (2003-2004, 2006-2007 and 2007-2008) and rest of the 6 years with low  $\tau_{du}$  (Figure 7.9b). The NEMs of these 3 years together contributed to 46.6% of the total Chl *a* concentration within CAS when all the 9 years of the study period are considered. The NEMs of 2003-2004 and 2007-2008 alone contributed to 38.5% of Chl *a* within CAS. The 2 years with the highest values of  $\tau_{du}$  were the NEMs of 2003-2004 ( $\tau_{du}$  of 0.04) and 2007-2008 ( $\sim 0.05$ ). These 2 years had average Chl *a* of  $0.83 \text{ mg m}^{-3}$  and  $0.57 \text{ mg m}^{-3}$  respectively. In contrast, the years with lower levels of dustiness had average Chl *a* of  $0.31 \text{ mg m}^{-3}$ . For the 3 years with the highest  $\tau_{du}$  (2003-2004, 2006-2007 and 2007-2008), CAS accounted for about 43.0% of the total Chl *a* of the AS ( $60\text{-}67^\circ\text{E}$ ,  $5\text{-}25^\circ\text{N}$ ) during NEM period. For the rest of the 6 years CAS accounted for only 24.3% of the total Chl *a* of the entire AS for the NEMs. It is therefore evident that, although, CAS supports low levels of Chl *a* biomass during the NEM time, the influence of episodic events like dust depositions supplying DFe can turn CAS into a productive system and account for a large part of the interannual variability within this region.

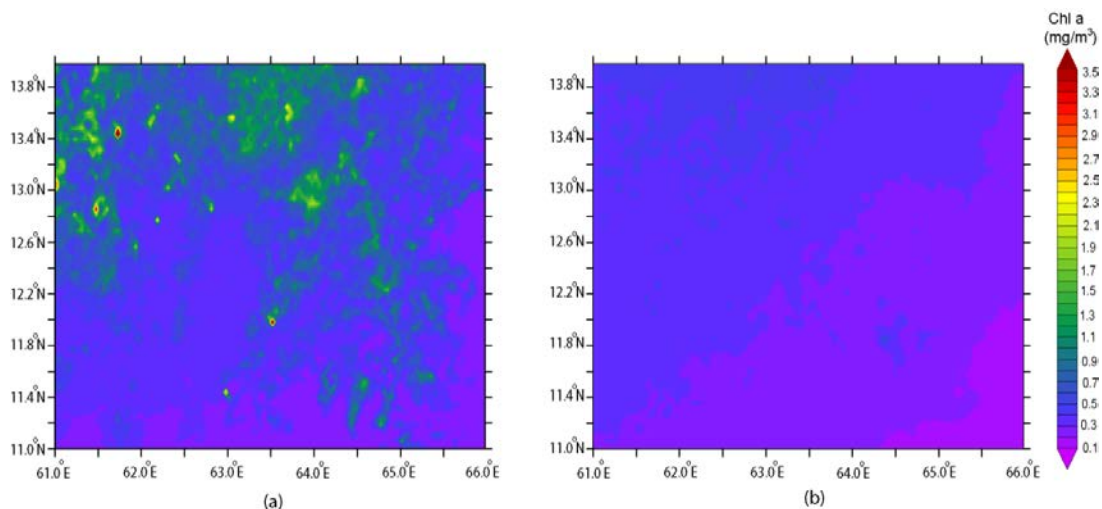


**Figure 7.9** Mean northeast monsoon time chlorophyll *a* concentration ( $\text{mg m}^{-3}$ ) for (a) heavy dust years (2003-2004, 2006-2007 and 2007-2008) and (b) less dust years (2002-2003, 2004-2005, 2005-2006, 2008-2009, 2009-2010 and 2010-2011) within central Arabian Sea.

## **7.2. Influence of dust during rest of the year**

The probable influence of dust depositions on the Chl *a* concentrations of the AS during the NEM period is clear from the previous section. In order to investigate if Chl *a* concentrations show some response to dust depositions during other seasons, maps showing correlations between  $\tau_{du}$  and Chl *a* concentrations for other seasons have also been constructed. These maps are shown in Figure 7.10 for SIM period, Figure 7.11 for SWM period and Figure 7.12 for FIM period.

### **7.2.1. Influence of dust during spring intermonsoon**

SIM is the time of the year when the dust deposition into the AS starts increasing (as is shown in Table 5.2). It is seen from Figure 7.10 that there are several scattered patches throughout the AS that show high positive correlations between  $\tau_{du}$  and Chl *a* concentrations without, however, showing much coherent pattern. This is also true for the correlations between  $\tau_{du}$  and FLH. Moreover, the regions of positive correlations between  $\tau_{du}$  and Chl *a* concentrations and that between  $\tau_{du}$  and FLH do not coincide. This makes it difficult to come to any conclusions regarding the probable influence of dust on the Chl *a* levels. Also, the AS is oligotrophic during this time of the year [Morrison *et al.*, 1998]. Therefore, NO<sub>3</sub> becomes a limiting nutrient. Since it is clear from Section 7.1 that dust is a poor supplier of NO<sub>3</sub> in the open ocean, phytoplankton growth will likely to be limited by the supply of macronutrients, even though sufficient amount of DFe is likely to be supplied by dust.

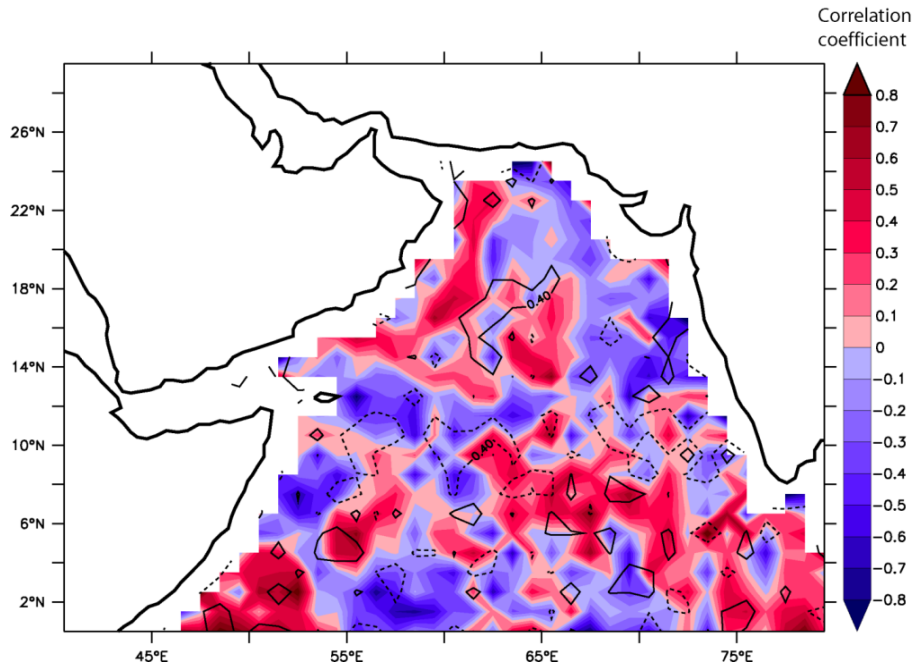


**Figure 7.10** Distribution of correlation coefficient between dust optical depth and chlorophyll *a* concentration over the AS (shading) for the spring intermonsoons of 2003-2011. The black contours enclose the regions where the correlation between dust optical depth and FLH exceeds a magnitude of 0.4: continuous contours for positive correlation and dashed contours for negative correlation.

### 7.2.2. Influence of dust during southwest monsoon

During the SWM time period a coherent region of high positive correlations between  $\tau_{du}$  and Chl *a* concentrations is seen in the northern AS (see Figure 7.11). This region also exhibits positive correlations between  $\tau_{du}$  and FLH. This is the time of the year when AS experiences maximum dust depositions and also has high supply of macronutrients because of upwelling and horizontal advection. Thus, it is likely that dust might have some influence on the phytoplankton biomass of the AS by supplying DFe (although the same can be supplied by upwelling). However, this positive correlation between  $\tau_{du}$  and Chl *a* concentrations have to be regarded with caution. This is primarily because, during the SWM time, satellite retrieval of Chl *a* is hampered by the presence of cloud over the AS. By examining the Chl *a* images year by year, it is evident that the

region of high correlation between  $\tau_{du}$  and Chl *a* concentration has large number of Chl *a* pixels missing. Therefore, although dust can influence Chl *a* levels during this time of the year, any definite conclusion cannot be arrived at with the present data set.

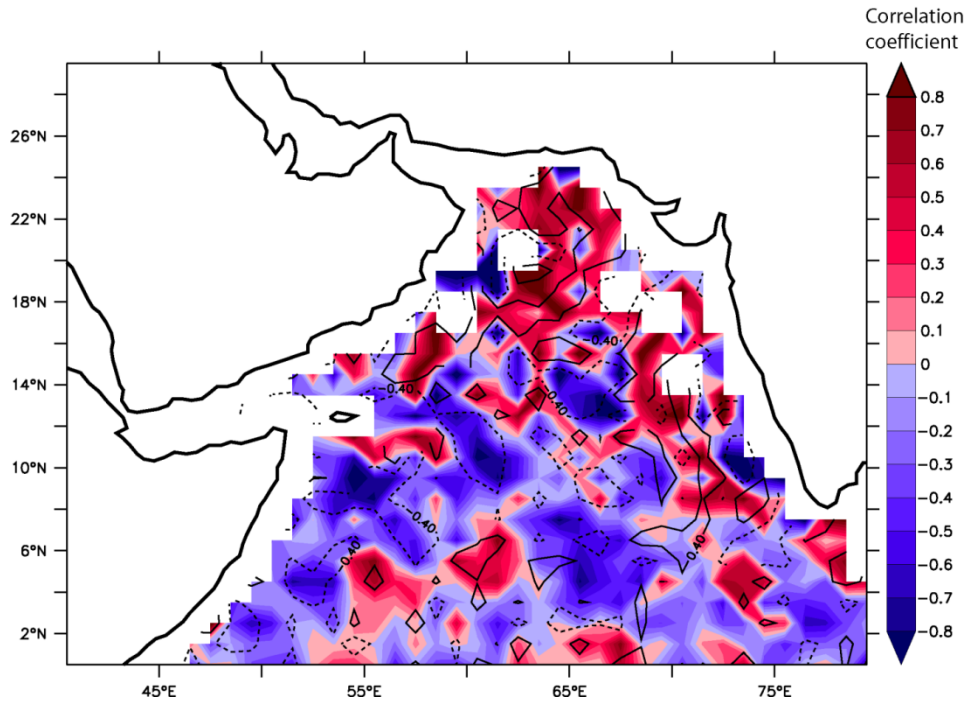


**Figure 7.11** Spatial distribution of correlation coefficient between dust optical depth and chlorophyll *a* concentration over the AS (shading) for the southwest monsoons of 2003-2011. The black contours enclose the regions where the correlation between dust optical depth and FLH exceeds a magnitude of 0.4: continuous contours for positive correlation and dashed contours for negative correlation.

### 7.2.3. Influence of dust during fall intermonsoon

Figure 7.12 shows the correlations between  $\tau_{du}$  and Chl *a* concentrations for the FIM period. This is the time of lowest dust deposition over the AS. This is also an oligotrophic time of the year. However, some remnants of macronutrients from the SWM upwelling may still be present during the early part of the FIM. Like SIM, there are several scattered patches of positive correlations between correlations between  $\tau_{du}$  and Chl *a* concentrations over the AS during FIM.

Of particular interest is the one located off the Oman coast centred on 15°N latitude and 60°E longitude. The patch also shows positive correlation between  $\tau_{du}$  and FLH. It has been proposed by the modeling study of *Wiggert and Murtugudde*, [2007] that there is a possibility of Fe limitation during the late SWM period in the western AS. A case of Fe-limitation was also reported by *Naqvi et al.* [2010] during the waning stage of the SWM period off Oman. They hypothesized that the upwelled water during the SWM came from above the depth of the oxygen-poor DFe-rich zone. Thus, within this upwelled water, the  $\text{NO}_3$ : DFe ratio is much above the value ( $\sim$  taken as 15,000) at which Fe limitation can take place. However, relating Chl *a* enhancements to dust depositions within this track proved inconclusive mainly because of the strong advection still present during the beginning of FIM.

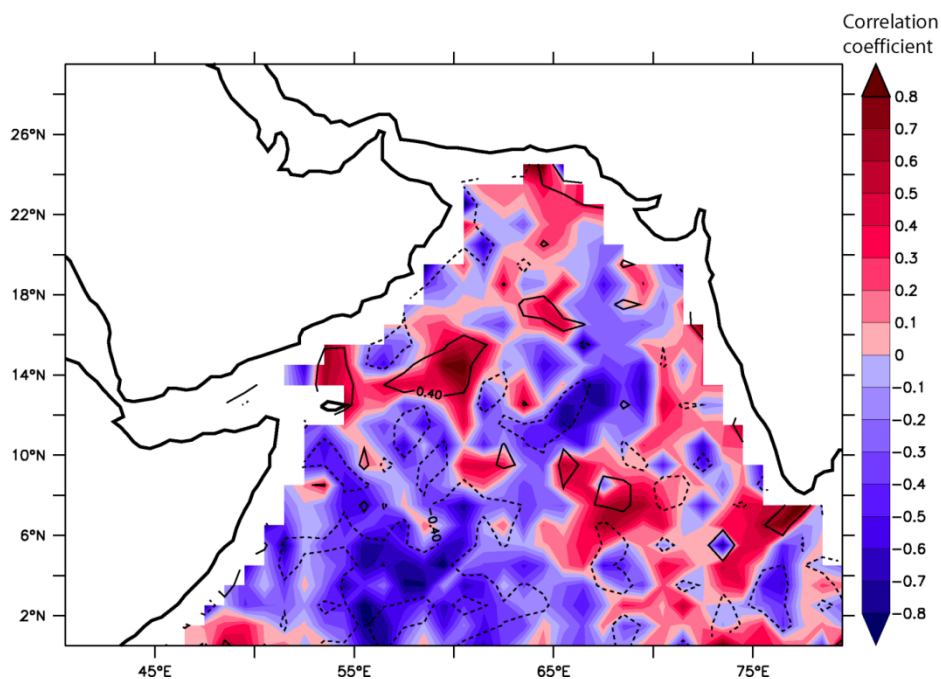


**Figure 7.12** Spatial distribution of correlation coefficient between dust optical depth and chlorophyll *a* concentration over the AS (shading) for the fall intermonsoons of 2003-2011. The black contours enclose the regions where the correlation between dust optical depth and FLH exceeds a magnitude of 0.4: continuous contours for positive correlation and dashed contours for negative correlation.

### 7.3. Summary

The chapter brings to light the mechanistic relationship between phytoplankton blooms and episodic dust depositions in the AS during the NEM period. Dust depositions can lead to Chl *a* enhancements within CAS, which is located away from the realm of active winter convection. Overall, there were 45 dust storms over the AS during the NEMs of 2002-2003 to 2010-2011 of which only 8 were followed by Chl *a* enhancements. For each of these 8 cases of Chl *a* enhancements, a comparison was made to see how much is the demand for different nutrients (like N, PO<sub>4</sub> and DFe) to sustain the observed levels of Chl *a* versus the supply of these nutrients. For the supply side, it was examined if the oceanic supply of nutrients were enough to support the observed levels of Chl *a* and, if not, how much nutrients can be obtained from dust depositions. It is likely that the deepening of the mixed layer can incorporate enough N and PO<sub>4</sub>, but not enough DFe from the subsurface waters leading to potential Fe limitation. Following episodic dust storms, the supply of DFe can alleviate the Fe limitation and result in phytoplankton blooms. Although, all the phytoplankton blooms within CAS were observed following episodic dust events, only four blooms can be attributed to dust depositions. It is seen that the years with high levels of dust can contribute 47% of the total Chl *a* concentrations in the AS during the NEM period. Such conclusions cannot be arrived at for other seasons primarily because of the nature of the data used.

## **CHAPTER 8**

### **SUMMARY AND OUTLOOK**

The Arabian Sea is one of the dustiest places on the globe. Dust aerosols over the Arabian Sea have been known to have numerous effects on the climate of the region by modifying the radiative balance, hydrological cycle and the large-scale monsoon circulations. Also, it has been seen in other parts of the globe that dust can potentially fertilize the ocean by supplying nutrients. However, there remain huge gaps in understanding the dust cycle and its variability and how dust-derived nutrients can impact the phytoplankton biomass so far as the Arabian Sea is concerned. To this end, the present thesis investigates the temporal variability of the dust cycle over the Arabian Sea at seasonal scale and what factors control this variability, the influence of the climate modes in controlling the interannual variability of dust and the effect of dust depositions on the phytoplankton biomass of the region.

To achieve this, first, seasonal cycle of dust emission, transport and deposition in the Arabian Sea and its surroundings has been studied using a regional climate model RegCM4. The model has been run for total of ten years from 2001 to 2010 to study the horizontal as well as the vertical distribution of dust and along with the atmospheric circulations responsible giving maximum stress on the southwest monsoon period. Next, the influence of El Nino-Southern Oscillations and the Indian Ocean Dipole on the levels of dust activity has been investigated with the help of 26 years of Aerosol Index data from satellite remote sensing and meteorological fields derived from reanalysis products. The study tries to unravel how these climate modes might remotely control the moisture flux and hence the dust activity in the dust source regions.

Finally, the possible role of dust in supporting the phytoplankton biomass of the Arabian Sea by supplying different nutrients has been explored by tracking the satellite-derived chlorophyll concentrations following episodic dust storms during the northeast monsoon. The demand versus supply (oceanic + atmospheric) of different nutrients have been calculated for each of the observed cases of chlorophyll enhancements to decide if a phytoplankton bloom can be attributed to dust depositions or not.

The major outcome of the thesis is that at seasonal scale the southwest monsoon circulation system is the main controller of the dust cycle accounting for 47% of dust emissions in the regions surrounding the Arabian Sea and 79% of dust depositions into the Arabian Sea. During the southwest monsoon, the intertropical convergence zone divides the south and southwest Asian landmass into two regimes: (1) to the east and the south of the convergence zone dust emission and its subsequent transport is accomplished by the southwest monsoon wind system. However, the energetic Findlater Jet blocks the transit of the dust over the open Arabian Sea, thereby; confining dust-laden air mostly to the west, (2) to the west and the north of the convergence zone dust mobilization and its transport is accomplished by the northwesterly and northerly wind system associated with the surrounding high pressure regions. Being confined within the lower few kilometres (~3 km) of the atmosphere, the southwest monsoon system is overridden by dusty airmass coming from southwest Asia and the Middle East. However, near the top of the Troposphere (above 11 km), the easterly return flow of the southwest monsoon system recirculates dust towards the west. At this level, Asian dust can be transported to long distances and thereby influence the climate of large part of the globe.

At interannual scale, it is shown that El Nino-Southern Oscillations can significantly influence the dust activity in the Arabian Sea and its surroundings. It is seen that La Nina conditions favour

dust production by remotely suppressing the amount of winter precipitation in the principal dust source regions surrounding the Arabian Sea. The opposite is true for El Nino conditions. This is achieved by modulation of the intensity of convection over the Indo-Pacific warm pool region. This can strengthen or weaken the intensity of subsidence over the dust source regions which, in turn, can impact the precipitation over the region. El Nino-Southern Oscillations further modifies the conditions favouring dust transport during the following summer by affecting the geopotential height over south and southwest Asia. El Nino-Southern Oscillations accounts for 36% of the interannual variability of dust activity over the Arabian Sea. Indian Ocean Dipole acts to oppose the effect of the El Nino-Southern Oscillations in the Arabian Sea.

Finally, the thesis also illustrates the fact that dust can influence the phytoplankton biomass of the central Arabian Sea during the northeast monsoon by supplying micronutrient iron. In the central Arabian Sea the intensity of the winter convection is much less and the ferricline is deeper than the nitracline. It is probable that any deepening of the mixed layer can supply enough nitrate and phosphate, but not enough iron. This might lead to a situation of iron limitation. Following episodic dust depositions, if enough iron is supplied, then phytoplankton can proliferate. During the northeast monsoon period, years with high levels of dust contribute to 47% of the total chlorophyll concentrations in the Arabian Sea. Such conclusions cannot be arrived at for other seasons.

The thesis has tried to shed light into the factors that control the dust load over the Arabian Sea at different temporal scales. Over the last few decades, there are compelling evidences of shifts in the climate over the north Indian Ocean. By analyzing the dust variability at different temporal scales, the present study implies that any changes in the ocean-atmosphere conditions over the north Indian Ocean has huge potential to effect the dust cycle. This has serious implications

because of the feedback that dust has on the climate of the region. For example, a climate-induced change in the dust load will have effect on the radiative forcing at different levels of the atmosphere. This in turn influences the atmospheric circulations and the monsoons. Therefore, it is critical to understand the behaviour of the dust cycle under a global warming scenario. An analysis of paleo-dust data might provide some clues to this end. Furthermore, the thesis also shows how dust can influence the phytoplankton biomass over a region. This aspect of the thesis has particular relevance to the carbon cycle. An important way to take the work forward is by linking the surface productivity with the carbon flux at depths. It is crucial to understand if any signature of the change in the size of the dust cycle translates into deep ocean carbon flux. One way to approach this problem is to couple a carbon cycle model with an atmospheric model and explore the carbon flux by doubling or halving the dust depositions. Another route is through *in situ* experiments that will try to quantify carbon flux at some depths in the ocean following artificial fertilization by dust.

## Bibliography

Abdi Vishkaee, F., C. Flamant, J. Cuesta, L. Oolman, P. Flamant, and H. R. Khalesifard (2012), Dust transport over Iraq and northwest Iran associated with winter Shamal: A case study, *J. Geophys. Res.*, 117, D03201, doi:10.1029/2011JD016339.

Abish, B., and K. Mohanakumar (2013), Absorbing aerosol variability over the Indian subcontinent and its increasing dependence on ENSO, *Glob. Plan. Change*, 106, 13–19.

Ackerman, S. A., and S. K. Cox (1989), Surface weather observations of atmospheric dust over the Southwest summer monsoon region, *Meteorol. Atmos. Phys.*, 41, 19–34.

Alpert, P., and B. Ziv (1989), The Sharav Cyclone: Observations and some theoretical considerations, *J. Geophys. Res.*, 94(D15), 18495–18514, doi:10.1029/JD094iD15p18495.

Antonov, J. I., D. Seidov, T. P. Boyer, R. A. Locarnini, A. V. Mishonov, H. E. Garcia, O. K. Baranova, M. M. Zweng, and D. R. Johnson (2010), *World Ocean Atlas 2009, vol. 2, Salinity*, edited by S. Levitus, 184 pp., U.S. Govt. Print. Off., Washington, D. C.

Awad, A.M., and A.W.S Mashat (2013), Synoptic features associated with dust transition processes from North Africa to Asia, *Arab J Geosci.*, 7, 2451-2467, doi:10.1007/s12517-013-0923-4.

Badarinath, K. V. S., S. K. Kharol, D. G. Kaskaoutis, A. R. Sharma, V. Ramaswamy, and H. D. Kambezidis (2010), Long range transport of dust aerosols over Arabian Sea and Indian region: A case study using satellite data and ground-based measurements, *Glob. Plan. Change*, 72, 164–181, doi:10.1016/j.gloplacha.2010.02.003.

Baddeley, H (1860), Whirlwinds and Duststorms of India, pp 6.

Banse, K. (1959), On upwelling and bottom-trawling off the southwest coast of India, *J. Mar. Biol. Assoc. India*, 1, 33–49.

- Barber, R. T., J. Marra, R. C. Bidigare, L. A. Codispoti, D. Halpern, Z. Johnson, M. Latasa, R. Goericke, and S. L. Smith (2001), Primary productivity and its regulation in the Arabian Sea during 1995, *Deep Sea Res., Part II*, 48, 1127–1172.
- Barbeau, K., and J. W. Moffett (2000), Laboratory and field studies of colloidal iron oxide dissolution as mediated by phagotrophy and photolysis, *Limnol. Oceanogr.*, 45, 827–835.
- Barlow, M., H. Cullen, and B. Lyon (2002), Drought in central and southwest Asia: La Nina, the warm pool, and Indian Ocean precipitation, *J. Climate*, 15(7), 697–700.
- Barlow, M., A. Hoell, and F. Colby (2007), Examining the wintertime response to tropical convection over the Indian Ocean by modifying convective heating in a full atmospheric model, *Geophys. Res. Lett.*, 34, L19702, doi:10.1029/2007GL030043.
- Bishop, J. K. B., R. E. Davis, and J. T. Sherman (2002), Robotic observations on dust storm enhancement of carbon biomass in the North Pacific, *Science*, 298, 817–821.
- Booth, B., N. Dunstone, P. Halloran, T. Andrews, and N. Bellouin (2012), Aerosols implicated as a prime driver of twentieth-century North Atlantic climate variability, *Nature*, 484, 228–232.
- Boyd, P. W., and M. J. Ellwood (2010), The biogeochemical cycle of iron in the ocean, *Nat. Geosci.*, 3, 675–682, doi:10.1038/ngeo964 .
- Boyd, P. W., D. S. Mackie, and K. A. Hunter (2010), Aerosol iron deposition to the surface ocean—Modes of iron supply and biological responses, *Mar. Chem.*, 120, 128–143, doi:10.1016/j.marchem.2009.01.008.
- Caron, D. A., and M.R. Dennett (1999), Phytoplankton growth and mortality during the 1995 northeast monsoon and spring intermonsoon in the Arabian Sea, *Deep Sea Res., Part II*, 46, 1665–1690.
- Chester, R., A.S. Berry and K.J.T. Murphy (1991), The distributions of particulate atmospheric trace metals and mineral aerosols over the Indian Ocean, *Mar. Chem.* 34, 261–290.

Claustre, H., A. Morel, S. B. Hooker, M. Babin, D. Antoine, K. Oubelkheir, A. Bricaud, K. Leblanc, B. Quéguiner, and S. Maritorena (2002), Is desert dust making oligotrophic waters greener? *Geophys. Res. Lett.*, 29(10), 1469, doi:10.1029/2001GL014056.

Clemens, S. C. (1998), Dust response to seasonal atmospheric forcing: Proxy evaluation and calibration, *Paleoceanography*, 13, 471–490, doi:10.1029/98PA02131.

Clifford, M., C. Horton, J. Schmitz, and L. H. Kantha (1997), An oceanographic nowcast/forecast system for the Red Sea, *J. Geophys. Res.*, 102 (C11), 25101–25122, doi:10.1029/97JC01919.

Creamean, J. M., K. J. Suski, D. Rosenfeld, A. Cazorla, P. J. DeMott, R. C. Sullivan, A. B. White, F. M. Ralph, and K. A. Prather (2013), Dust and biological aerosols from the Sahara and Asia influence precipitation in the western US, *Science*, 339(6127), 1572–1578, doi:10.1126/science.1227279.

Darbyshire, M. (1967), The surface waters off the coast of Kerala, south-west India, *Deep Sea Res.*, 14, 295–320.

Dayan, U., Ziv, B., Shoob, T. and Enzel, Y. (2008), Suspended dust over southeastern Mediterranean and its relation to atmospheric circulations, *Int. J. Climatol.*, 28, 915–924. doi: 10.1002/joc.1587.

Deepshikha, S., S. K. Satheesh, and J. Srinivasan (2006), Dust aerosols over India and adjacent continents retrieved using METEOSAT infrared radiance. Part I: Sources and regional distribution, *Ann. Geophys.*, 24, 37–61.

Dickinson, R.E., A. Henderson-Sellers, and P.J. Kennedy (1993), Biosphere-atmosphere Transfer Scheme (BATS) Version 1e as Coupled to the NCAR Community Climate Model, NCAR Technical Note NCAR/TN-387+STR, doi: 10.5065/D67W6959.

Du, Y., S.-P. Xie, G. Huang, and K. Hu (2009), Role of air-sea interaction in the long persistence of El Niño-induced North Indian Ocean warming, *J. Clim.*, 22, 2023–2038.

Duce, R.A., and N. W. Tindale (1991), The atmospheric transport of iron and its deposition in the ocean, *Limnol. Oceanogr.*, 36, 1715–1726.

Dunion, J. P., and C. S. Velden (2004), The impact of the Saharan air layer on Atlantic tropical cyclone activity, *Bull. Am. Meteorol. Soc.*, 85(3), 353–365.

Eck, T. F., et al. (2008), Spatial and temporal variability of column-integrated aerosol optical properties in the southern Arabian Gulf and United Arab Emirates in summer, *J. Geophys. Res.*, 113, D01204, doi:10.1029/2007JD008944.

Evan, A. T., J. Dunion, J. A. Foley, A. K. Heidinger, and C. S. Velden (2006), New evidence for a relationship between Atlantic tropical cyclone activity and African dust outbreaks, *Geophys. Res. Lett.*, 33, L19813, doi:10.1029/2006GL026408.

Evan, A. T., D. J. Vimont, A. K. Heidinger, J. P. Kossin, and R. Bennartz (2009), The role of aerosols in the evolution of tropical North Atlantic ocean temperature anomalies, *Science*, 324, 778–781, doi:10.1126/Science.1167404.

Fan, Y., and H. van den Dool (2004), Climate Prediction Center global monthly soil moisture data set at 0.5° resolution for 1948 to present, *J. Geophys. Res.*, 109, D10102, doi:10.1029/2003JD004345.

Fecan, F., B. Marticorena, and G. Bergametti (1999), Parameterization of the increase of the Aeolian erosion threshold wind friction velocity due to soil moisture for arid and semi-arid area, *Ann. Geophys.*, 17, 149 – 157.

Findlater, J. (1969), A major low-level air current near the Indian Ocean during the northern summer, *Quart. J. Roy. Meteor. Soc.*, 95, 362–380, doi:10.1002/qj.4970954.

Findlater, J. (1977), Observational aspect of the low-level cross equatorial jet stream of the western Indian Ocean, *Pure Appl. Geophys.*, 115, 1251–1262.

Fischer, J., F. Schott, and L. Stramma (1996), Currents and transports of the Great Whirl-Socotra Gyre system during the summer monsoon, August 1993, *J. Geophys. Res.*, 101(C2), 3573–3587, doi:10.1029/95JC03617.

Gabric, A. J., R. A. Cropp, G. H. McTainsh, B. M. Johnston, H. Butler, B. Tilbrook, and M. Keywood (2010), Australian dust storms in 2002–2003 and their impact on Southern Ocean biogeochemistry, *Global Biogeochem. Cycles*, 24, GB2005, doi:10.1029/2009GB003541.

- Garrison, D. L., et al. (2000), Microbial food web structure in the Arabian Sea: A U.S. JGOFS study, *Deep Sea Res., Part II*, 47, 1387–1422.
- Geider, R. J., and J. La Roche (1994), The role of iron in phytoplankton photosynthesis, and the potential for iron-limitation of primary productivity in the sea, *Photosynth. Res.*, 39(3), 275–301, doi:10.1007/BF00014588.
- Geyer, C. J. (2011), Introduction to Markov Chain Monte Carlo. *In Handbook of Markov chain Monte Carlo*. (eds S. Brooks, A. Gelman, G. K. Jones and Meng X. L.) FL: CRC Press. pp. 3–48.
- Ginoux, P., M. Chin, I. Tegen, J. Prospero, B. Holben, O. Dubovik, and S.-J. Lin (2001), Sources and distributions of dust aerosols simulated with the GOCART model, *J. Geophys. Res.*, 106, 20,255–20,273.
- Ginoux, P., D. Garbuzov, and H. C. Hsu (2010), Identification of anthropogenic and natural dust sources using Moderate Resolution Imaging Spectroradiometer (MODIS) Deep Blue level 2 data, *J. Geophys. Res.*, 115, D05204, doi:10.1029/2009JD012398.
- Ginoux, P., J. M. Prospero, T. E. Gill, N. C. Hsu, and M. Zhao (2012), Global-scale attribution of anthropogenic and natural dust sources and their emission rates based on MODIS Deep Blue aerosol products, *Rev. Geophys.*, 50, RG3005, doi:10.1029/2012RG000388.
- Goericke, R. (2002), Top-down control of phytoplankton biomass and community structure in the monsoonal Arabian Sea, *Limnol. Oceanogr.*, 47, 1307–1323.
- Goudie, A. S., and N. J. Middleton (2006), Desert Dust in the Global System, *Springer*, 287 pp.
- Grell, G. A., J. Dudhia, and D. R. Stauffer (1994), Description of the Fifth Generation Penn State/NCAR Mesoscale Model (MM5), *NCAR Tech. Note NCAR/TN-398 + STR*, 121 pp., NCAR, Boulder, Colo.
- Griffin, D. W., and C. A. Kellogg (2004), Dust storms and their impact on ocean and human health: Dust in Earth's atmosphere, *EcoHealth*, 1(3), 284–295, doi:10.1007/s10393-004-0120-8.

Herman, J. R., and E. A. Celarier (1997), Earth surface reflectivity climatology at 340–380 nm from TOMS data, *J. Geophys. Res.*, 102, 28 003–28 01.

Herman, J. R., P. B. Bhartia, O. Torres, C. Hsu, C. J. Seftor, and E. Celarier (1997), Global distribution of UV-absorbing aerosols from Nimbus 7/TOMS data. *J. Geophys. Res.*, 102, 16911–16921.

Hoell, A., C. Funk, M. Barlow (2014), La Niña diversity and Northwest Indian Ocean Rim teleconnections, *Clim Dyn.*, doi: 10.1007/s00382-014-2083-y.

Holben, B. N., et al. (1998), AERONET: A federated instrument network and data archive for aerosol characterization, *Remote Sens. Environ.*, 66, 1–16, doi:10.1016/S0034-4257(98)00031-5.

Honjo, S., J. Dymond, W. Prell, and V. Ittekkot (1999), Monsoon-controlled export fluxes to the interior of the Arabian Sea; U. S. JGOFS 1994–95 experiment, *Deep Sea Res., Part II*, 46, 1859–1902.

Hsu, N. C., S.-C. Tsay, M. D. King, and J. R. Herman (2004), Aerosol properties over bright-reflecting source regions, *IEEE Trans. Geosci. Remote Sens.*, 42(3), 557–569, doi:10.1109/TGRS.2004.824067.

Hsu, N. C., S.-C. Tsay, M. D. King, and J. R. Herman (2006), Deep Blue retrievals of Asian aerosol properties during ACE-Asia, *IEEE Trans. Geosci. Remote Sens.*, 44(11), 3180–3195, doi:10.1109/TGRS.2006.879540.

Hu, C., F. E. Muller-Karger, C. Taylor, K. L. Carder, C. Kelble, E. Johns, and C. A. Heil (2005), Red tide detection and tracing using MODIS fluorescence data: A regional example in SW Florida coastal waters, *Remote Sens. Environ.*, 97, 311–321, doi:10.1016/j.rse.2005.05.013.

Hubert, W. E., D. R. Morford, A. N. Hull, and R. E. Englebretson (1983), Forecasters handbook for the Middle East/Arabian sea, Rep. CR 83-06, *Nav. Environ. Predict. Res. Facil.*, Monterey, Calif.

Huneeus, N., et al. (2011) Global dust model intercomparison in AeroCom phase I, *Atmos. Chem. Phys.*, 11, 7781–7816, doi:10.5194/acp-11-7781-2011.

- Izumo, T., C. de Boyer Montegut, J.-J. Luo, S. K. Behera, S. Masson, and T. Yamagata (2008), The role of the western Arabian Sea upwelling in Indian monsoon rainfall variability, *J. Clim.*, 21, 5603–5623.
- Jiang, H., J. T. Farrar, R. C. Beardsley, R. Chen, and C. Chen (2009), Zonal surface wind jets across the Red Sea due to mountain gap forcing along both sides of the Red Sea, *Geophys. Res. Lett.*, 36, L19605, doi:10.1029/2009GL040008.
- Jickells, T. D., et al. (2005), Global iron connections between desert dust, ocean biogeochemistry, and climate, *Science*, 308, 67–71, doi:10.1126/science.1105959.
- Johnson, B. T., Brooks, M. E., Walters, D., Woodward, S., Christopher, S. and Schepanski, K. (2011), Assessment of the Met Office dust forecast model using observations from the GERBILS campaign, *Q.J.R. Meteorol. Soc.*, 137: 1131–1148. doi: 10.1002/qj.736.
- Johnson, M. S., N. Meskhidze, V. P. Kiliyanpilakkil, and S. Gassó (2011), Understanding the transport of Patagonian dust and its influence on marine biological activity in the South Atlantic Ocean, *Atmos. Chem. Phys.*, 11, 2487–2502, doi:10.5194/acp-11-2487-2011.
- Kalnay, E., et al. (1996), The NCEP/NCAR 40-year reanalysis project, *Bull. Am. Meteorol. Soc.*, 77, 437–471.
- Kaskaoutis, D.G., A. Rashki, E. E. Houssos, A. Mofidi, D. Goto, A. Bartzokas, P. Francois and M. Legrand (2014), Meteorological aspects associated with dust storms in the Sistan region, southeastern Iran, *Clim Dyn.*, doi: 10.1007/s00382-014-2208-3.
- Kaufman, Y. J., D. Tanré, L. A. Remer, E. F. Vermote, A. Chu, and B. N. Holben (1997), Operational remote sensing of tropospheric aerosol over land from EOS moderate resolution imaging spectroradiometer, *J. Geophys. Res.*, 102(D14), 17051–17067, doi:10.1029/96JD03988.
- Kaufman, Y., I. Koren, L. A. Remer, D. Tanre, P. Ginoux, and S. Fan (2005), Dust transport and deposition observed from the Terra-MODIS spacecraft over the Atlantic Ocean, *J. Geophys. Res.*, 110, D10S12, doi:10.1029/2003JD004436.

Kiehl, J., J. Hack, G. Bonan, B. Boville, B. Breigleb, D. Williamson and P. Rasch (1996), Description of the NCAR community climate model (ccm3), Technical report, National Center for Atmos. Res.

Kohfeld, K., and S. P. Harrison (2001), DIRTMAP: The geologic record of dust, *Earth Sci. Rev.*, 54, 81–114.

Krishnamurti, T. N., B. Jha, J. Prospero, A. Jayaraman, and V. Ramanathan (1998), Aerosol and pollutant transport and their impact on radiative forcing over the tropical Indian Ocean during the January–February 1996 pre-INDOEX cruise, *Tellus Ser. B*, 50, 521–542.

Kubilay, N., S. Nickovic, C. Moulin, and F. Dulac (2000), An illustration of the transport and deposition of mineral dust onto the eastern Mediterranean. *Atmos. Environ.*, 34, 1293–1303.

Kumar, A., and M. P. Hoerling (2003), The nature and causes for the delayed atmospheric response to El Nino. *J. Climate*, 16, 1391–1403.

Kumar, K. K., B. Rajagopatan, M. Hoerling, G. Bates, and M. Cane (2006), Unraveling the mystery of Indian monsoon failure during El Niño, *Science*, 314(5796), 115–119, doi:10.1126/science.1131152.

Kumar, S. P., and T. G. Prasad (1999), Formation and spreading of Arabian Sea high-salinity water mass, *J. Geophys. Res.*, 104(C1), 1455–1464, doi:10.1029/1998JC900022.

Lal, D.M., S. D. Patil, H. N. Singh, Sachin D. Ghude, S. Tiwari and Manoj K. Srivastava (2013), Influence of aerosol on clouds over the Indo-Gangetic Plain, India, *Clim Dyn*, 41, 601–612, doi: 10.1007/s00382-013-1775-z.

Landry, J. R., S. L. Brown, L. Campbell, J. Constantinou, and H. Liu (1998), Spatial patterns in phytoplankton growth and microzooplankton grazing in the Arabian Sea during monsoon forcing, *Deep Sea Res., Part II*, 45, 2353–2368.

Lau, K.-M., and K.-M. Kim (2006), Observational relationships between aerosol and Asian monsoon rainfall, and circulation, *Geophys. Res. Lett.*, 33, L21810, doi:10.1029/2006GL027546.

- Laurent, B., I. Tegen, B. Heinold, K. Schepanski, B. Weinzierl, and M. Esselborn (2010), A model study of Saharan dust emissions and distributions during the SAMUM-1 campaign, *J. Geophys. Res.*, 115, D21210, doi:10.1029/2009JD012995.
- Lelieveld, J., et al. (2001), The Indian Ocean Experiment: Widespread air pollution from south and southeast Asia, *Science*, 291, 1031–1036, doi:10.1126/science.1057103.
- Léon, J., and M. Legrand (2003), Mineral dust sources in the surroundings of the north Indian Ocean, *Geophys. Res. Lett.*, 30(6), 1309, doi:10.1029/2002GL016690.
- Levy, R. C., L. A. Remer, D. Tanré, S. Mattoo, and Y. J. Kaufman (2009), Algorithm for remote sensing of tropospheric aerosol over dark targets from MODIS: Collections 005 and 051: Revision 2, MOD04/MYD04, NASA Goddard Space Flight Cent., Greenbelt, Md.
- Li, F., and V. Ramanathan (2002), Winter to summer monsoon variation of aerosol optical depth over the tropical Indian Ocean, *J. Geophys. Res.*, 107(D16), 4284, doi:10.1029/2001JD000949.
- Li, F., P. Ginoux, and V. Ramaswamy (2010), Transport of Patagonian dust to Antarctica, *J. Geophys. Res.*, 115, D18217, doi:10.1029/2009JD012356.
- Liebmann, B., and C. A. Smith (1996), Description of a complete (interpolated) outgoing longwave radiation dataset, *Bull. Amer. Meteor. Soc.*, **77**, 1275–1277.
- Lin, I.-I., et al. (2011), Fertilization potential of volcanic dust in the low-nutrient low-chlorophyll western North Pacific subtropical gyre: Satellite evidence and laboratory study, *Global Biogeochem. Cycles*, 25, GB1006, doi:10.1029/2009GB003758.
- Littmann, T. (1991), Dust storm frequency in Asia—Climatic control and variability, *Int. J. Climatol.*, 11(4), 393–412.
- Locarnini, R. A., A. V. Mishonov, J. I. Antonov, T. P. Boyer, H. E. Garcia, O. K. Baranova, M. M. Zweng, and D. R. Johnson (2010), *World Ocean Atlas 2009*, vol. 1, Temperature, edited by S. Levitus, 184 pp., U.S. Govt. Print. Off., Washington, D. C.
- Lohmann, U., and J. Feichter (2005), Global indirect aerosol effects: A review, *Atmos. Chem. Phys.*, 5, 715–737, doi:10.5194/acp-5-715-2005.

Luo, C., N. Mahowald, and C. Jones (2004), Temporal variability of dust mobilization and concentration in source regions, *J. Geophys. Res.*, 109, D20202, doi:10.1029/2004JD004861.

Mackie, D. S., J. M. Peat, G. H. McTainsh, P. W. Boyd, and K. A. Hunter (2006), Soil abrasion and eolian dust production: Implications for iron partitioning and solubility, *Geochem. Geophys. Geosyst.*, 7, Q12Q03, doi:10.1029/2006GC001404.

Madhupratap, M., S. P. Kumar, P. M. A. Bhattathiri, M. D. Kumar, S. Raghukumar, K. K. C. Nair, and N. Ramaiah (1996), Mechanism of the biological response to winter cooling in the northeastern Arabian Sea, *Nature*, 384, 549–552.

Maher, B. A., J. M. Prospero, D. Mackie, D. Gaiero, P. P. Hesse, and Y. Balkanski (2010), Global connections between aeolian dust, climate and ocean biogeochemistry at the present day and at the last glacial maximum, *Earth Sci. Rev.*, 99, 61–97, doi:10.1016/j.earscirev.2009.12.001.

Mahowald, N. M., and C. Luo (2003), A less dusty future?, *Geophys. Res. Lett.*, 30(17), 1903, doi:10.1029/2003GL017880.

Mahowald, N., A. Baker, G. Bergametti, N. Brooks, R. Duce, T. Jickells, N. Kubilay, J. Prospero, and I. Tegen (2005), The atmospheric global dust cycle and iron inputs to the ocean, *Global Biogeochem. Cycles*, 19, GB4025, doi:10.1029/2004GB002402.

Mahowald, N. M., et al. (2010), Observed 20th century desert dust variability: Impact on climate and biogeochemistry, *Atmos. Chem. Phys.*, 10, 10,875–10,893, doi:10.5194/acp-10-10875-2010.

Mariotti, A., J. Ballabrera-Poy, and N. Zeng (2005), Tropical influence on Euro-Asian autumn rainfall variability, *Climate Dyn.*, 24, 511–521.

Mariotti, A. (2007), How ENSO impacts precipitation in southwest central Asia, *Geophys. Res. Lett.*, 34, L16706, doi:10.1029/2007GL030078.

Martin, J. H., and S. Fitzwater (1988), Iron deficiency limits phytoplankton growth in the northeast pacific subarctic, *Nature*, 331, 341–343, doi:10.1038/331341a0.

Martin, J. (1990), Glacial-interglacial CO<sub>2</sub> change: The iron hypothesis, *Paleoceanography*, 5, 1-13.

- Martin, J., S. Fitzwater, R. Gordon, C. Hunter, and S. Tanner (1993), Iron, primary production and carbon-nitrogen flux studies during the JGOFS North Atlantic Bloom Experiment, *Deep Sea Res., Part II*, 40, 115–134.
- Martinez-Garcia, A., A. Rosell-Mele, S. L. Jaccard, W. Geibert, D. M. Sigman, and G. H. Haug (2011), Southern Ocean dust–climate coupling over the past four million years, *Nature*, 476, 312–315, doi:10.1038/nature10310.
- Martyn, D. (1992), *Climates of the World*, Elsevier, 436 pp.
- McCreary, J., and P. Kundu (1988), A numerical investigation of the Somali Current during the Southwest Monsoon, *J. Mar. Res.*, 46(1), 25–58, doi:10.1357/002224088785113711.
- Measures, C.I., and S. Vink (1999), Seasonal variations in the distribution of Fe and Al in the surface waters of the Arabian Sea, *Deep Sea Res., Part II*, 46, 1597–1622.
- Membery, D. A. (1983), Low level wind profiles during the Gulf shamal, *Weather*, 38, 18–24.
- Membery, D. (1985), A gravity-wave haboob?, *Weather*, 40(7), 214–221.
- Menon, S., J. Hansen, and L. Nazarenko (2002), Climate effects of black carbon aerosols in China and India, *Science*, 297, 2250–2253.
- Meyers, G., P. McIntosh, L. Pigot, and M. Pook (2007), The years of El Niño, La Niña and interactions with the tropical Indian Ocean. *J. Clim.*, 20, 2872–2880, doi:10.1175/JCLI4152.1.
- Middleton, N. J. (1986), A geography of dust storms in South-West Asia, *J. Climatol.*, 6, 183–196. doi: 10.1002/joc.3370060207.
- Miller, R. L., I. Tegen, and J. Perlwitz (2004), Surface radiative forcing by soil dust aerosols and the hydrologic cycle, *J. Geophys. Res.*, 109, D04203, doi:10.1029/2003JD00408.
- Miller, S. D., A. P. Kuciauskas, M. Liu, Q. Ji, J. S. Reid, D. W. Breed, A. L. Walker, and A. A. Mandoos (2008), Haboob dust storms of the southern Arabian Peninsula, *J. Geophys. Res.*, 113, D01202, doi:10.1029/2007JD008550.

- Moore, J. K., S. C. Doney, D. M. Glover, and I. Y. Fung (2002), Iron cycling and nutrient-limitation patterns in surface waters of the world ocean, *Deep Sea Res., Part II*, 49, 463–507.
- Morrison, J. M., L. A. Codispoti, S. Gaurin, B. Jones, V. Manghnani, and Z. Zheng (1998), Seasonal variation of hydrographic and nutrient fields during the US JGOFS Arabian Sea Process Study, *Deep Sea Res., Part II*, 45, 2053–2101.
- Moulin, C., C. E. Lambert, F. Dulac, and U. Dayan (1997), Control of atmospheric export of dust from North Africa by the North Atlantic Oscillation, *Nature*, 387, 691–694.
- Müller, D., K. Franke, F. Wagner, D. Althausen, A. Ansmann, J. Heintzenberg, and G. Verver (2001), Vertical profiling of optical and physical particle properties over the tropical Indian Ocean with six-wavelength lidar: 2. Case studies, *J. Geophys. Res.*, 106, 28577–28595, doi:10.1029/2000JD900785.
- Nair, S. K., K. Parameswaran, and K. Rajeev (2005), Seven-years satellite observations of the mean structure and variabilities in the regional aerosol distribution over the oceanic areas around the Indian subcontinent, *Ann. Geophys.*, 23, 2011–2030.
- Naqvi, S. W. A., et al. (2000), Increased marine production of N<sub>2</sub>O due to intensifying anoxia on the Indian continental shelf, *Nature*, 408, 346–349.
- Naqvi, S. W. A., H. Naik, A. Pratihary, W. D'Souza, P. V. Narvekar, D. A. Jayakumar, A. H. Devol, T. Yoshinari, and T. Saino (2006), Coastal versus open-ocean denitrification in the Arabian Sea, *Biogeosciences*, 3, 621–633, doi:10.5194/bg-3-621-2006.
- Naqvi, S.W.A., et al. (2010), The Arabian Sea as a high-nutrient low-chlorophyll region during the late Southwest Monsoon, *Biogeosciences*, 7, 2091–2100, doi: 10.5194/bg-7-2091-2010.
- Nazemosadat, M. J., and A. R. Ghasemi (2004), Quantifying the ENSO related shifts in the intensity and probability of drought and wet periods in Iran, *J. Clim.*, 17, 4005–4018.
- Nishioka, J., H. Obata, and D. Tsumune (2013), Evidence of an extensive spread of hydrothermal dissolved iron in the Indian Ocean, *Earth Planet. Sc. Lett.*, 361, 26–33.

- Nodwell, L. M., and N. M. Price (2001), Direct use of inorganic colloidal iron by marine mixotrophic phytoplankton, *Limnol. Oceanogr.*, 46(4), 765–777.
- Notaro, M., F. Alkolibi, E. Fadda, and F. Bakhrjy (2013), Trajectory analysis of Saudi Arabian dust storms. *J. Geophys. Res. Atmos.*, 118, 6028–6043, doi:10.1002/jgrd.50346.
- O'Reilly, J. E., S. Maritorena, D. Siegel, and M.C. O'Brien (2000), Ocean color chlorophyll a algorithms for SeaWiFS, OC2, and OC4: version 4, in: SeaWiFS postlaunch technical report series, volume 11, SeaWiFS postlaunch calibration and validation analyses, part 3, edited by: Hooker, S. B. and Firestone, E. R., Greenbelt, Maryland: NASA Goddard Space Flight Center, 9–23.
- Pal, J. S., E. E. Small, A. B. Eltahir (2000), Simulation of regional scale water and energy budgets: Representation of subgrid cloud and precipitation processes within RegCM, *J. Geophys. Res.*, 105, 29,579–29,594.
- Patra, P. K., M. D. Kumar, N. Mahowald, and V. V. S. S. Sarma (2007), Atmospheric deposition and surface stratification as controls of contrasting chlorophyll abundance in the North Indian Ocean, *J. Geophys. Res.*, 112, C05029, doi:10.1029/2006JC003885.
- Pease, P. P., V. P. Tchakerian, and N. W. Tindale (1998), Aerosols over the Arabian Sea: Geochemistry and source areas for aeolian desert dust, *J. Arid Environ.*, 39, 477– 496.
- Pedgley, D. E. (1974), An outline of the weather and climate of the Red Sea, in *L'Océanographie Physique de la Mer Rouge*, pp. 9–27, U. N. Ed. Sci. and Cult. Org., Paris.
- Perrone, T. J. (1979), Winter Shamal in the Persian Gulf, Tech. Rep. TR 79-06, 168 pp., Nav. Environ. Predict. Res. Facil., Monterey, Calif.
- Perry, K. D., T. A. Cahill, R. A. Eldred, D. D. Dutcher, and T. E. Gill (1997), Long-range transport of North African dust to the eastern United States, *J. Geophys. Res.*, 102(D10), 11225–11238, doi:10.1029/97JD00260.
- Pöschl, U. (2005), Atmospheric aerosols: Composition, transformation, climate and health effects, *Angew. Chem. Int. Ed.*, 44, 7520–7540.

Prasad, T. G., M. Ikeda, and S. P. Kumar (2001), Seasonal spreading of the Persian Gulf Water mass in the Arabian Sea, *J. Geophys. Res.*, 106(C8), 17059–17071, doi:10.1029/2000JC000480.

Prasanna Kumar, S., and T. G. Prasad (1999), Formation and spreading of Arabian Sea high salinity water mass, *J. Geophys. Res.*, 104, 1455–1464.

Prasanna Kumar, S., M. Madhupratap, M. Dileep Kumar, P. M. Muraleedharan, S. N. de Souza, M. Gauns, and V. V. S. S. Sarma (2001), High biological productivity in the central Arabian Sea during summer monsoon driven by Ekman pumping and lateral advection, *Curr. Sci.*, 81, 1633–1638.

Prasanna Kumar, S., N. Ramaiah, M. Gauns, V. V. S. S. Sarma, P. M. Muraleedharan, S. Raghukumar, M. D. Kumar, and M. Madhupratap (2001), Physical forcing of biological productivity in the northern Arabian Sea during the Northeast Monsoon, *Deep Sea Res., Part II*, 48(6–7), 1115–1126, doi:10.1016/S0967-0645(00)00133-8.

Prasanna Kumar, S., R. P. Roshin, J. Narvekar, P. K. Dinesh Kumar, and E. Vivekanandan (2010), What drives the increased phytoplankton biomass in the Arabian Sea?, *Curr. Sci.*, 99, 101–106.

Price, J. F., R. A. Weller, and R. Pinkel (1986), Diurnal cycling: Observations and models of the upper ocean response to diurnal heating, cooling, and wind mixing, *J. Geophys. Res.*, 91(C7), 8411–8427, doi:10.1029/JC091iC07p08411.

Prospero, J. M., and P. J. Lamb (2003), African droughts and dust transport to the Caribbean: Climate change implications, *Science*, 302, 1024–1027.

Prospero, J. M., P. Ginoux, O. Torres, S. E. Nicholson, and T. E. Gill (2002), Environmental characterization of global sources of atmospheric soil dust identified with the NIMBUS 7 Total Ozone Mapping Spectrometer (TOMS) absorbing aerosol product, *Rev. Geophys.*, 40(1), 1002, doi:10.1029/2000RG000095.

Rahul, P. R. C., P. S. Salvekar, and P. C. S. Devara (2008), Aerosol optical depth variability over Arabian Sea during drought and normal years of Indian monsoon, *Geophys. Res. Lett.*, 35, L22812, doi:10.1029/2008GL035573.

- Randel, W. J., M. Park, L. Emmons, D. Kinnison, P. Bernath, K. A. Walker, C. Boone, and H. Pumphrey (2010), Asian monsoon transport of pollution to the stratosphere, *Science*, 328, 611–613, doi:10.1126/science.1182274.
- Rao, P.G., H.R. Hatwar, H.H. Al-Sulaiti, A.H. Al-Mulia (2003), Summer Shamals over the Arabian Gulf, *Weather*, 58, 472–478.
- Rashki, A., Kaskaoutis, D.G., Goudie, A.S., Kahn, R.A. (2013), Dryness of ephemeral lakes and consequences for dust activity: the case of the Hamoun drainage basin, southeastern Iran, *Sci Total Environ.*, 463–464:552–564.
- Raupach, M. R., G. H. McTainsh, and J. F. Leys (1994), Estimates of dust mass in some recent major Australian dust storms, *Aust. J. Soil Water Conserv.*, 7(3), 20–24.
- Redfield, A. C., B. H. Ketchum, and F. A. Richards (1963), The influence of organisms on the composition of seawater, in *The Sea*, vol. II, edited by M. N. Hill, pp. 26–77, Interscience, New York.
- Remer, L. A., et al. (2002), Validation of MODIS aerosol retrieval over ocean, *Geophys. Res. Lett.*, 29(12), 8008, doi:10.1029/2001GL013204.
- Rodwell, M. J., and B. J. Hoskins (1996), Monsoons and the dynamics of deserts, *Q. J. R. Meteorol. Soc.*, 122, 1385–1404, doi:10.1002/qj.49712253408.
- Ropelewski C.F., and M. S. Halpert (1987), Global and regional scale precipitation patterns associated with the El Nino/Southern Oscillation, *Monthly Weather Review*, 115, 1606–1626.
- Rosenfeld, D., Y. Rudich, and R. Lahav (2001), Desert dust suppressing precipitation: A possible desertification feedback loop, *Proc. Natl. Acad. Sci.*, 98, 5975–5980.
- Ryther, J. H., J. R. Hall, A. K. Pease, A. Bakun, and M. M. Jones (1966), Primary production in relation to the chemistry and hydrography of the western Indian Ocean, *Limnol. Oceanogr.*, 11, 371–380, doi:10.4319/lo.1966.11.3.0371.
- Saji, N. H., B. N. Goswami, P. N. Vinayachandran, and T. Yamagata (1999), A dipole mode in the tropical Indian Ocean, *Nature*, 401, 360–363, doi:10.1038/43854.

Satheesh, S. K., J. Srinivasan, and K. K. Moorthy (2006), Contribution of sea-salt to aerosol optical depth over the Arabian Sea derived from MODIS observations, *Geophys. Res. Lett.*, 33, L03809, doi:10.1029/2005GL024856.

Savoie, D. L., J. M. Prospero, and R. T. Nees (1987), Nitrate, non-sea-salt sulfate, and mineral aerosol over the northwestern Indian Ocean, *J. Geophys. Res.*, 92(D1), 933–942, doi:10.1029/JD092iD01p00933.

Schepanski, K., I. Tegen, and A. Macke (2009), Saharan dust transport and deposition towards the tropical northern Atlantic, *Atmos. Chem. Phys.*, 9, 1173–1189, doi:10.5194/acp-9-1173-2009.

Schepanski, K., I. Tegen, and A. Macke (2012), Comparison of satellite based observations of Saharan dust source areas, *Remote Sens. Environ.*, 123, 90–97, doi:10.1016/j.rse.2012.03.019

Schneider, U., A. Becker, P. Finger, A. Meyer-Christoffer, M. Ziese, and B. Rudolf (2013), GPCC's new land surface precipitation climatology based on quality-controlled in situ data and its role in quantifying the global water cycle, *Theor. Appl. Climatol.*, 1–26.

Schott, F., and J. P. McCreary (2001), The monsoon circulation of the Indian Ocean, *Prog. Oceanogr.*, 51, 1–123.

Schott, F. A., S.-P. Xie, and J. P. McCreary Jr. (2009), Indian Ocean circulation and climate variability, *Rev. Geophys.*, 47, RG1002, doi:10.1029/2007RG000245.

Shahsavani, A. et al. (2012), Characterization of Ionic Composition of TSP and PM10 during the Middle Eastern Dust (MED) Storms in Ahvaz, Iran, *Environ. Monit. Assess*, 184 ( 11), 6683–6692.

Shetye, S. R., A. D. Gouveia, S. S. C. Shenoi, D. Sundar, G. S. Michael, A. M. Almeida, and K. Santanam (1990), Hydrography and circulation off the west coast of India during the southwest monsoon 1987, *J. Mar. Res.*, 48, 359–378, doi:10.1357/002224090784988809.

Shetye, S. R., A. D. Gouveia, S. S. C. Shenoi, G. S. Michael, D. Sundar, A. M. Almeida, and K. Santanam (1991), The coastal current off western India during the northeast monsoon, *Deep Sea Res., Part I*, 38, 1517–1529.

- Shetye, S. R., A. D. Gouveia, S. S. C. Shenoi (1994), Circulation and water masses of the Arabian Sea, Biogeochemistry of the Arabian Sea D. Lal, 9–25, *Ind. Acad. of Sci.*, Bangalore.
- Shetye, S. R., I. Suresh, D. Shankar, D. Sundar, S. Jayakumar, P. Mehra, R. G. Prabhudesai, and P. S. Pednekar (2008), Observational evidence for remote forcing of the West India Coastal Current, *J. Geophys. Res.*, 113, C11001, doi:10.1029/2008JC004874.
- Siefert, R. L., A. M. Johansen, and M. R. Hoffmann (1999), Chemical characterization of ambient aerosol collected during the southwest monsoon and intermonsoon seasons over the Arabian Sea: Labile-Fe(II) and other trace metals, *J. Geophys. Res.*, 104(D3), 3511–3526, doi:10.1029/1998JD100067.
- Singh, R. P., A. K. Prasad, V. K. Kayetha, and M. Kafatos (2008), Enhancement of oceanic parameters associated with dust storms using satellite data, *J. Geophys. Res.*, 113, C11008, doi:10.1029/2008JC004815.
- Singh, A., N. Gandhi, and R. Ramesh (2012), Contribution of atmospheric nitrogen deposition to new production in the nitrogen limited photic zone of the northern Indian Ocean, *J. Geophys. Res.*, 117, C06004, doi:10.1029/2011JC007737
- Smirnov, A., B. N. Holben, T. F. Eck, O. Dubovik, and I. Slutsker (2003), Effect of wind speed on columnar aerosol optical properties at Midway Island, *J. Geophys. Res.*, 108(D24), 4802, doi:10.1029/2003JD003879.
- Smith, S. L. (2001), Understanding the Arabian Sea: Reflections on the 1994–1996 Arabian Sea expedition, *Deep Sea Res., Part II*, 48, 1385–1402.
- Smith, S.L. and Madhupratap, M. (2005), Mesozooplankton of the Arabian Sea: patterns influenced by seasons, upwelling, and oxygen concentrations, *Prog. Oceanogr*, 65, 214–239.
- Solmon, F., F. Giorgi, and C. Liousse (2006), Aerosol modelling for regional climate studies: Application to anthropogenic particles and evaluation over a European/African domain, *Tellus B*, 58(1), 51–72, doi:10.1111/j.1600-0889.2005.00155.X.

Srinivas, B., Sarin, M. and Kumar, A., (2011), Impact of anthropogenic sources on aerosol iron solubility over the Bay of Bengal and the Arabian Sea, *Biogeochem*, 110 (1-3), 257-268, doi:10.1007/s10533-011-96801-1.

Stocker, T. F., and Coauthors, Eds., (2014), *Climate Change 2013: The Physical Science Basis*. Cambridge University Press, 1535 pp.

Sunda, W., and S. Huntsman (1995), Iron uptake and growth limitation in oceanic and coastal phytoplankton, *Mar. Chem.*, 50, 189–206.

Sunda, W. G. (1997), Control of dissolved iron concentrations in the world ocean: A comment, *Mar. Chem.*, 57, 169–172.

Syed, F., F. Giorgi, J. Pal, and M. King (2006), Effect of remote forcings on the winter precipitation of central southwest Asia. Part 1: Observations, *Theor. Appl. Climatol.*, 86, 147–160.

Takeda, S., A. Kamatani, and K. Kawanobe (1995), Effects of nitrogen and iron enrichments on phytoplankton communities in the northwestern Indian Ocean, *Mar. Chem.*, 50, 229–241.

Tanré, D., Y. J. Kaufman, M. Herman, and S. Mattoo (1997), Remote sensing of aerosol properties over oceans using the MODIS/EOS spectral radiances, *J. Geophys. Res.*, 102(D14), 16971–16988, doi:10.1029/96JD03437.

Taylor S.R. and McLennan S.H. (1985), *The continental crust: its composition and evolution*, Blackwell (Oxford).

Tegen, I., M. Werner, S. P. Harrison, and K. E. Kohfeld (2004), Relative importance of climate and land use in determining present and future global soil dust emission, *Geophys. Res. Lett.*, 31, L05105, doi:10.1029/2003GL019216.

Tindale, N. W., and P. P. Pease (1999), Aerosols over the Arabian Sea: Atmospheric transport pathways and concentrations of dust and sea salt, *Deep Sea Res., Part II*, 46, 1577–1595.

Tomczak, M., and J. S. Godfrey (1994), *Regional Oceanography: An Introduction*, 193 pp., Elsevier, New York.

Torrence, C., and P. J. Webster (1999), Interdecadal changes in the ENSO-monsoon system, *J. Climate*, 12, 2679–2690.

Trenberth, K. E. (1997), The definition of El Niño. *Bull. Am. Meteorol. Soc.*, 78, 2771–2777.

Tripathi, J. K., and V. Rajamani (1999), Geochemistry of the loessic sediments on Delhi ridge, eastern Thar Desert, Rajasthan: Implications for exogenic processes, *Chem. Geol.*, 155, 265–278.

Uno, I., K. Eguchi, K. Yumimoto, T. Takemura, A. Shimizu, M. Uematsu, Z. Liu, Z. Wang, Y. Hara, and N. Sugimoto (2009), Asian dust transported one full circuit around the globe, *Nat. Geosci.*, 2, 557–560.

Vecchi, G. A., S.-P. Xie, and A. S. Fischer (2004), Ocean-atmosphere co-variability in the western Arabian Sea, *J. Clim.*, 17, 1213–1224.

Vernier, J.-P., L. W. Thomason, and J. Kar (2011), CALIPSO detection of an Asian tropopause aerosol layer, *Geophys. Res. Lett.*, 38, L07804, doi:10.1029/2010GL046614.

Vinoj, V., P. J. Rasch, H. Wang, J.-H. Yoon, P.-L. Ma, K. Landu, and B. Singh (2014), Short-term modulation of Indian summer monsoon rainfall by West Asian dust, *Nat. Geosci.*, 7, 308–313, doi:10.1038/ngeo2107.

Vishkaee, A. F., C. Flamant, J. Cuesta, L. Oolman, P. Flamant, and H. R. Khalesifard (2012), Dust transport over Iraq and northwest Iran associated with winter Shamal: A case study, *J. Geophys. Res.*, 117, D03201, doi:10.1029/2011JD016339.

Vu, H.T.D., and Y. Sohrin (2013), Diverse stoichiometry of dissolved trace metals in the Indian Ocean, *Sci. Rep.* 3, p. 1745, doi:10.1038/srep01745.

Wiggert, J.D., and R.G. Murtugudde (2007), The sensitivity of the southwest monsoon phytoplankton bloom to variations in aeolian iron deposition over the Arabian Sea, *J. Geophys. Res.*, Vol. 112, C05005, doi: 10.1029/2006JC003514.

Wiggert, J. D., R. R. Hood, S. W. A. Naqvi, K. H. Brink, and S. L. Smith (2009), Indian Ocean Biogeochemical Processes and Ecological Variability, *Geophys. Monogr. Ser.*, Vol. 185, American Geophysical Union, 429pp.

Xie, S.-P., H. Annamalai, F. Schott, and J. P. McCreary Jr. (2002), Origin and predictability of South Indian Ocean climate variability, *J. Clim.*, 15(8), 864–874.

Yamagata, T., S. K. Behera, J.-J. Luo, S. Masson, M. R. Jury, and S. A. Rao (2004), The coupled ocean-atmosphere variability in the tropical Indian Ocean, in *Earth's Climate: The Ocean-Atmosphere Interaction*, *Geophys. Monogr. Ser.*, vol. 147, edited by C. Wang et al., pp. 189–211, AGU, Washington, D. C.

Yang, J., Q. Liu, S.-P. Xie, Z. Liu, and L. Wu (2007), Impact of the Indian Ocean SST basin mode on the Asian summer monsoon, *Geophys. Res. Lett.*, 34, L02708, doi:10.1029/2006GL028571.

Yu, L., and R. A. Weller (2007), Objectively analyzed air-sea heat fluxes for the global ice-free oceans (1981–2005), *Bull. Am. Meteorol. Soc.*, 88, 527–539.

Yu, Y., M. Notaro, Z. Liu, O. Kalashnikova, F. Alkolibi, E. Fadda, and F. Bakhrjy (2013), Assessing temporal and spatial variations in atmospheric dust over Saudi Arabia through satellite, radiometric, and station data, *J. Geophys. Res. Atmos.*, 118, 13253–13264, doi:10.1002/2013JD020677.

Zakey, A. S., F. Solmon, and F. Giorgi (2006), Development and testing of a desert dust module in a regional climate model, *Atmos. Chem. Phys.*, 6, 1749–1792.

Zender, C. S., H. Bian, and D. Newman (2003), Mineral Dust Entrainment and Deposition (DEAD) model: Description and 1990s dust climatology, *J. Geophys. Res.*, 108, 4416, doi:10.1029/2002JD002775, D14.

Zender, C. S., D. Newman, and O. Torres (2003), Spatial heterogeneity in aeolian erodibility: Uniform, topographic, geomorphic, and hydrologic hypotheses, *J. Geophys. Res.*, 108(D17), 4543, doi:10.1029/2002JD003039.

Zender, C. S., R. Miller, and I. Tegen (2004), Quantifying mineral dust mass budgets: Terminology, constraints, and current estimates, *Eos Trans. AGU*, 85(48), 509–512.

Zhang, L., S.-L. Gong, J. Padro, and L. Barrie (2001), A size-segregated particle dry deposition scheme for an atmospheric aerosol module, *Atmos. Environ.*, 35(3), 549–560.

Zhu, A., V. Ramanathan, F. Li, and D. Kim (2007), Dust plumes over the Pacific, Indian, and Atlantic oceans: Climatology and radiative impact, *J. Geophys. Res.*, *112*, D16208, doi:10.1029/2007JD008427.

Zhuang, G., Z. Yi, R. A. Duce, and P. R. Brown (1992), Chemistry of iron in marine aerosols, *Global Biogeochem. Cycles*, *6*(2), 161–173, doi:10.1029/92GB00756.

Zobler, L. A. (1986), World Soil File for Global Climate Modeling, NASA.